Title

A smart manufacturing inspired approach to research in electrochemisty applied to electrochemical carbon dioxide reduction and steam methane reforming

Author

Richard, Derek Michael

Publication Date

2023

UNIVERSITY OF CALIFORNIA

Los Angeles

A smart manufacturing inspired approach to research in electrochemisty applied to electrochemical carbon dioxide reduction and steam methane reforming

A dissertation submitted in partial satisfaction of the
requirement for the degree Doctor of Philosophy
in Chemical Engineering

by

Derek Michael Richard

2023

ABSTRACT OF THE DISSERTATION

A smart manufacturing inspired approach to research in electrochemisty
applied to electrochemical carbon dioxide reduction and steam methane reforming

by

Derek Michael Richard
Doctor of Philosophy in Chemical Engineering
University of California, Los Angeles, 2023
Professor Carlos G. Morales Guio, Chair

Electrochemical technologies have the potential to dramatically reshape the global energy landscape, but implementation at commercial scales has been slow. Technologies like fuel cells and electrolyzers are recently gaining more widespread traction and are being demonstrated at large scale. These developments are being fueled by the push to convert to energy carriers that can be produced without greenhouse gas emissions. However, technologies like electrochemical CO_2 reduction, that involve more complicated chemistry and multi-step reaction mechanisms, are still far from industrial applications despite having been under development for decades. Progress in these more complicated systems is slow due to the multitude of variables that affect the reaction. Complex interactions between mass, charge, and heat transport, along with reaction kinetics are often convoluted and difficult to distinguish using traditional research methods. These methods rely on relatively small data sets and often use poorly characterized experimental systems that provide inconsistent results. For example, in electrochemical CO_2 reduction research, mass transport effects have generally been overlooked in the study of different catalysts over the past decade. However, recent work has shown that what is measured in these electrochemical cells is not the in-

trinsic *reaction kinetics*, but rather the *reactor kinetics* that are dependent on the reactor geometry and its influence on the many factors involved in the reaction of interest. Designing experimental systems that can isolate specific phenomena will be extremely difficult, if not impossible. Thus, new methods must be developed to aid in the extraction of fundamental relationships governing the processes occurring in these experimental systems.

This thesis explores how experimental electrochemistry can utilize methods inspired by Smart Manufacturing (SM) to accelerate the extraction of underlying relationships in complex electrochemical systems. In contrast to traditional experimental methods, SM techniques rely on large data sets to extract useful information from complex processes and optimize control. With large data sets of high quality data, modern computing capabilities can take advantage of computational methods in machine learning and multi-scale modeling to quickly draw hidden foundational relationships out of complex systems. Additionally, by utilizing sensing, data handling, and modeling techniques similar to those that will be used when an experimental technology is commercialized, this SM inspired approach can help to ensure that appropriate techniques are used when the technology is scaled up.

First, the framework for the application of SM techniques to electrochemical research will be discussed, and brief demonstrations of its utility will be presented. The following chapters will provide more detailed discussion of computational fluid dynamics modeling efforts in the application of this framework to electrochemical CO_2 reduction research and characterization of our experimental system. Finally, a second case where the framework has been applied to the development of an experimental system for testing electrochemical steam methane reforming will be discussed along with motivation for the development of this system. Together, these cases demonstrate how SM techniques can be applied in the lab to accelerate discoveries and provide an understanding of how they might be applied in other areas of research.

The dissertation of Derek Michael Richard is approved.

Panagiotis D. Christofides

Eric M. V. Hoek

Philippe Sautet

Carlos G. Morales Guio, Committee Chair

University of California, Los Angeles

2023

Contents

List of Figures

List of Tables

ACKNOWLEDGMENTS

First I would like to thank my advisor, Professor Carlos G. Morales Guio for his guidance and support. I believe his efforts to challenge common assumptions in electrochemistry has help me to form a more critical approach to research and development of electrochemical systems and the collaborations he has forged with other labs in the department have provided me with opportunities to develop broader engineering skills alongside electrochemistry. I would also like to thank Professor Panagiotis D. Christofides for his guidance and support in my work with computation fluid dynamics simulations and smart manufacturing. His extensive experience has been a very helpful resource for my research.

I thank Dr. Rod Borup of Los Alamos National Lab for his guidance during my time as a post bachelor intern in Los Alamos and his advice during my time as a graduate student at UCLA. His example and the experience that he provided me was instrumental in my decision to pursue a doctorate at UCLA. I also thank Professor Lauren Greenlee who provided me with the initial research experience as an undergraduate student at the University of Arkansas and who first showed me why electrochemistry is so exciting.

I am also grateful for the friendship and collaborations with my fellow graduate students in the Morales-Guio group and Christofides group and throughout the Chemical and Biomolecular Engineering Department at UCLA. In particular I would like to thank Matthew Tom for all of his help with the Ansys Fluent simulations and willingness to help with anything and everything around the lab. I'm also especially grateful for Joonbaek Jang, Berkay Çitmaci, Vito Canuso, Junwei Luo, and Sungil Yun for their help in conducting research and their friendship.

I would also like to thank Professor Philippe Sautet and Professor Eric Hoek for serving on my doctoral committee. Additionally, I would like thank all of the Chemical and Biomolecular Engineering department faculty for sharing their unique perpectives and talent, along with out collaborators on the DOE CESMII project, especially Jim Davis, and Haresh malkani..

Last but not least, I would like to thank my family and friends for their support throughout

my graduate research, especially during the COVID pandemic in my early years at UCLA. The company of our neighbors, especially Shan and Christine Bird as well as good friends Alex and Sara Woodard brightened my time at UCLA. I am also especially grateful for the friendship I've developed with Taylor Smith who is always ready to go on an adventure or dig into more technical conversations about the random science questions that I come up with. Most importantly, I want to thank my wife, Allie, for her undying love and support during my time at UCLA. I couldn't have done this without her and the perspective that she provides.

With regard to the research that forms the foundation for this work:

Chapter 2 contains a version of: D. Richard, J. Jang, B. Çitmaci, J. Luo, V. Canuso, P. Korambath, O. Morales-Leslie, J. F. Davis, H. Malkani, P. D. Christofides, and C. G. Morales-Guio. Smart manufacturing inspired approach to research, development, and scale-up of electrified chemical manufacturing systems. *Iscience*, 26(6):106966, 2023.

Chapter 3 contains a version of: D. Richard, M. Tom, J, Jang, S. Yun, P. D. Christofides, and C. G. Morales-Guio. Quantifying transport and electrocatalytic reaction processes in a gatight rotating cylinder electrode reactor via integration of Computational Fluid Dynamics modeling and experiments. *Electrochem. Acta*, 440:141698, 2023.

Chapter 4 contains a version of: D. Richard, Y. Huang, and C. G. Morales-Guio. Recent advances in the electrochemical production of chemicals from methane. *Curr. Opin. in Electrochem.*, 30:100793, 2021.

Curriculum Vita

2015 **Associate of Science**, Magna Cum Laude
Northwest Arkansas Community College

2018 **Bachelor of Science, Chemical Engineering**, Cum laud
Department of Chemical Engineering
University of Arkansas, Fayetteville

2018-2019 **Post Bachelor Intern**
Los Alamos National Laboratory

2019-2023 **Graduate Student**
Department of Chemical and Biomolecular Engineering
University of California, Los Angeles

2020-2023 **Teaching Assistant/Associate**
Department of Chemical and Biomolecular Engineering
University of California, Los Angeles

2021 **Master of Science in Chemical Engineering**
Department of Chemical and Biomolecular Engineering
University of California, Los Angeles

Journal Publications

1. **D. Richard**, J. Jang, B. Çitmaci, J. Luo, V. Canuso, P. Korambath, O. Morales-Leslie, J. F. Davis, H. Malkani, P. D. Christofides, and C. G. Morales-Guio. Smart manufacturing inspired approach to research, development, and scale-up of electrified chemical manufacturing systems. *iScience*, 26(6):106966, 2023.

2. **D. Richard**, M. Tom, J, Jang, S. Yun, P. D. Christofides, and C. G. Morales-Guio. Quantifying transport and electrocatalytic reaction processes in a gatight rotating cylinder electrode reactor via integration of Computational Fluid Dynamics modeling and experiments. *Electrochemica Acta*, 440:141698, 2023.

3. B. Çitmaci, J. Luo, J. Jang, V. Canuso, **D. Richard**, Y. M. Ren, C. G. Morales-Guio, and P. D. Christofides. Machine learning-based ethylene concentration estimation, real-time optimization and feedback control of an experimental electrochemical reactor. *Chemical Engineering Research and Design*, 185:85-107, 2022.

4. **D. Richard**, Y. Huang, and C. G. Morales-Guio. Recent advances in the electrochemical production of chemicals from methane. *Current Opinions in Electrochemistry*, 30:100793, 2021.

5. K. Chintam, M. R. Gerhardt, A. M. Baker, **D. Richard**, M. S. Wilson, J. R. Flesner, T. Rockward, D. S. Hussey, J. M. LaManna, D. L. Jacobson, J.Rau, A. Z. Weber, and R. L. Borup. Imaging and modeling of passive water management in a miniature fuel cell. *Electrochemical Society Transactions*, 92(8):395, 2019

Chapter 1

Introduction

Since the industrial era, anthropogenic emission of greenhouse gases have globally increased the concentration of CO_2 in the atmosphere, leading to widespread effects on the global climate. These emissions have primarily been due to the prevalence of fossil fuels to provide energy and chemical feedstocks to growing nations worldwide. While the individual effect of a given process on the global CO_2 levels is insignificant, the sustained accumulation of CO_2 over many decades has overwhelmed the ability of natural processes on earth to remove CO_2 from the atmosphere. In fact, estimates suggest that the net flux of anthropogenic CO_2 emissions is roughly double the removal through natural processes on a global scale [1]. To address this issue, a global push to reduce fossil fuel use and increase utilization of clean energy sources has presented new challenges to the energy and chemical manufacturing industries. On one hand, clean energy sources, at their core, derive energy from the sun and typically produce energy in the form of electricity. One of the major challenges associated with these energy sources is that they are intermittent and require the development of large scale electric storage solutions. Many different methods are being investigated including battery, thermal, and hydroelectric storage [2]. On the other hand, many chemical production process that we rely on for common chemicals, use fossil fuels as feedstock to provide the carbon that is necessary to produce those chemicals. The obvious solution to this issue without

fossil fuels would be to capture carbon from CO_2 in the atmosphere, but doing so is extremely challenging and expensive with existing technology due to the dilute concentration of CO_2 in the atmosphere.

The technology that is most likely to provide solutions to both the energy storage and chemical feedstock issues caused by eliminating fossil fuels, is the development of new electrochemical processes. Electrochemistry provides the opportunity to utilize energy in the form of electricity to drive chemical reactions in ways that would be impossible with thermal catalysis, and the opportunity to implement separation processes along with the reaction [3]. Through the manipulation of the electric potential, the energy of the electrons at an electrode surface can be increased or decreased to control reaction rates, ions can be selectively removed or added to control thermodynamic equilibrium, and thermal balances can be established locally where the reaction is taking place [4]. However, many challenges exist to the development of industrial processes that utilize electrochemical techniques. Electrochemical systems consist of a complex mix of interactions between mass, charge, and heat transport that affect the observed reaction kinetics [5]. Decoupling these effects is especially difficult for reactions like CO_2 reduction that involve multiple steps and competing reactions. For reactions like these, traditional electrochemical methods of determining governing relationship, like Tafel slopes, are no longer adequate to describe the phenomena that govern selectivity and reactivity [6, 7]. As such, new methods of data collection and analysis must be developed to address the complexity of the electrochemical system of interest.

In this thesis, efforts to develop and apply such methods are presented. In Chapter 2, a framework for accelerating research and development in electrochemical systems is presented. This framework is inspired by Smart Manufacturing (SM) methods that are applied industrially to optimize and control complex systems, and consists of 4 phases. The first phase introduces enhanced sensing and automation to experimental reactors to enable the collection of large data sets. A higher degree of complexity requires the investigation of a large number of variables. Thus, to extract underlying relationships, a data set that is commensurate in size to the complexity of the

system will be needed. To accelerate the rate of data collection, automated sensors and control methods can be implemented. Data management strategies such as standardized data formatting and centralized storage in a designated database are also implemented at this stage to minimize the data curation needed in later phases. In phase 2 machine learning models are used to analyze the data sets collected in phase 1. These models can provide insights into relationships between key variables in the system and guide decision about what conditions to investigate further with multi-scale modeling in phase 3. These multi-scale models may include a combination of techniques from continuum scale computational fluid dynamics modeling, to Density Functional Theory, and are used together to gather intelligence about what is happening close to the electrode surface at scales that are difficult to probe experimentally. Methods developed to model the experimental system can then be used to inform the design of larger scale systems where the system performance can be tested *in silico* and optimized before real world testing. Together this framework provides a holistic approach to electrochemical system scale-up and examples are provided for how each phase of this framework has been applied to the investigation of electrochemical CO_2 reduction.

Following the introduction of the SM inspired framework, a detailed discussion of the multi-scale CFD modeling efforts for the rotating cylinder electrode reactor (RCE) is presented, along with the insights that these models have provided. Chapter 3 details the first stage of the modeling efforts which is focused on the hydrodynamics of the RCE. Since the hydrodynamics are what control mass transport to and from the electrode surface, modeling methods developed in this chapter are foundational to all future steps in the model development. Here we use the simple one electron transfer reduction of ferricyanide to probe the effects of the hydrodynamics on the electrochemical response of the RCE and compare the simulation results to experimental results to ensure model accuracy. With the accuracy of the simulation results verified against high quality experimental data, we then evaluate the influence of rotation speed on the structure of the hydrodynamic and diffusion boundary layers.

Having establishing the hydrodynamic foundation for CFD simulations in the RCE, Chapter 4

adds the hydrogen evolution reaction (HER) into the simulation. This reaction which involved the reduction of protons or water molecules to produce H_2, is ubiquitous to aqueous electrochemistry and plays a foundational role in modeling electrochemical reactions in the RCE. Additionally, motivation is provided for the investigation of buffer effects on HER. Simulating electrochemical reactions has presented numerous new challenges which have thus far prevented the successful simulation of more than one electrochemical reaction at appreciable rates. These challenges are discussed in detail along with solutions that have been identified. Although challenges persist, useful information about the conditions at the electrode surface can be gained by evaluating the successful simulations of the kinetically limited water reduction reaction and proton reduction under mass transport limited conditions. Results include the current density and potential profiles at the surface of the electrode, how the potential field changes as current density increases, and the influence of mass transfer and solution resistance.

The final two chapters shift away from the application of the SM inspired framework to electrochemical CO_2 reduction. Instead focus is placed on efforts to apply the same framework to electrochemical steam methane reforming (SMR). Chapter 5 provides motivation for the investigation of electrochemical activation of methane and reviews current developments in this field. As renewable sources of electric power become more affordable, the economics of electrochemical production of H_2 and other chemicals from methane become more attractive. As a result electrochemical activation of methane may offer an alternative path for the production of many common chemicals. The recent development of highly stable, selective, and conductive proton conducting ceramics shows promise in providing an electrochemical SMR process that can be commercialized. This technology also offer the potential for efficient coupling of SMR with other reactions such as nitrogen reduction to ammonia that would not be possible with other technologies.

Having identified proton conducting ceramic membranes for SMR as a technology of interest, Chapter 6 details efforts to apply SM techniques related to system automation and data connectivity to the design of an experimental system capable of performing electrochemistry with these

membranes. A system is designed from the ground up to allow control over feed gas flow rates and composition, steam fraction, system pressure and temperate, and applied electric potential and current. Appropriate sensors and controllers are interfaced with a centralized LabVIEW based user interface that allows for automated system control, online process monitoring, and standardized data collection. Details of the system design and implementation are discussed along with initial experimental results and challenges that were faced in the design of the system. This system involves a total of 18 automated sensors and controllers and is an excellent demonstration for the application of phase 1 in the SM inspired framework for electrochemical systems.

Overall, this thesis provides a detailed understanding of the SM inspired framework for accelerating research in electrochemistry. While Chapter 1 explains the framework in detail, the following chapters provide specific examples of its application in the lab. For those looking to apply the framework to their own experiments, this thesis provides a basis to start from and a better understanding of the challenges they may face along the way.

Chapter 2

Smart manufacturing inspired approach to research, development, and scale-up of electrified chemical manufacturing systems

A growing coalition of countries, cities, businesses, and other institutions are pledging to achieve net-zero emissions by 2050 or earlier. Meeting this ambitious goal will require cutting greenhouse gas emissions as close to zero as possible, while also implementing carbon offset technologies to capture persistent emissions from the atmosphere to close the carbon cycle. A major factor enabling this shift to a carbon-neutral economy is the emergence of cost-effective renewable energy sources such as photovoltaics and wind turbines that harvest renewable energy in the form of electricity. The energy landscape in 2050 is expected to be dominated by renewable energy technologies. To enable the transition to an electric-based energy landscape, Power-to-X and X-to-Power technologies will be needed to decouple power from the electricity sector for use in other sectors of the economy: such as transportation fuels, industrial chemical production, grid-scale energy storage, and eventually carbon capture (Fig. 2.1 (A)). The development and scale-up of Power-to-X and X-to-Power technologies is viewed as a promising solution to meet strong decar-

bonization targets while enabling the high penetration of renewables into the different sectors of the economy [8].

Great progress has been made in the electrification of residential and commercial heating, as well as the electrification of industrial furnaces and the use of green hydrogen for metal refining [7, 9–12]. However, progress in the scale-up of emerging technologies for the electrification and decarbonization of hard-to-abate sectors, such as the production of fuels and chemicals, has been slow due to the inherent complexity of these systems [13–18]. Electrochemical systems involve many simultaneously interacting phenomena drawn from various aspects of physics and chemistry, and require a disciplined learning of the multiple variables affecting the process [19]. Understanding the underlying effects of thermodynamics, reaction kinetics, and transport phenomena occurring inside an electrochemical system, and how they interact across different length and time scales, is one of the greatest engineering challenges inhibiting the Research, Development, and Deployment (RD&D) of industrial-scale electrified chemical manufacturing systems. Current research methods attempt to extrapolate an understanding of these complex phenomena from small, simple datasets [20–23]. This approach has so far prevented a holistic understanding of the system. Instead, large datasets that are commensurate to the complexity of the system should be used. This will require the development of new techniques to enable efficient handling of large datasets, the extraction of useful relationships, and the development of descriptive multi-scale models. Successful application of these techniques in research will be crucial in accelerating the scale-up of electrosynthesis technologies from bench-scale reactors operating at the watt scale to industrially relevant systems operating on the terawatt scale in a timely manner (Fig. 2.1 (B)).

In the following sections, we will examine the research challenges that have thus far prevented the scale-up of electrochemical reactors for CO_2 reduction, and discuss why traditional research methodology may prove to be unsuccessful in providing the understanding that is necessary to scale these systems. Having identified the challenges of using traditional research methodology, we then discuss how the inspiration for a more efficient approach can be taken from smart manufacturing

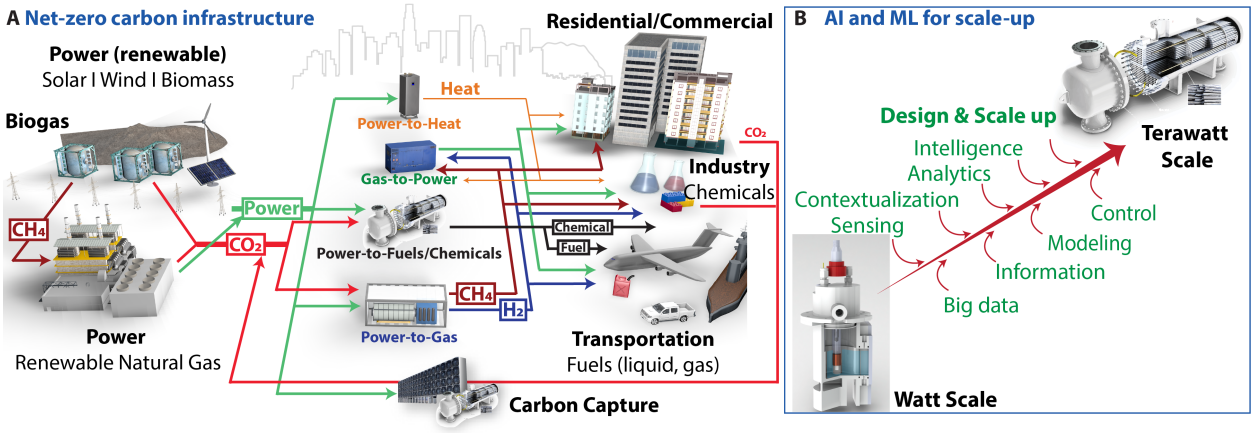

Figure 2.1: Application of AI and ML to electrolyzer scale-up can enable a net zero carbon future. (A) Vision of a net-zero carbon future. (B) AI and ML for scale-up of CO_2 electrolyzers.

(SM) methods that have been applied successfully to complex industrial processes. The framework of the SM-inspired research methodology is presented, followed by detailed examples of how it has been applied in efforts toward the scale-up of electrochemical CO_2 reduction devices. In this chapter, we highlight how techniques such as automation, connectivity, and advanced modeling methods can be seamlessly integrated with experimental processes to accelerate the scale-up of electrochemical systems.

The discussion of challenges toward the scale-up of electrochemical reactors for CO_2 reduction presented in this chapter is not exhaustive. Learning curves for water electrolyzer technologies have shown that high cost across the entire value chain have limited their rapid deployment. Electricity is the dominant cost for on-site production of green hydrogen, but the journey to lower renewable costs is already underway. Efforts are shifting to the second largest cost for green hydrogen: electrolysers. Green hydrogen production as well as electrolyzer manufacturing benefit from economies of scale. However, the lack of infrastructure and a skilled workforce to sustain gigawatt (GW) scale manufacturing have limited the current electrolyzer manufacturing capacity to under 8 GW/year [24]. In comparison, solar modules manufacturing capacity in 2021 was already 240 GW/year. The same challenges in the scale-up of manufacturing capacity are expected to limit CO_2 electrolyzer manufacturing, even if all the fundamental research challenges presented in this

chapter were suddenly resolved.

2.1 Challenges in existing approach to RD&D of CO_2 electrolyzers

The production of fuels and chemicals from carbon dioxide, water, and renewable electricity in an electrochemical reactor has been proposed as a viable approach to the reduction of CO_2 emissions associated with the chemical manufacturing sector [25]. Most importantly, when paired with carbon capture technologies and renewable energy sources, electrochemical CO_2 reduction offers the unique possibility of closing the carbon cycle by recycling carbon from the atmosphere as feedstock that supports chemical manufacturing industries [26]. Industrial scale adoption of CO_2 electrolysis would enable many existing processes based on carbon feedstocks to continue operation while minimizing the need for new chemical production and distribution infrastructures. Most notable examples include production of fuels for transportation, base chemicals for production of plastics, and grid-scale liquid-fuel energy storage for intermittent renewable energy sources. As such, interest in developing this technology has been increasing steadily for the last decade. While high current densities as high as 3.37 A cm^{-2} have been reported [19], durability remains low with current density decreasing quickly after tens of hours, and when the scale of the system is increased. To achieve efficient and low-cost production of chemicals at large scales, CO_2 electrolysis technologies will need further improvements in durability, efficiency, conversion, product selectivity, and overall system design as well as the development of efficient direct air capture technologies to provide carbon feedstocks. One of the key roadblocks to understanding how to scale-up these systems is the development of a practical kinetics-transport model of electrochemical CO_2 reduction. The development of such a model has thus far eluded the scientific community due to the convolution of different interactions within CO_2 electrolyzer systems.

Many complications preventing these improvements arise from the chemistry itself. While

various transition metals have been shown to effectively reduce CO_2 to CO or formate, Cu is the only known single-element metal to enable conversion to C_{2+} products such as olefins and liquid alcohols at an appreciable rate. Because Cu offers the potential for one-step production of valuable precursors such as ethylene, ethanol, and propanol, Cu-based catalysts have been the main material of interest for electrochemical CO_2 reduction. A total of 16 different chemicals have been identified as products, with CO and hydrocarbons (CH_4 and C_2H_4) observed in the gas phase, and oxygenates such as formate, ethanol, n-propanol, acetate, and aldehydes observed in the liquid phase [27]. CO is the key intermediate formed via two electron transfer steps and can be further reduced to CH_4, methanol, and C_{2+} products. However, the kinetics associated with each intermediate step and the species involved in the reactions are difficult to elucidate conclusively, and various mechanistic pathways have been proposed without collective agreement on a detailed mechanism within the research community [28].

The existence of competing reactions further complicates understanding the electrochemical CO_2 reduction mechanism. Hydrogen evolution reaction (HER) is inherent in the nature of aqueous electrochemistry, as proton sources are required to reduce CO_2. In aqueous electrolytes, the proton sources can be hydronium ions, molecular water, and buffers that relay protons to the surface of the electrode. Formate is another product pathway that proceeds in parallel to the CO production pathway. The production of hydrogen and formate is affected by the CO_2 and bicarbonate buffer chemistry, in which bicarbonate can act as a proton donor and buffer in the bulk electrolyte. [29] This homogeneous buffering chemistry makes mass transport characteristics nonlinear for key reaction species including CO_2, bicarbonate, and hydroxide, creating an additional layer of complexity in describing the electrochemical environment near the electrode surface. Even the formation of the simplest two electron transfer products (H_2, formate, and CO) consists of at least three elementary steps (i.e., adsorption, two-electron-proton transfer steps, and desorption) which cannot be readily described by the Butler-Volmer equation, especially when concentrations of reactive species in the vicinity of the reaction front are unknown.

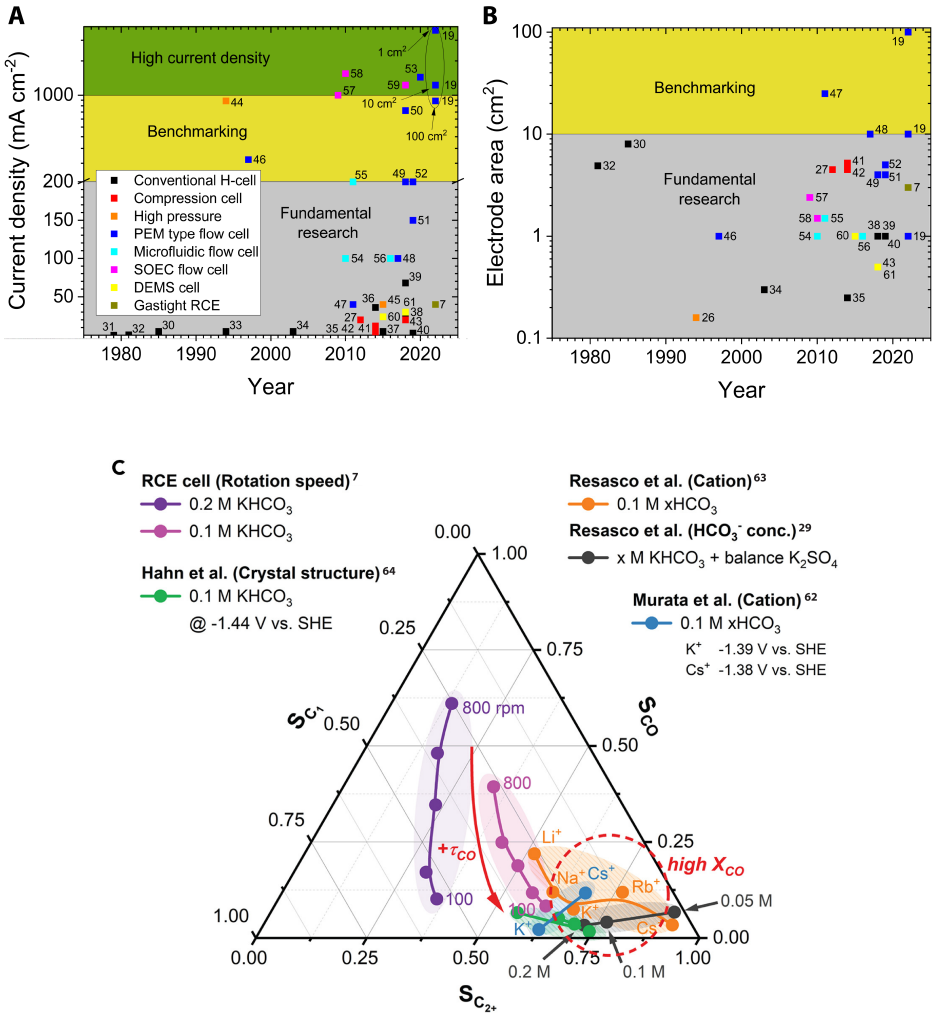

Figure 2.2: Data highlighting the difficulty in CO_2 electrolyzer scale-up and the significance of mass transport. (A) Current densities for select experimental electrochemical CO_2 reduction studies since Hori's initial reports. (B) Cathode geometric areas for the same studies shown in (A). Cell types listed in (A) and (B) are primarily categorized as identified in their respective publication. However, H-cell and compression cell classification is not entirely clear, so the following criteria were considered for classification. H-cell is a two or three compartment cell where high electrode area to electrolyte volume ratio is not a priority, and where the cross section area of the membrane separating cathode and anode is small relative to the cathode compartment cross section area. The compression cell is a small form factor reactor targeting high electrode area to electrolyte volume ratio, where the components of the cell are sandwiched together with compressive force to provide gas and liquid-tight connections. References for H-cell [30–40], compression cell [27, 41–43], high pressure [44, 45], polymer electrolyte membrane (PEM) type flow cell [19, 46–53], microfluidic flow cell [54–56], solid oxide electrolyzer (SOEC) flow cell [57–59], differential electrochemical mass spectrometry (DEMS) cell [60, 61], and the rotating cylinder electrode (RCE) reactor [7]. (C) A ternary plot showing that the data collected in common reactors used for electrochemical CO_2 reduction falls in the region representative of stagnant flow conditions inside the RCE, suggesting that mass transport is poorly defined in these reactors [7, 29, 62–64].

While the products of electrochemical CO_2 reduction were first analyzed completely by Hori and co-workers [30], this process did not gain mainstream attention until the last decade. In the time since Hori's results were published, the majority of research has been performed using an H-cell configuration with low current density. These experiments were conducted with the intention of investigating the fundamental relationships governing electrochemical CO_2 reduction. Early reports suggested that mass transport significantly affects the selectivity and rates of CO_2 reduction [44, 65]. To overcome mass transfer limitations, flow cell-type reactors and high-pressure CO_2 electrolyzers were investigated early on. Systems showing high current density near 1 A cm^{-2} were demonstrated as early as the 1990s [44]. Flow cells, in particular, have consistently shown current density significantly higher than other cell types due to the improved mass transport of CO_2 to the catalyst near the three-phase boundary. These systems are better used for bench- marking catalysts in the sense that their activity can be studied under reduced mass transport limitations. However, scaling these reactor types remains difficult due to the lack of fundamental understanding of the underlying relationships governing CO_2 reduction rates and selectivity as the conversion of CO_2 increases along the flow path. One example that clearly demonstrates this issue is circled in the top right corner of Fig. 2.2 (A). Three data points show the current densities obtained for three flow cells with the same catalyst when the geometric surface area of the electrode is increased from 1 to 10 and then 100 [19]. The 1 cm^2 electrode reaches current densities of 3.37 A cm^{-2}. However, when the system is scaled to an electrode area of 10 and 100 cm^2, the current densities quickly decrease to below 1 A cm^{-2}. Research in electrochemical CO_2 reduction is still very much in the fundamental research stage, as demonstrated by the fact that nearly all research is still conducted with electrode surface areas of less than 10 cm^2 (Fig. 2.2 (B) and that attempts of scaling these systems typically resulted in significant performance losses. To move beyond this stage, the development of selective and efficient electrochemical processes will require advances in both catalyst and device/process design [7, 28]. At large, the research community has generally focused on the design of catalysts or devices separately, and rarely on understanding the coupling of both.

The widespread adoption of compression-type H-cell reactors highlights this trend. The introduction of the compression cell [27] ushered in a flood of fundamental research due to the ease of experimentation and improvement in the sensitivity for detecting C_{2+} liquid products. However, this reactor is limited in the fact that it does not provide control over mass transport. Because of this, the electrochemical conditions near the electrode surface are poorly defined. The implications of this limitation are apparent when data generated in this electrochemical reactor is compared with results from a rotating cylinder electrode (RCE) reactor, in which mass transport can be controlled. Fig. 2.2 (C) shows a ternary plot for product selectivity to CO, C_1, and C_{2+} products denoted as S_{CO}, S_{C_1}, and $S_{C_{2+}}$, respectively. These selectivities relate to the fractions of CO_2 molecules consumed in producing the three groups of products (data extracted from Jang et al. [7]). The purple and the pink curves show data collected with the RCE cell using 0.2 and 0.1 M potassium bicarbonate electrolytes, respectively, at a constant potential of -1.41 V vs. the standard hydrogen electrode (SHE) while varying the electrode rotation speed. As the rotation speed decreases from 800 to 100 rpm, the mass transport coefficient of all species to and from the electrode surface decreases. This decrease in the mass transport coefficient also applies to the intermediate CO, slowing down the removal of CO generated on the surface of the electrode and increasing the residence time of CO (τ_{CO}). The increase in τ_{CO} increases the probability of further reducing CO to C_1 or C_{2+} products, and reduces the probability of the intermediate CO being released as a final product [7]. This trend in the selectivity shift is clearly shown for data obtained in the RCE cell. On the other hand, in electrochemical reactors with poor mass transport characteristics, τ_{CO} is likely very long, although this cannot be well-defined, resulting in a high conversion of CO to its further reduced products (X_{CO}). The selectivity curves from these reactors populate only the bottom-right corner of the ternary diagram (Fig. 2.2 (C)) under electric potentials similar to experiments from the RCE cell, in the range of -1.38 to -1.44 V vs. SHE. This brings up an important realization that what we measure experimentally is reactor kinetics, not reaction kinetics.Thus, the use of Tafel analysis to study reaction mechanism in CO_2 reduction experiments on copper electrodes, for example,

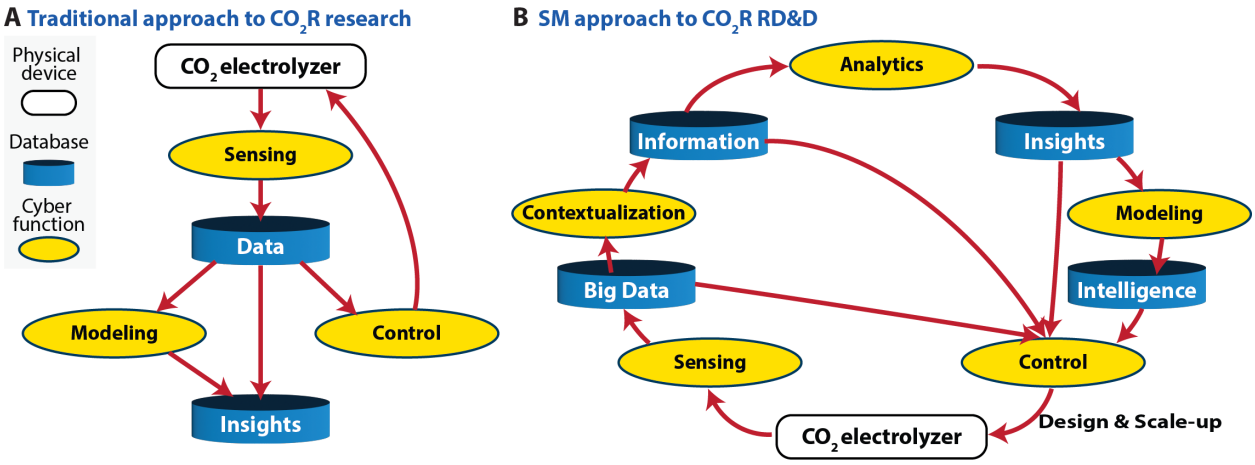

Figure 2.3: Comparing the traditional research workflow to smart manufacturing (SM). (A) A visual representation of how research is traditionally conducted, showing how control over the electrochemical CO_2 reduction reaction is attempted based on results from small datasets and modeling is often conducted separate from data interpretation. (B) A visual representation of the SM approach, showing how connectivity of information from all stages of the RD&D process aid in providing the knowledge necessary to develop the control of CO_2 electrolysis necessary to scale-up.

does not have any scientific foundation. Gregoire and co-workers have also recently shown how hydrodynamics in the electrochemical cell determine the apparent Tafel slope measured during electrochemical CO_2 reduction on a copper electrode, further demonstrating that mass transport is on equal footing with catalyst active sites in determining reaction mechanisms and the ensuing product distribution [6]. Thus, the importance of collecting data across a large operational parameter space under well-controlled transport characteristics in electrocatalytic reactors cannot be understated, as this is the only manner in which we will be able to extract intrinsic kinetics from reactor kinetics.

In addition to the effect that reactor selection has on the quality of data collected in experimental CO_2 electrolyzers, it becomes apparent that the traditional research approach taken to the study of CO_2 electrolyzers may be inadequate to fully parameterize the kinetics for electrochemical CO_2 reduction reactions. For comparison, a generalization of the traditional approach is presented in Fig. 2.3 (A). In this approach, data is collected from an experimental reactor, using various sensors, and insights are extracted from relatively small datasets. However, these insights often do not

translate readily to larger-scale systems, as is becoming evident in the CO_2 electrolyzer research community. In CO_2 electrolysis, this is primarily because the results collected in experimental systems are specific to the reactor properties rather than reaction properties. This is demonstrated by the fact that identical catalysts will often show differing performances in different experimental reactors. Frequently, density functional theory (DFT) or microkinetic modeling is used to explain the results or to try to better understand what is happening at time and length scales that are inaccessible to experiments in the real system. Multi-scale modeling can be a powerful tool for understanding what is happening in a reactor. However, accurate, high-fidelity experimental data and an excellent understanding of the experimental conditions in the reactor are required to fully parameterize these multi-scale models. In many instances, there is a disconnect between modeling and experimental groups that prevents this from happening, leading to models that simply fit the data. As shown here, difficulty in collecting high quality data and the typical method of conducting research, make it difficult to conclusively understand the fundamental relationships governing the performance of CO_2 electrolyzers. Accelerating the scale-up of these systems requires an adjustment to the current research approach.

2.2 Smart manufacturing background and context for applications in scale-up research

SM refers to a holistic approach to process optimization, where advanced sensing techniques are paired with robust data handling and modeling strategies to provide rationally optimized system operations, improved safety and security, and reduced waste [66–69]. Application of SM is built on the idea that optimal control can be achieved through the integration of advanced operations technologies (OT) and information technologies (IT) to develop streamlined data acquisition, handling, and interpretation processes that interconnect the individual parts of a process [66, 70–73]. While implementation of SM can look very different between two systems [74], the approach can

be generalized by Fig. 2.3 (B). Here we see that optimal control with SM begins with sensing that allows for the collection of large datasets. Sensors for a given process should be chosen to provide useful and reliable data that can be collected in an automated fashion. Sensors applied in this way enable the collection of large datasets for modeling and frequent input updates for real-time system control [69]. For example, a thermocouple senses the temperature and produces a voltage signal that is recorded as data. However, for these data to be useful, they need to be contextualized. By tying the data to the sensor type and the characteristics of the process, information can be extracted to improve control of the system. An example of this would be taking the data from the thermocouple and contextualizing it with the knowledge that the thermocouple is located in a liquid-filled vessel, and that a certain voltage signal correlates with a specific temperature. By contextualizing these data with knowledge of the process and the sensor, we gain the information: in this case, the temperature of the fluid in the vessel. Next, analytics provide insights to further optimize control of the process. Using the thermocouple example again, we could analyze the change in temperature over a period of time to gain insight about the trajectory of the fluid temperature with time. Fluid temperature could also be tied to other sensor types, such as pressure sensors, to further evaluate the performance or safety of the overall system using a combination of hundreds or thousands of sensors across a manufacturing process. With the immense dataset provided by these sensors, modeling can provide an added degree of intelligence by building on the knowledge from past data to predict the system's future behavior. Models can also provide information about the current state of the system that cannot be sensed directly. Examples of how advanced modeling can be applied industrially include the prediction of catalyst lifetime or equipment failure [75], adjusting for external factors such as changes in real-time feedstock, product and utility pricing [76], or setting optimized system control set-points based on predicted performance [77–79]. Benefits of implementing SM in the industry have been demonstrated for a wide range of applications [80], and industrial adoption has been successful for improving efficiency and safety in large scale industrial applications [81]. It stands to reason that similar benefits might be gained by applying the same

principles and methodologies to RD&D of emerging electrosynthesis technologies.

Additionally, using SM techniques at the research stage can help enable SM implementation when the technology is scaled-up [82]. Many chemical manufacturing processes utilize aging infrastructure, and were not designed with SM in mind. Even though the technology and methods have been available for decades, the industry has been surprisingly slow to adopt SM regardless of the proven benefits. Hesitancy to adopt SM remains, primarily, due to the technical debt that must be repaid before legacy systems can be converted to an SM infrastructure [83, 84]. In the context of this discussion, technical debt can be separated into two main components, intellectual and physical, that describe the costs associated with upgrading existing systems to SM systems. First, the intellectual component of technical debt comes from a lack of trained individuals who are educated on SM methods and know how to implement and maintain them in the industry. Time, energy, and financial backing are required to train personnel in SM practices, and educational institutions along with industry partners must develop programs to supply this workforce [85]. As such, technical debt is not only associated with the cost of hiring a technically skilled labor force, but also a shift in the education system to supply skilled individuals [81]. Second, the physical component of technical debt includes the hardware and software upgrades necessary to implement SM techniques. This may include costs associated with adding sensors and the infrastructure to collect data from them or purchasing software to process data and the equipment to run the software. In many cases, the cost associated with implementing SM may simply be too high to justify retrofitting an existing process, especially for smaller businesses that lack the necessary financial backing. However, the physical component of technical debt can be eliminated for new processes if they are designed from the start with SM in mind. This provides an exciting opportunity for the development of electrochemical manufacturing technologies that will utilize SM industrially. Not only can the implementation of SM techniques in research of advanced reactor technologies accelerate the experimental process by streamlining data acquisition and interpretation, but implementation at early stages of development and scale-up can enable systems to be designed from the

start to utilize SM once commercialized.

2.3 Framework for a smart manufacturing inspired approach to RD&D

As an example of how the SM approach can be applied in research, the framework developed for electrochemical CO_2 reduction research is provided in Fig. 2.4 [86]. The individual steps defined in Fig. 2.3 (B) are shown at the top of the framework in Fig. 2.4 for direct comparison, while the parts of the process involved in each step are defined below. This framework can be separated into four distinct phases that are highlighted by the background color.

Blue indicates Phase I where the experimental reactor is adapted to automate data collection and improve connectivity to enhance experimental throughput, data accessibility, and data collection. This requires the selection of a reactor that can provide high-fidelity data suitable for modeling. That is, a reactor with well- defined transport characteristics. Phase II is highlighted in orange, where machine learning (ML) and artificial intelligence (AI) are utilized along with dimensional analysis to accelerate data processing and enable the extraction of underlying relationships between inputs and outputs. These relationships are used to design real-time control schemes and build predictive models for the reactor. Real-time control of the reactor is used to validate the extracted relationships, as control will not be possible without an adequate understanding of the relationships governing the reactor performance. Green highlights Phase III, where multi-scale modeling techniques utilize first principle relationships and the relationships extracted in Phase II to build predictive models of the reactor. This step develops modeling methods to capture the local phenomena occurring at the gas/liquid, liquid/solid, and gas/liquid/solid interfaces that will be used in parameterizing improved reactor designs [5]. Finally, red highlights the last step, where insights gained from the aforementioned modeling methods are utilized to guide the rational design of prototype reactors. These designs can then be tested in silico using the methods developed

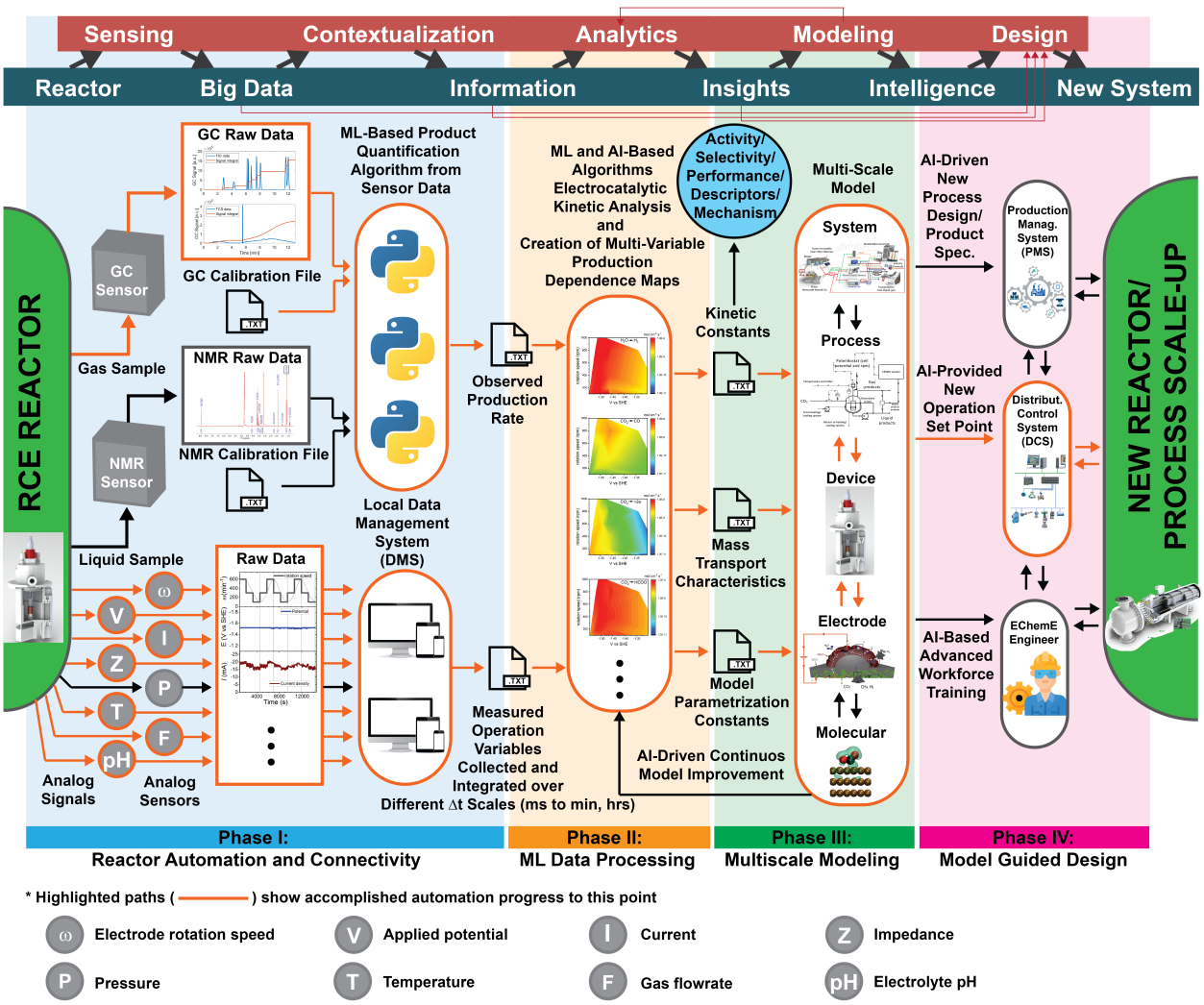

Figure 2.4: The smart manufacturing (SM) inspired framework for research. A framework for the application of the SM approach to accelerate scale-up and development of CO_2 electrolyzers. Adapted [86], Copyright 2022, with permission from Elsevier.

in Phase III before actual construction, reducing cost and time requirements. This is an iterative process that can then be applied to the prototype reactor at each scale and used to accelerate further scale-up to more industrially relevant systems over multiple iterations. Multi-scale models are also key for the workforce training of electrochemical engineers. The following sections will discuss in detail how this framework has accelerated progress toward the goal of enabling the scale-up of electrochemical CO_2 reduction technologies.

2.4 Lab-scale reactor selection for CO_2 reduction research

The first step in applying the SM framework to RD&D of CO_2 electrolyzers is the identification of process- relevant variables. Significant variables that are common to most fuel and chemical manufacturing processes include pressures, temperatures, flow rates, and composition. However, electrochemical systems require additional variables to be fully characterized, including electric potential, current, and impedance. Other factors that must be considered in the design of larger-scale electrochemical reactors include the effects of chemical and electrical interfaces, charge, heat and species transport, the presence of multiphase interfaces, and the composition of the electrolyte [87]. While the complexity of these systems makes them ideally suited for utilization of an SM inspired approach, application of the framework requires a lab-scale system designed to allow individual manipulation of each relevant process variable and efficient collection of large datasets.

Several experimental electrochemical reactors exist for investigating electrocatalysis, but many of these systems have limitations that make them less than ideal for investigating CO_2 electrolysis. The compression cell was introduced to improve product detection of liquid products by increasing the electrode-to-electrolyte ratio compared to traditional H-cell reactors. However, the compression cell lacks control over hydrodynamics and mass transport conditions. Flow cells are utilized to overcome mass transport limitations, but are too complex to extract a fundamental understanding of the underlying phenomena. Rotating disk electrode (RDE) reactors have been widely adopted

for the investigation of electrocatalysis because of the well-understood mass transport effects provided by the Levich equation. However, RDE electrodes are restricted to diameters of less than 5 mm and laminar flow conditions. In this case, the small electrode area prevents liquid product quantification.

A promising alternative reactor type that provides control over mass transport while also maintaining a high electrode area to electrolyte volume ratio is the gastight rotating cylinder electrode (RCE) reactor. While the current system is limited to a small range of temperatures and pressure, it is uniquely suited to decouple transport effects from intrinsic electrode kinetics. The main advantages provided by the RCE can be attributed to the high degree of symmetry. Symmetry ensures that all points on the electrode surface are exposed to the same hydrodynamics, resulting in a uniform and controllable mass and heat transport across the entire surface. This is especially true for the hydrodynamics in the electrocatalytically active region of the reactor, within a few micrometers of the electrode surface. Furthermore, the mass and heat transport can be controlled by simply adjusting the cylinder rotation speed. Changing the rotation speed increases the velocity gradient and reduces the boundary layer thickness, enhancing mass and heat trans- port to and from the electrode surface [5]. By controlling the rotation speed and evaluating the change in rates and selectivity, the timescales of the intrinsic kinetics and transport processes can be decoupled from each other. This allows the determination of the intrinsic reaction kinetics rather than the reactor kinetics that have been measured in other reactor configurations. Additionally, the symmetry of the RCE means that the hydrodynamics of the RCE is independent of the cylinder length, which enables the use of a large surface area electrode while ensuring uniform mass transport conditions and current densities. This enables the system to attain high total reaction rates, resulting in more easily detectable liquid products. The RCE is ideally suited to experimental studies that require mass and heat transport effects to be decoupled from kinetics, thus providing the information necessary to optimize the conditions in larger-scale designs. However, it should be noted that the RCE is not intended to represent the design of a larger-scale system, and other specialized reactor de-

signs may be needed to investigate relevant phenomena other than mass and heat transport as these systems are scaled-up.

2.5 Application of Automation and connectivity for enhanced data collection and processing

After identifying an appropriate reactor, the next step is to integrate automation and data connectivity in the reactor system. At the lab scale, data collection can be tedious and time-consuming. As such, automation efforts should be focused on two results: elimination of time-consuming, human-performed tasks and improvement of data collection reliability and accessibility. Process-relevant variables, identified in the initial analysis of the system, should be used here to identify what data can be collected through automated methods. This will support the efficient collection and management of large datasets to cover a wide parameter space. Recently, efforts have been growing to automate workflows in the lab using high- throughput screening and experimentation, as well as to develop self-driven laboratories that use ML to guide automated test systems [88]. Although primarily developed for material discovery [89], drug and vaccine development [90], and optimization of synthesis techniques [91], a general push in the field to increase throughput through automated techniques will be beneficial for a wide range of applications. Indeed, it can be argued that most efforts in the automation of data collection, digestion, contextualization, and modeling can be mapped out eventually against the SM approach to RD&D in Fig. 2.3 (B).

There are three modes of data collection: fully automated, semi-automated, and manually recorded. Examples of easily automated data types for electrochemical CO_2 reduction reactors [86] are displayed in green in Fig. 2.5. These include potential, current, electrode rotation speed, temperature, and CO_2 gas flow rates. Other data types, such as product concentrations, may require a degree of manual interaction for data collection or interpretation. Establishing automation and data connectivity with experimental systems re- quires an initial time investment, but will quickly

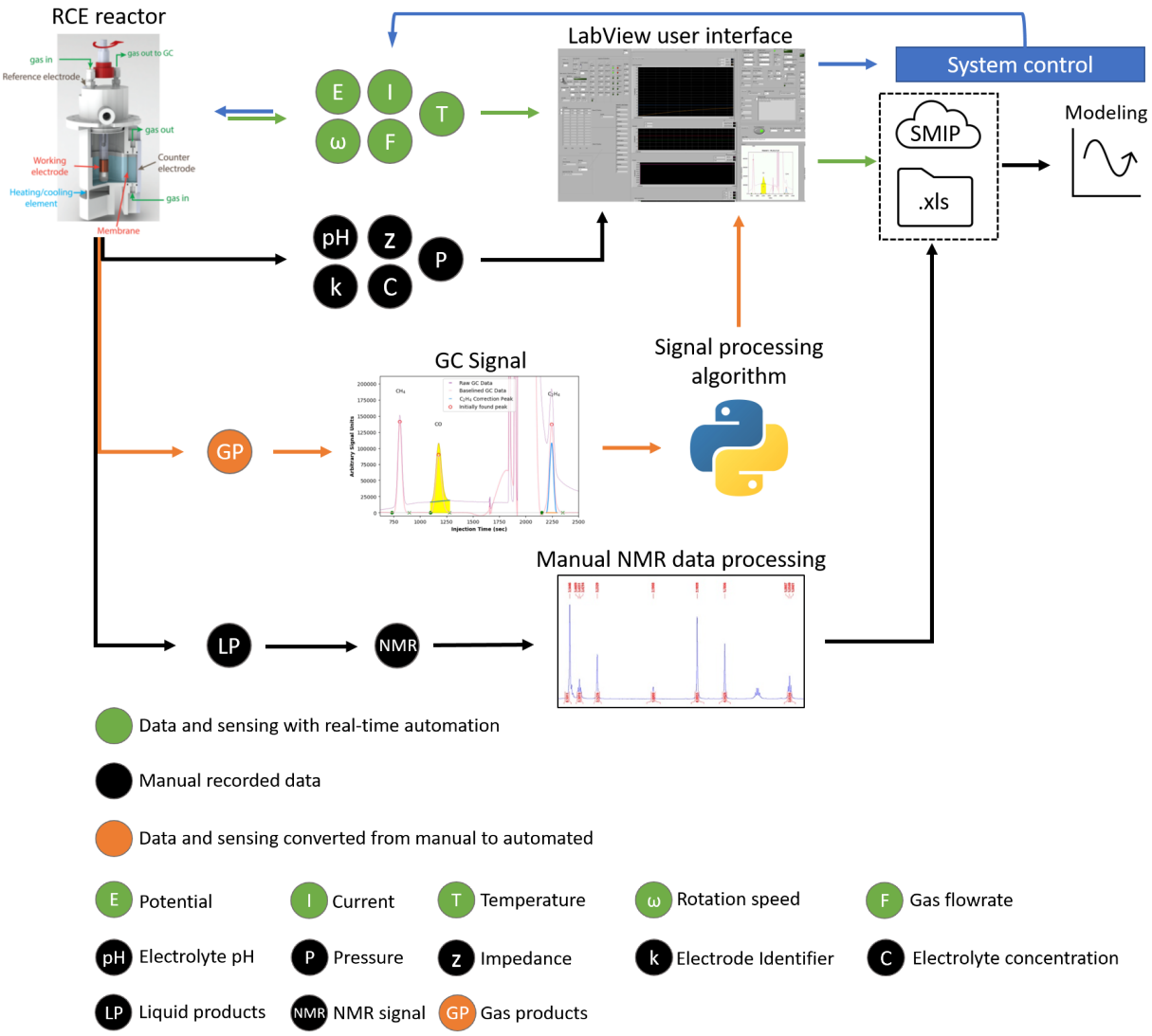

Figure 2.5: Automation of the experimental CO_2 electrolyzer. An overview of data collection, interpretation, and utilization within the experimental electrochemical RCE system showing how automation was incorporated for different data types.

pay for itself when collecting large datasets.

An example where automation significantly improved the workflow in CO_2 electrolysis research, is the automation of data collected using a gas chromatograph (GC). Before automation efforts, GC results were manually integrated using GC-specific software. In a typical experiment, four GC injections were measured approximately 20 min apart. While the physical task of integrating and logging the data from an injection only took 5–10 min, the intermittency of this task and the short length of time between each injection made it difficult to conduct outside work during experiments. To automate the GC data collection, a Python- based script was used to automatically baseline the GC spectra, identify peaks, and extract product concentrations (orange path in Fig. 2.5). This Python script was connected with a LabVIEW user interface that would upload data in real-time to the Clean Energy Smart Manufacturing Innovation Institute (CESMII) Smart Manufacturing Innovation Platform (SMIP) for centralized data storage, as explained by Çitmaci et al [86]. With the help of OT/IT specialists, these data collected through the LabVIEW interface were also connected with equipment profiles in the SMIP that connected the data to information about the individual sensor they were collected from, thus providing context for the data generated. From this platform, data can be easily accessed in a centralized location and in a standardized format along with relevant sensor in- formation, which is very important when building models of the reactor performance. This setup has been demonstrated in the real-time control of ethylene concentration in the RCE reactor effluent using proportional integral (PI) control [76] and multi-input-multi-output (MIMO) control of ethylene and CO concentrations [92].

Data types that are typically collected manually include tasks such as recording sample preparation methods or material properties. These types of data are often recorded once at the beginning of the experiment. However, models may need to access these data for contextualization, so they should be tied to real-time data collected during experiments. This data type can also be integrated with the online data collection with a centralized user interface like LabVIEW. Data such as electrolyte pH, pressure, impedance, electrolyte concentration, and the unique identifier for the

reference electrode can be entered once at the beginning of the experiment and automatically connected to the real-time data when transferred to the SMIP. In the CO_2 electrolyzer system, the only data type not automated is nuclear magnetic resonance (NMR) measurements of the liquid product composition. Since these data are processed ex situ, the data must later be entered manually (black path in Fig. 2.5). However, data collection for liquid products could be automated using high-performance liquid chromatography in the future.

The principles of automation and connectivity are broadly applicable for accelerating research by enabling more efficient data collection and accessibility. Many demonstrations of this principle have proven useful, especially in the discovery of catalysts and development of new materials [93–95]. Automation of data collection and storage has shown promise in basic research and should be implemented when possible to reduce the need for human interaction and the possibility of human error, to streamline the process of data collecting, and to improve management of large experimental datasets.

2.6 Application of machine learning to lab-scale reactor modeling and control

ML allows modeling, control, and optimization in CO_2 electrolyzer development. The collection and structuring of data must be designed well and should be pre-processed before the models are built. For both a dynamic and steady-state model, experimental conditions for generating training data should be comprehensive. Training data should include data from the highest and lowest operational limits, and safety can be increased by adding data points from slightly higher and lower operational input regions. For example, the electric current values of an electrolyzer might be higher than the training data limits, depending on surface potential. Furthermore, the data collection points should be well-distributed. If the training set is considerably more populated around a specific operational region and sparsely sampled around other operational regions, the

model is not expected to generalize well to all conditions. Thus, a more balanced dataset is the objective of designing experiments. On the other hand, preprocessing encompasses, but is not limited to, techniques such as outlier detection and correlation extraction. A correlation matrix is an effective way of exploring linear relations between experimental parameters. By checking covariance and standard deviation for two parameters, it is possible to gain intuition about the process. However, it is important to keep in mind that a correlation matrix might not be efficient in very nonlinear processes. Jensen and co-workers [96] automated an experimental flow reactor system for nucleophilic aromatic substitution of morpholine onto 2,4-dichloropyrimidine reactions to estimate kinetic parameters. A correlation matrix approach was used on the effects of pre-exponential factors and activation energies of 4 kinetic constants to comprehend the uncertainties in kinetic parameter predictions. An example of a correlation matrix for CO_2 electrolysis in the RCE reactor is shown in Fig. 2.6 (A). This correlation matrix is based on steady-state data for two process inputs (surface potential and catalyst rotation speed) and nine products. The intuition about process variable correlations provided by relative gain array (RGA) can be used at early stages to inform the building of models.

An ML method that might be used for building steady-state operational models is feedforward neural networks (FNN), due to their ability to capture complex nonlinear relationships. Since FNNs are high-fidelity models, they can easily overfit data, especially for small datasets. In the electrochemical CO_2 reduction, FNN was used to model the steady-state production of thirteen product species and oxygenate selectivity [97]. Given the large number of product species and reactor variability, an FNN was chosen for this model because the steady-state performance of the reactor is assumed to be independent of time. The inputs to the FNN are the applied potential and rotation speed since these are independent variables that quantify the kinetic and mass-transfer rates, respectively. To improve model prediction, the FNN loss function was designed to account for the statistical variability of the data. This FNN is trained to maximize the probability that the model predicts the data. Specifically, the loss function is the mean-squared error, but each

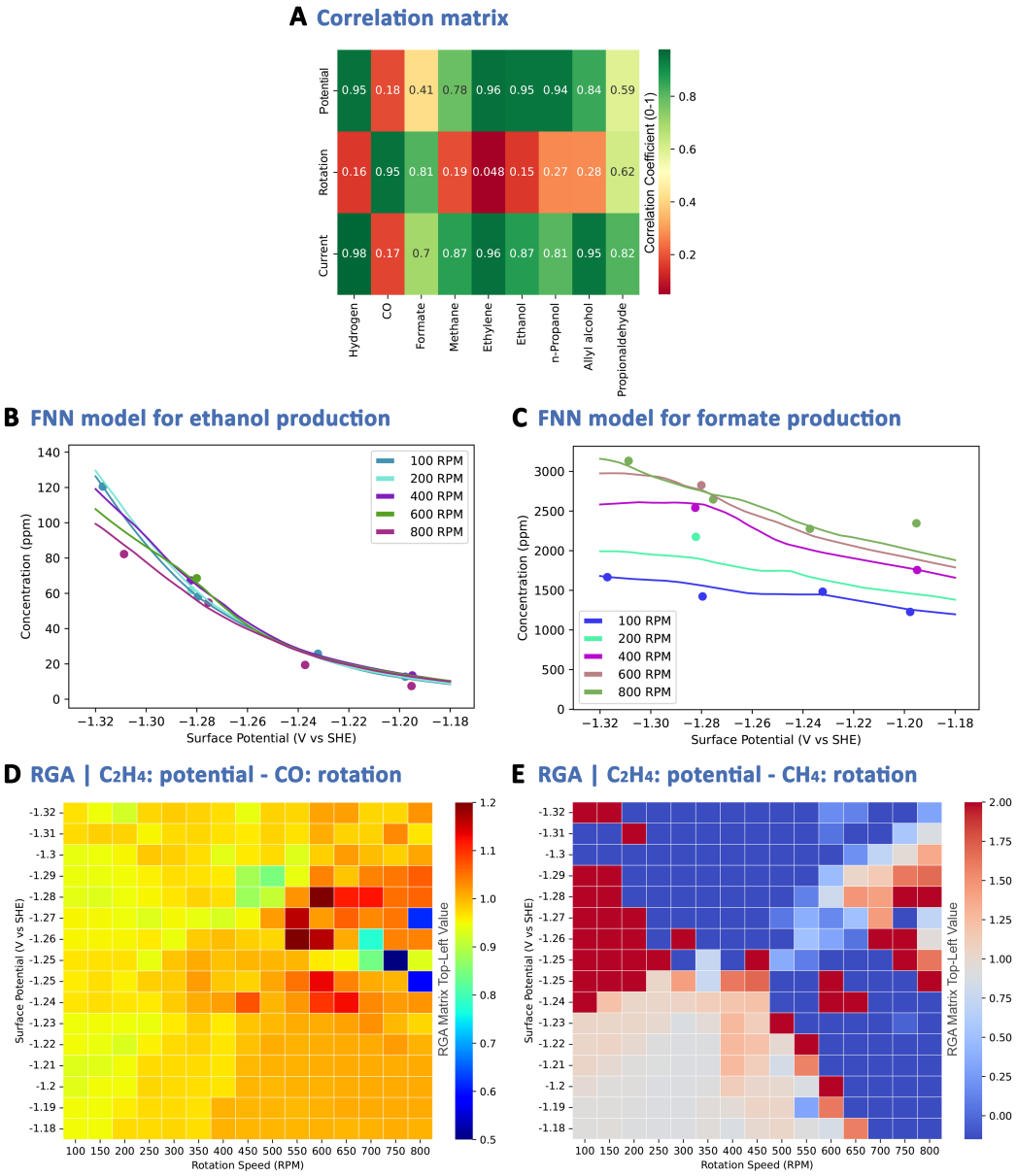

Figure 2.6: Examples of successful applications of ML techniques to CO_2 electrolyzer scale-up. (A) Correlation matrix showing the degree of linear correlation between the production rates of nine CO_2 reduction products and the surface potential, rotation speed, and electric current. (B and C) Expected concentration for ethanol and formate at different operational points. Continuous lines show predictions at different rotation speeds, and solid markers show averaged experimental data. (D and E) Relative gain arrays that demonstrate the coupled values. (D) Shows that coupling production rates of ethylene with potential and carbon monoxide with rotation speed works well for controlling the system with two PI controllers since RGA values are close to 1 across all conditions. However, (E) has varying RGA values at different operational regions, indicating that two PI controllers can control the process only in a small region of the parameter space between -1.18 and -1.23 V vs. SHE and 100 to 500 rpm where RGA values are close to 1. For the remaining operational ranges, an MPC is needed.

term is weighted by the standard deviation of the data point generated by repeating experiments at specific inputs three times. The FNN model is described in more detail by Luo et al [97]. Fig. 2.6 (B) shows the concentration predictions of ethanol, one of the most valuable products in this electrochemical reactor, and Fig. 2.6 (C) shows the formic acid model without an overfit in the operational range described [92]. Additionally, this model can be used for management-level control and optimization. The energy consumption of the reactor is related to the applied potential, so set-points can be selected by solving a nonlinear optimization problem that maximizes the energy efficiency or profitability of the reactor. This approach was demonstrated by selecting cost-optimal set-points to conduct multivariable control experiments [76, 92].

Another step up in complexity is the use of recurrent neural network (RNN) models. RNNs are a class of deep learning neural networks that are specifically suited for handling a series of data points, such as time-series data. To capture the time dependencies, the RNNs feed the neural network output of the previous states as an additional input to the next unit. This recursive nature of the RNN is usually explained as its *memory* of the previous data in the series. The more advanced RNN structure is the long short-term memory (LSTM) unit [98]. For process data regression, LSTMs check the time-dependent relations between two respective inputs and learn how the process should dynamically develop for the next time steps. Specifically, LSTMs check a specific time window from the past data and learn the inherent relations from this time window.

RCE cell dynamics vary depending on specific operating conditions. For example, the dead time in the RCE cell depends on the specific rotation speed or the amount of change in rotation speed [92]. RNN models were shown to adapt to variable dynamics and are able to capture the dynamic behavior of the RCE well. Alternatively, the transient behavior of product concentrations in the effluent of the RCE cell can be approximated using a continuous stirred tank reactor (CSTR) approximation [76]. However, this type of approximation is not an accurate description of the real reactor and adds error to predictions. Thus, a model built only with electrochemical cell data can represent inherent reactor dynamics better than hybrid model approximations. However, to

build a deep learning model such as RNN, voluminous datasets are required. Although the applied potential, current, and rotation speed values are recorded at per-second basis, the output gas concentrations are measured via GC, which only provides results in long discrete time intervals (e.g., 20 min). To overcome the scarcity of the GC data, the dataset was augmented using polynomial fits to approximate a probable dynamic experimental trajectory between GC data points [92]. After enriching the dataset with the polynomial fits, more than a hundred thousand artificially generated data points were generated from the initial hundreds of GC data points. This increase in the amount of data enables training of a dynamic deep learning model and can be useful in the dynamic modeling of any electrochemical process with gas products. RNNs have been shown to model the dynamic behavior of chemical reactors and to make robust models for use with model predictive control (MPC) or multiple PI controllers, even when faced with data variability [98, 99]. For example, two PI controllers were used for multi-input-multi- output (MIMO) control using feedback from the LSTM models of the RCE [92] and Xavier and Trimboli used MPC in an electrochemical system to charge a lithium-ion battery in the shortest time under voltage constraints using a circuit model [100].

2.7 Benefits of machine learning for scale-up research

A black-box ML model itself can be operationally very useful, yet would not be very informative about the underlying mechanisms. Efforts to discover the first-principle equations of electrochemical CO_2 reduction can be accelerated and supported by black-box steady-state models. A candidate kinetics model can be derived from a proposed reaction mechanism, and this mechanism can be validated by experimental data at various operational regions. However, in complex processes such as CO_2 electrolysis, there are many possible candidate reaction mechanisms, and it would be very costly and time-consuming to experimentally validate each model. Instead, the results of a proposed kinetic model can be compared to the predictions of steady-state ML models at

numerous operational conditions. Thus, a strong generalizer model built with well-distributed data from experiments can produce infinitely many accurate predictions within the operational range and replace a myriad amount of physical experiments.

Additionally, due to the non-linear nature and high degree of complexity in developing electrochemical synthesis processes, new control schemes may be necessary to control these devices effectively when scaled-up. Thus, the development of robust, system-specific models and control techniques alongside the development of the reactor provides an integrated approach to developing both the reactor and the methods of controlling it. The control strategy of a system can be decided based on an RGA. In RGA, one of the process inputs is coupled with one of the process outputs for each input and output. The RGA results for a nanoporous copper cylinder electrode in the RCE are presented in Fig. 2.6. If the RGA results are close to one in a broad range of operation regions, then multiple PI controllers can be implemented for feedback control. On the other hand, if the RGA array consists of a broad range of values including negative numbers and values greater than 1, a more advanced controller scheme such as MPC should be implemented.

The objective of showing successful control in RCE is to develop control strategies and intuition for a scaled-up system. Model-based control may be particularly useful for nonlinear system scale-up efforts, as in the implementation of MPC. If there is a dynamic model available, an MPC scheme can be constructed, and ML methods have been proven to build accurate dynamic models in the absence of first principles. In the context of scale-up, an MPC control system can leverage information from multi-scale models of the reactor and external factors in its control actions. For example, the controller can stabilize the system while simultaneously minimizing the energy consumption, maximizing selectivity of desired products, avoiding unsafe operating regions, etc. Likewise, this multi-scale modeling and optimization approach could allow better integration of complex reactor interactions and be used to guide the optimized design of industrial reactors, as well as implement control for nonlinear electrochemical reactors once constructed.

2.8 Understanding underlying relationships through dimensional analysis

In addition to the black-box-type ML models discussed in the previous section, dimensional analysis is a powerful, reduced-order modeling method for understanding underlying relationships in electrochemical reactors. When used properly, dimensional analysis enables the description of intrinsic relationships between variables in a system using dimensionless numbers: i.e., groups of physical variables that reduce to dimensionless descriptors for specific phenomena. By establishing scale-invariant relationships between physical variables, the same characteristics can be defined for systems of different scales by ensuring that the dimensionless value that describes that characteristic is the same in both systems [101, 102]. Additionally, these dimensionless numbers can provide an effective way of investigating the influences of physical variables on a process by reducing the order of parameters to be studied. For example, changing temperature has multiple effects on the electrochemical CO_2 reduction process including the diffusion coefficients of species, the viscosity and density of electrolytes, the solubility of CO_2 in the bulk electrolyte, the kinetics of homogeneous buffer reactions, and the kinetics of heterogeneous electrochemical reduction reactions on the electrode surface. Among the aforementioned effects, the temperature effect on diffusion with respect to changes in material properties can be segregated using the Schmidt number (Sc). As defined in Table 1, the Schmidt number reduces three parameters (diffusivity, viscosity, and density) down to a single grouped parameter, simplifying the tracking of temperature effects. Since it is a material property, Sc can also normalize the effects of diffusing species and electrolyte media on the overall mass transport characteristics represented using another dimensionless number, the Sherwood number (Sh).

In the RCE reactor, when Sc and Sh are characterized as a function of rotation speed (non-dimensionalized as the Reynolds number, Re) using simple reactions with facile kinetics producing a single product, a universal relation- ship can be extracted from mass transport limited reaction

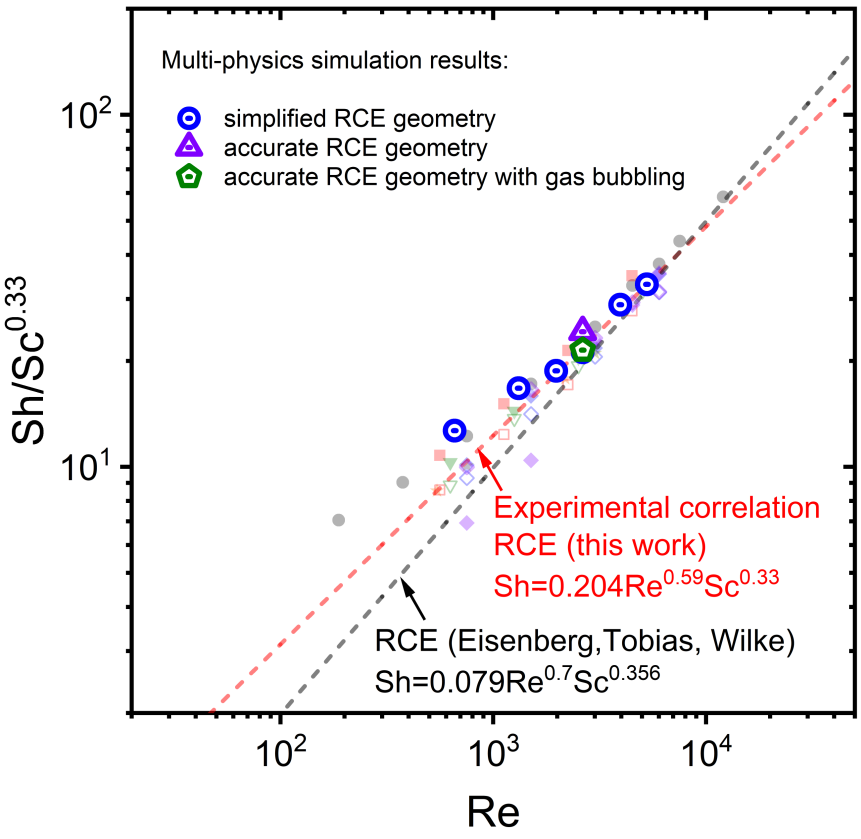

Figure 2.7: The dimensionless universal correlation for mass transport limited reactions in the rotating cylinder electrode (RCE) reactor. The dimensionless correlation between mass transfer and rotation speed for the RCE reactor showing CFD simulation results overlaying experimental data. This correlation applies to any reaction occurring under mass transport limited conditions inside the RCE reactor. Copied with permission [5], Elsevier copyright 2022.

rates (Fig. 2.7) as demonstrated by Jang et al [7] and Richard et al [5]. This dimensionless correlation is useful in three ways. First, once established using facile and simple reactions, convective mass transfer rates of species involved in more complicated reactions can be quantified since all the species are affected by the same hydrodynamics. This is particularly useful in understanding mass transport in CO_2 electrolyzers where mass transport limited reaction rates cannot be readily extracted from experimental data, and homogeneous reactions occur involving multiple buffering species. Second, this relationship can be used to evaluate whether a specific reaction or reaction step is mass transfer limited. If a reaction is mass transfer limited, the rates will align with the universal correlation, while if it is kinetically limited, the rates may be lower and will not scale with Re. Lastly, the correlation between Sh and Re is empirically derived and will only hold for the specific reactor geometry and flow pattern in which it was developed. However, when paired with multi-scale modeling techniques such as computational fluid dynamics (CFD) this correlation can be tied to specific physical phenomena such as the hydrodynamic or diffusion boundary layer thicknesses [5]. Knowing this relationship between Sh and the phenomena governing it can then enable the same correlations developed in the RCE to be applied in systems with different geometry, enabling rational decisions to be made when selecting new reactor configurations.

The Damköhler number (Da) is another dimensionless parameter that has been useful in evaluating the mechanisms driving reaction and selectivity for CO_2 reduction products. Da represents the ratio of timescales for reaction and convective mass transport, and is used to evaluate if a reaction is kinetically or transport limited at given conditions. In the RCE reactor, Da has revealed that CO_2 reduction is not limited by the convective transfer of CO_2 from the bulk to the electrode surface ($Da_{CO_2} < 1$) at -1.41 V vs. SHE for electrode rotation speeds within 100 and 800 rpm. On the other hand, the residence time of CO near the electrode surface, which decreases with Sh^2, has been identified as a critical parameter in determining the selectivity of reactions toward products involving transfer of more than two electrons (>2e-) or toward the intermediate CO. As the Sherwood number decreases, longer residence time of CO leads to higher $Da_{>2e^-}$ and conversion

Name	Description	Symbol and Equation
Reynolds number	$\frac{Inertial\ forces}{Viscous\ forces}$	$Re = \frac{\rho U_{\text{cyl}} d_{\text{cyl}}}{\mu}$
Schmidt number	$\frac{Viscous\ transport}{Diffusive\ transport}$	$Sc = \frac{\mu}{\rho D_{\text{i}}}$
Sherwood number	$\frac{Convective\ transport}{Diffusive\ transport}$	$Sh = \frac{k_{\text{m}}}{D_{\text{i}}/d_{\text{cyl}}} = 0.204 Re^{0.59} Sc^{0.33}$
Damköhler number	$\frac{Reaction\ rate}{Mass\ transfer\ rate}$	$Da = \frac{r_{\text{i}}}{k_{\text{m}} C_{\text{i,b}}}$

Table 2.1: Dimensionless numbers used in research with the RCE reactor to understand the underlying relationships between mass transport and reaction kinetic effects. Here ρ is the electrolyte density, U_{cyl} is the surface velocity of the electrode, d_{cyl} is the cylindrical electrode diameter, μ is the electrolyte viscosity, D_{i} is the diffusivity of species i, r_{i} is the rate of reaction for species i, and $C_{\text{i,b}}$ is the bulk concentration of species i in solution. k_{m} is the mass transfer coefficient derived from the limiting current (j_{lim}) by $j = zFk_{\text{m}}C_{\text{i,b}}$ where z is the number of electrons involved in the reaction, and F is Faraday's constant.

of CO [6, 7]. This relationship between $Da_{>2e^-}$ and Sh has significant implications in the design and scale-up of CO_2 electrolyzers, since the rate of production for >2e$^-$ products can now be estimated by the production rate of the intermediate CO and Sh, representing the local mass transport around the catalyst. Further details on the development of a model capturing this relationship and demonstrating the application of this estimation will be covered in a follow-up report.

In addition to the traditional approach discussed so far, dimensional analysis has the potential to be integrated with the ML approach. There is an analogy between dimensional analysis and ML in the sense that they remove the variance in dimensions to better capture the underlying relationships. Recently, there have been attempts to incorporate or replace the traditional Buckingham Pi theorem using the physics-informed neural network (PINN) to identify independent dimensionless parameters that are significant to the system. PINN could incorporate principles of the Buckingham Pi theorem directly in the training algorithm [103], or replace the theorem by iteratively solving for both the physical dimensional constraints and exponents of the governing equations [104]. This

makes the PINN a powerful tool since the traditional Buckingham Pi theorem does not provide information on the dominance and power-law exponents of each independent dimensionless number [104]. Another approach to implementing dimensional analysis in PINN is through solving physical laws in the form of dimensionless partial differential equations. There are several advantages to non-dimensionalizing equations and unknown variables. Such an approach reduces the computational pressure on neural networks and is less sensitive to simulation instabilities arising from changes in the scales of physical parameters (e.g., diffusivity, mass transfer coefficient, rate constants, etc.) [103, 105].

This chapter has focused primarily on issues related to mass transport. The principles of similarity for mass and heat transfer establish that the level of turbulence experienced by a particle as it traces out similar paths in reactors at multiple scales should be kept constant so that mass and heat transfer rates are similar at all scales. This is key for reactor scale-up. The reader is directed to the chapter on "Principles of similarity and their application for scale up" in "Design of multiphase reactors" [87] for a review of dimensionless analysis in process scale-up from model to prototype scales. When scaling up electrolyzers from a model scale, it will not be sufficient to maintain the similarity of mass and heat. Rather, chemical similarity (rate of product formation to the rate of bulk flow, and rate of product formation to the rate of convective mass/heat transfer) must be maintained. In practice, it is very difficult to maintain chemical similarity between a model and a prototype. These challenges become more significant in electrochemical systems where charge transport between the working and counter electrode also becomes important as this affects concentration polarization and ionic resistance, which in turn affect energy efficiency and heat generation in the cell. The different mass, heat, and charge transport phenomena must be controlled and optimized at each scale during reactor scale-up, and here is where extraction of relationships in a bench-scale system using dimensionless numbers can be powerful, as dimensionless correlations can be useful in determining the similarity principles that are most relevant to the performance of the system. Combined with multi-scale models, dimensional analysis can

be further integrated into the optimal design, control, and operation of pilot scale systems using SM methods. This is very similar to what has been shown in industry. Undoubtedly, heat and charge transport management will likely become more important at larger scales and will need to be optimized to control selectivity and rates for desired products while minimizing overpotential.

2.9 Multi-scale modeling aided research and design

The previous modeling techniques using AI and dimensional analysis are powerful tools for understanding how the process-relevant variables in a system affect its performance, but can be difficult to connect with the underlying phenomena in complex systems. To overcome this difficulty, well-parameterized, physics-based, multi-scale models can be developed to tie these reduced order relationships to physical phenomena and allow the design of optimized larger scale systems. Multi-scale modeling incorporates physics-based modeling techniques to capture local phenomena in detail that cannot be evaluated experimentally. These models can be used to identify the local conditions that correspond to specific experimental results, and then to ensure that the desired local conditions are present in a larger-scale design. By building these multi-scale models based on first principle relationships and ensuring that experimental behavior is replicated, these models can help to generate rational designs that can be tested *in silico* with multi-scale models before construction.

An example of how multi-scale modeling can be used to better understand the local conditions governing reactor performance is in the evaluation of boundary layer conditions at the RCE surface. As mentioned previously, this small region governs the rates at which species move to and from the electrode surface. The universal relationships between Sh and Re discussed in the previous section help us understand the effect of rotation speed on the rate of mass transfer, but only apply to systems where similar definitions of Sh and Re can be used. While we know that the boundary layer is responsible for this behavior, we cannot easily observe this phenomenon during experiments. To probe the boundary layer region, a CFD simulation of the RCE reactor was constructed that

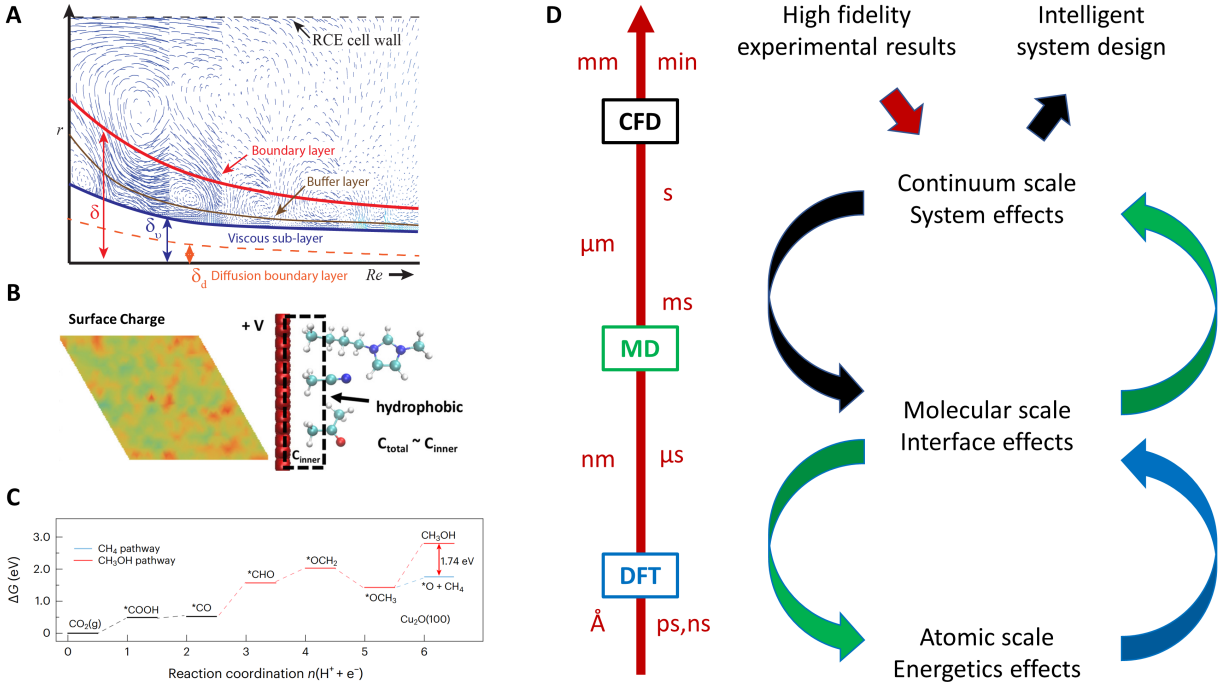

Figure 2.8: Multi-scale modeling can provide insights across the relevant length and timescales to guide intelligent design of advanced electrochemical synthesis reactors. (A) CFD provides information about the system effects, like boundary layer conditions. Reprinted, Copyright 2023, with permission from Elsevier [5]. (B) MD can provide information about the local environment at the electrode interface. Reprinted with permission, Copyright 2020, American Chemical Society [106]. (C) DFT provides information about the energetics of different reaction pathways. Springer Nature, 2022, reproduced with permission from SNCSC [107]. (D) Models can provide information for each other to span various scales and guide intelligent system design.

is capable of replicating the experimental behavior of the cell under well-defined mass transfer limited reaction conditions [5]. This model was developed to capture both the transient and steady-state behavior to ensure that both the average and variations in local conditions could be evaluated. With this simulation, not only can a connection be made between mass transfer rates and the rotation speed, but the physical conditions in the boundary layer region can be defined for the mass transport rates observed. These include the velocity and concentration gradients at the wall, the velocity and concentration boundary layer thicknesses, and the influence of small vortexes near the boundary layer region (Fig. 2.8 (A)). With this information, local conditions in other systems can be identified, and the mass transport rates can be predicted regardless of geometry.

Further efforts are being directed at adding complex reaction schemes involving both heterogeneous and homogeneous reactions to these simulations. These simulations will help to understand how the local concentration and residence time of species in the boundary layer affect selectivity in the multi-step reaction mechanisms of CO_2 electrolysis. Together, this information will enable the extraction of intrinsic reaction kinetics from experimental data, by revealing the local conditions at the electrode surface and removing the bulk characteristics that are influenced by the reactor geometry. Finally, the kinetics and simulation techniques used to describe the existing system can be applied to developing new reactor designs that optimize rates and selectivity for desired products.

In the case of CO_2 electrolysis, mass transport has a significant influence over the product distribution and reaction rates. Once this influence is accounted for, other effects may require further investigation to achieve industry-relevant performance. Molecular dynamics (MD) simulations can provide insight into phenomena occurring at the electrode surface near the electrical double layer, where hydrodynamics are essentially stagnant (Fig. 2.8 (B)) [106]. DFT can provide insight into the energetics of specific reaction pathways on the electrode surface (Fig. 2.8 (C)), guiding the development of more selective catalysts [107].

Typically, modeling methods such as CFD, MD, and DFT are individually investigated, but each can provide complimentary information for each other (Fig. 2.8 (D)) [108]. CFD can provide continuum scale information about the concentrations of species near the electrode surface. MD can incorporate this information to evaluate the local environment within nanometers of the electrode surface to capture stochastic processes relevant to catalysis. DFT provides the energetics of different reaction pathways, but utilizing information from the MD and CFD models can help to determine if a species is available to react on the electrode. Additionally, AI and ML techniques can be incorporated into these modeling methods to reduce the computational cost and increase the accuracy of these models [109]. At larger scales, these techniques can be further integrated into the optimal control and operation of pilot scale systems using SM methods. For example, heat management will likely become more important at larger scales and will need to be optimized

to control selectivity and rates for desired products. Industrial applications for controlling temperature distributions in a steam methane reformer have shown how the integration of advanced sensing, data management, ML, and multi-scale modeling can be utilized to optimize such operations [79]. Likewise, the techniques discussed here could be applied to similar problems in the operation of larger scale electrochemical systems. Only through a coordinated incorporation of these models across multiple scales with high-fidelity experimental data can intelligent designs be developed to bring complex electrochemical conversions to industrial scales.

2.10 Conclusions

Emerging CO_2 electrolyzer technologies have proven to be particularly difficult to scale-up due to the convoluted interactions of mass, charge, and heat transport with complex reaction pathways. Tackling the difficult task of scaling up electrochemical synthesis methods requires a more holistic scientific approach that incorporates high-fidelity experimental results with big data and advanced modeling techniques spanning from the atomic to the reactor scale. In this chapter, we evaluate an approach to accelerate research targeted at the scale-up of complex electrochemical reactors that is inspired by the same techniques used to apply SM in the industry to tackle complex process optimizations. This approach not only provides an improved research methodology but also provides a pathway for the parallel development of strategies to apply SM in industrial electrosynthesis processes.

In summary, this approach is divided into four phases. In Phase I, automation of data collection and handling is applied to the experimental reactor system to accelerate the data collection process and enable easy access to the data when building models. Next, AI and ML techniques along with dimensional analysis are used in Phase II to interpret the large datasets and extract useful relationships governing the reactor performance. For example, RGA provides insights into the dependency of product concentrations on the potential or rotation speed of the electrode, and

dimensional analysis reveals a universal correlation between the rotation speed and mass transport rates. These relationships are used in Phase III to inform the development of physics-based multi-scale models that cover a spectrum of time and length scales relevant to the reaction process. Additionally, these models allow phenomena that cannot be directly observed experimentally to be quantified and tied to the relationships developed in Phase II. The same modeling techniques can be applied in Phase IV to evaluate the performance of scaled-up reactor designs *in silico* before materials are committed to construction. Finally, these four phases can be applied iteratively at each new scale to address additional challenges as they arise.

When applied independently, each of these steps can provide limited insight into how to improve an electrochemical synthesis process. However, when incorporated as part of this holistic approach, the use of these tools can efficiently accelerate the development of industrial-scale electrochemical reactors. To show the utility of this approach, we have provided an example of how it has been applied so far to RD&D of CO_2 electrolyzers. While CO_2 electrolysis has been the focus of this demonstration, the same methodology can be applied to RD&D of any electrosynthesis technology, as the same underlying phenomena will be influential in the scale-up of any electrosynthesis process. Each step of the approach presented in this chapter provides key advantages in accelerating the research necessary to scale up electrochemical systems, and we hope such an approach will be applied by others to accelerate new discoveries in the field of electrochemistry.

Chapter 3

Quantifying transport and electrocatalytic reaction processes in a gastight rotating cylinder electrode reactor via integration of Computational Fluid Dynamics modeling and experiments

3.1 Introduction

Providing energy for a population projected to reach 9 billion people in the middle of this century is one of the most pressing societal issues. Today, fossil fuels comprising coal, oil, and natural gas products account for more than 80% of our global energy consumption [110]. Electrified chemical and fuel manufacturing systems promise to accelerate the renewable energy transition by replacing fossil-sourced molecules with molecules synthesized from air, water, and renewable electricity [111]. The efficient transformation of air and water into high-energy density molecules

in an electrocatalytic reactor, however, requires precise control of the momentum, mass, charge, and heat transport phenomena as well as control of the reaction kinetics at the catalytic sites. Although substantial efforts have been made by the electrochemical engineering community [112] to develop a detailed understanding of the nonlinear transport-reaction relations in electrocatalytic reactors, a more detailed understanding of these processes is needed in order to rationally design and scale-up these technologies to commercially relevant scales.

In order to gain insight into complex electrocatalytic processes, we have recently developed a gastight rotating cylinder electrode (RCE) reactor for the study of electrocatalytic transformations under well-defined transport conditions. Fig. 3.1 (a) shows schematically the different components of the RCE reactor, including the working and counter electrode compartments as well as the inlets and outlets for gases and the ports for sampling loops and auxiliary electrodes. The RCE reactor also includes a heating/cooling element to study the dependence of electrocatalytic transformations on temperature. Fig. 3.1 (b) shows the RCE reactor under operating conditions as well as a digital image of the RCE shaft on which the active catalyst is mounted. The outlet of the gas in the headspace is connected to an online gas chromatogram and the back pressure on the cell is kept at atmospheric pressure unless indicated otherwise.

The RCE geometry has been chosen here as it offers a high degree of symmetry and homogeneity for primary and secondary current distributions on the surface of the electrode [112–114]. This allows the study of electrocatalytic processes under well-characterized electrochemical and hydrodynamic conditions. Although the rotating disk electrode (RDE) has been much more popular for the study of electrocatalysis under well-defined transport, few studies recognize that the primary current distribution in these electrodes is not uniform and that the concentration of species along the radial direction of the disk varies with position. In RDE systems, the potential drop in the solution, the concentration overpotential, and the surface overpotential vary with the radial position on the disk [115], and these gradients become larger for larger disks. This has limited the diameter of RDEs to 5 mm or less, and thus their use has also been limited for the fundamental study of elec-

trocatalytic transformations that require accurate gas and liquid product quantification. Due to the limitations of the RDE system, Newman suggested that perhaps more attention should be devoted to the possibility of using rotating cylinder electrodes rather than rotating disk electrodes [112]. In our previous work, we have shown that the RCE cell is indeed a viable tool for the decoupling of intrinsic kinetics from transport effects and the extraction of high quality data for the development of multi-physics electrocatalytic models, particularly for chemistries involving low solubility gases as reactants and low partial current densities for gas and liquid products [7]. A limitation of the RCE cell in Fig. 3.1(a) is, however, the fact that the counter electrode does not surround entirely the working electrode cylinder, which causes measurable distortions in the primary current distributions around the cylinder. These distortions become more significant under conditions of high current density and low electrolyte ionic conductivity.

The development of a multi-physics model of the RCE reactor will be of value for scale-up efforts if it reproduces with high-fidelity the experimental observations. Furthermore, by cross-validating the multi-physics model against a broad range of chemistries studied in the same cell and under the same hydrodynamic conditions, overparameterization will be reduced, and a deeper understanding of the relationship between transport and reaction processes at multiple time- and length-scales will be gained. Multi-physics models have the unique advantage of accessing multiple levels of spatial and temporal resolution, which cannot be achieved through experimental electrocatalytic or spectroscopic methods. From a fundamental heterogeneous electrocatalysis perspective, these models reveal time constants for processes that are obscured in experimental cells, such as the timescales for surface reaction and diffusion as well as the distribution of timescales for transport of species in and out of the proximity of the electrode. From an engineering and scale-up perspective, a multi-physics model that is correctly parameterized could enable the accelerated *in silico* development of new electrocatalytic processes, where the complex and nonlinear interactions between transport and reactions are unknown to the experimentalist and yet, are captured in simulations carried out across multiple scales [116]. In this first work, we present a systematic approach

and detail the initial process of parameterizing a multi-physics model of the gastight RCE reactor. Through the building of a multi-physics model for the RCE reactor, which has a rather simple and idealized geometry, we generate enough fundamental knowledge and know-how to explicitly list four minimum requirements needed in the development of high-fidelity multi-scale electrocatalytic models. These requirements are:

- The use of enhanced surface treatment functions at the electrode/electrolyte interface to capture accurately the momentum and energy transfer at the time- and length-scales relevant to electrocatalysis.

- The use of a fine mesh with a computational cell size at least one order of magnitude smaller than the characteristic length of the phenomena involved in the transport reaction process. For example, a computational cell size one order of magnitude smaller than the diffusion boundary layer thickness is needed to reveal the effects of cell hydrodynamics in the transport of species in and out of an electrocatalyst surface.

- The use of small simulation time steps to avoid numerical errors, but long simulated process times to capture transient behaviors that can then be validated against time-dependent experimental data.

- Validation of highly detailed simulations against correlations derived experimentally from high quality data that lump parameters relevant to the description of transport and reaction properties in the electrocatalytic cell. For example, the comparison of correlations between the dimensionless Reynolds (Re), Sherwood (Sh), and Schmidt (Sc) numbers obtained from simulations and experiments.

The multi-physics model presented in this work captures both the transport processes at the micrometer and microsecond scale occurring near the electrode/electrolyte interface, as well as the cell hydrodynamics and flow conditions developed in the system over millimeter and minute scales.

The four minimum requirements listed here should inform further attempts to design, simulate, and construct electrocatalytic reactors at increasingly larger scales, and contribute to the accelerated scale-up of electrified chemical and fuel manufacturing systems by closing the existing gap between experimental electrocatalysis in bench-scale reactors and multi-scale models.

3.2 Experimental electrochemical methods in transport phenomena and catalysis

Among the various electrocatalytic transformations of relevance to the renewable energy transition, we have studied in the RCE reactor the electrochemical proton reduction to generate hydrogen (Eq. 3.1), the electrochemical reduction of nitrites to ammonia (Eq. 3.2), and the electrochemical reduction of CO_2 to fuels and chemicals such as liquid alcohols, ethylene, and carbon monoxide. The generation of carbon monoxide (Eq. 3.3) is of particular interest as it is the first step in transforming CO_2 into all other further reduced hydrocarbons and alcohols. An additional reaction studied in the RCE reactor is the one-electron reduction of ferricyanide (Eq. 3.4). This last reaction is used to characterize mass transport properties in electrochemical cells, as the kinetics on the surface of the electrode are fast, the entropy change in the process is small, and the reaction does not involve proton-coupled electron transfer steps that could be affected by changes in the local pH at the electrode/electrolyte interface.

$$2H^{+} + 2e^{-} \rightleftharpoons H_2 \tag{3.1}$$

$$NO_2^{-} + 5H_2O + 6e^{-} \rightleftharpoons NH_3 + 7OH^{-} \tag{3.2}$$

$$CO_2 + H_2O + 2e^{-} \rightleftharpoons CO + 2OH^{-} \tag{3.3}$$

$$[Fe(CN)_6]^{3-} + e^{-} \rightleftharpoons [Fe(CN)_6]^{4-} \tag{3.4}$$

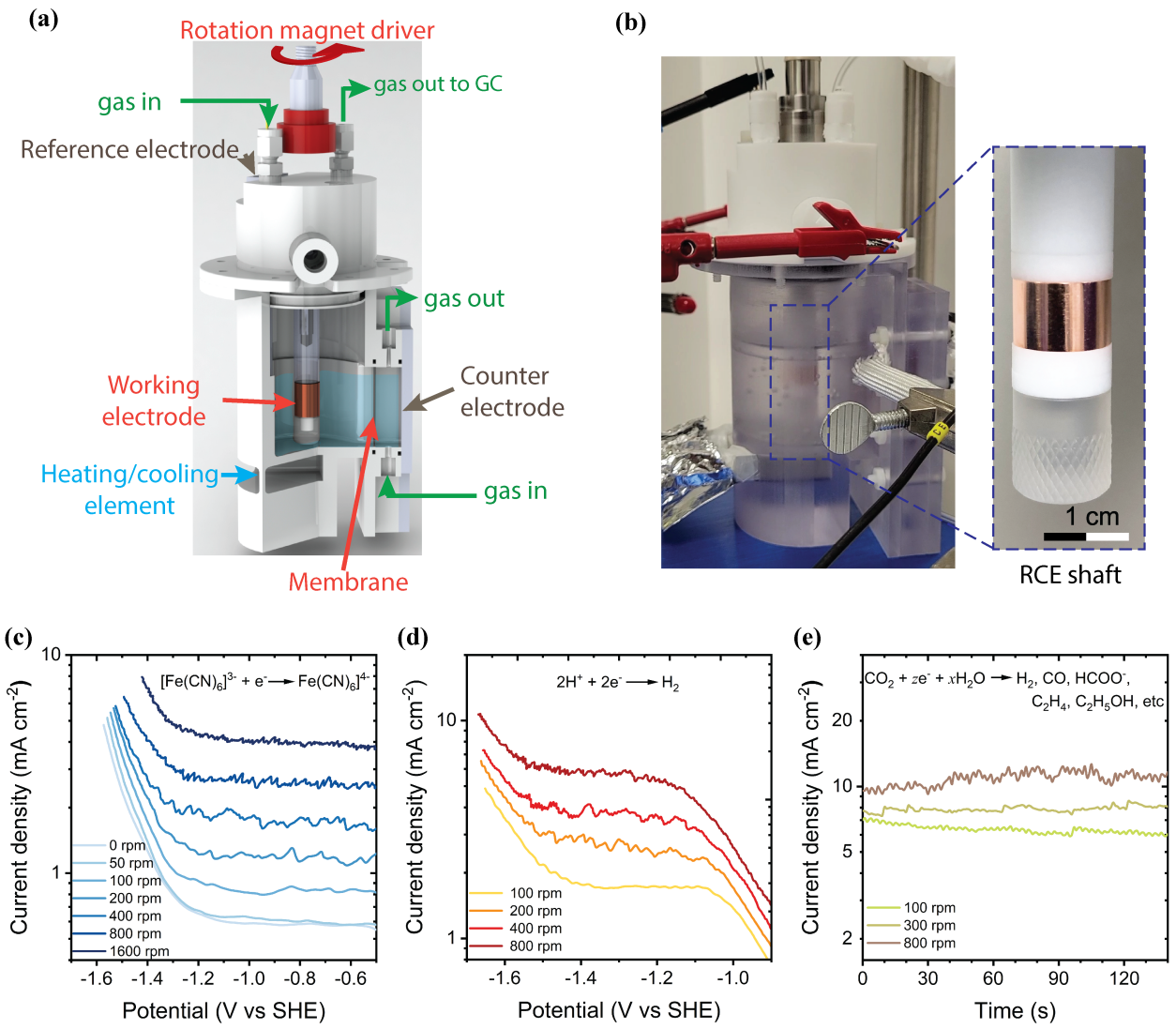

Figure 3.1: (a) Schematic of the RCE reactor showing the separation between the working and counter electrode compartment. (b) Digital image of the RCE reactor under operation. The inset shows the insulating RCE shaft with an electropolished copper cylinder as working electrode. (c) Current density vs. potential curves for the electrochemical reduction of ferricyanide on an electropolished copper cylinder electrode under different electrode rotation speeds. A 0.1 M potassium perchlorate solution with the addition of 0.01 M potassium ferricyanide was used as electrolyte for ferricyanide reduction experiments at a scan rate of 50 mV s^{-1} at 20°C . (d) Current density vs. potential curves for the electrochemical reduction of protons on a mechanically polished titanium cylinder electrode under different electrode rotation speeds at a scan rate of 50 mV s^{-1} at 20°C. The electrolyte is a 0.05 M potassium perchlorate solution adjusted to a pH of 2.5 using perchloric acid. (e) Current vs. time curves for the electrochemical reduction of CO_2 on a nanoporous polycrystalline copper cylinder electrode in a 0.2 M $KHCO_3$ electrolyte at different rotation speeds. The applied potential is -1.28 V vs SHE. Detailed experimental methods for electrode preparations are reported in [7].

$$2H_2O + 2e^- \rightleftharpoons H_2 + 2OH^- \tag{3.5}$$

Examples of experimental potential vs. current curves obtained for the reduction of ferricyanide and protons at 20 °C are shown in Fig. 3.1 (c) and Fig. 3.1 (d), respectively. At potentials positive of -1.4 V vs. the Standard Hydrogen Electrode (SHE), the current density for these two reactions is limited by mass transport, and increases as the rotation speed of the electrode increases. At potentials negative of -1.4 V vs. SHE, the competing hydrogen evolution reaction from water (Eq. 3.5) takes place, resulting in a current density dependence on the applied potential, which is not observed for the reactions limited only by external mass transport at more positive potentials. Fig. 3.1 (e) shows the current vs. time curves obtained during the electrochemical reduction of CO_2 to fuels and chemicals on a nanoporous polycrystalline copper electrode. In comparison to the ferricyanide and proton reduction in Fig. 3.1 (c) and Fig. 3.1 (d), the average current density for the electrochemical reduction of CO_2 shows a smaller dependence on the rotation speed when changing the rotation of the electrode from 100 to 800 rpm. In this case, the currents observed are the result of the complex coupling of transport and intrinsic surface reactions for multiple products, which cannot be readily separated.

Under mass transport limited conditions, the kinetics at the surface of the electrode are faster than the transport of reactants from the bulk of the electrolyte to the surface of the electrode. This results in transport-limited current densities j_{lim} independent of the applied potential. Under these conditions, the current densities are proportional to the bulk concentration of the reactant $C_{\text{i,b}}$, the number of electrons transferred per reacting molecule z, and the mass transport coefficient k_{m} (Eq. 3.6). Here, the limiting current is i_{lim}, F is Faraday's constant, and the geometric area of the electrode is A.

$$j_{\text{lim}} = \frac{i_{\text{lim}}}{A} = zFk_{\text{m}}C_{\text{i,b}} \tag{3.6}$$

In the RCE reactor, we have experimentally measured the transport-limited current densities for the reactions in Eqs. 3.1 through 3.4 under different rotation speeds, reactant bulk concentrations,

and temperatures. The details of these experiments have been previously discussed [7].

The transport-limited current densities provide a wealth of information on the transport phenomena occurring not only in the hydrodynamic boundary layer, but also within the first few electrolyte layers at the electrode/electrolyte interface through the small oscillations in the current density that occur as a function of time [117, 118]. For example, the frequency and amplitude of the current oscillations are similar for the electrochemical reduction of ferricyanide and protons (Fig. 3.1 (c) and Fig. 3.1 (d)) indicating that these oscillations are related only to the transport phenomena and independent of the nature of the reactant molecules or the catalyst surface composition. As the rotation speed of the electrode increases from static conditions (with only gas bubbling in the bulk of the cell) up to rotation speeds of 400 rpm, the amplitude, and frequency of the current oscillations around an average value increase. When the rotation speed is higher than 400 rpm, the frequency of the current oscillations continues to increase while the amplitude of the current oscillations decreases. These changes in frequency and amplitude of the current density oscillations are the fingerprints of the different modes and timescales of mass, heat, and momentum transfer at the electrode/electrolyte interface and are an important component in the process of describing how transport influences selectivity and conversion in electrocatalysis.

Accurate simulation of a complex and yet industrially relevant reaction such as CO_2 electrochemical reduction requires the correct parameterization of numerous interaction: such as heterogeneous reaction kinetics, homogeneous reaction kinetics, mass transfer between gas and liquid phases, as well as heat generation and transfer. This must also be done under non-ideal conditions with local changes in species concentration, and changes in applied surface potential when current distributions are not uniform. This requires a multiscale understanding of these interactions that is aided by the use of multiphysics models at multiple scales. This can be accomplished by separating a multi-scale, multi-physics model into three parts: 1) a CFD component that captures the continuum behaviour of the reactor and transport phenomena at the macroscale (times scales of ms to minutes), 2) a molecular dynamics (MD) component that captures the interplay among

the chemical events occurring at the mesoscale such as absorption and desorption processes at the electrode/electrolyte interface as well as buffer reaction kinetics and proton discharge events (μs to ms), and 3) an *ab initio* component that captures the energetics of making and breaking chemical bonds at the atomic scale for rare events that ultimately result in chemical or electrochemical step turnover (ns and ps). This work deals with the development of the CFD component.

The simulation of the CO_2 reduction process and other electrocatalytic transformations of similar complexity are beyond our current capabilities. The electrocatalytic reduction of protons and ferricyanide is a far simpler process than the electrocatalytic reduction of CO_2 to fuels and chemicals, and yet, it captures the same modes and timescales for transport phenomena occurring at the macroscale during the transformation of CO_2. For this reason, the ferricyanide reduction has been taken here as a starting point for the construction of complex multi-scale electrocatalytic models that can capture transport-reaction processes occurring in proximity to the electrode/electrolyte interface.

3.3 Emergence of universal transport-reaction correlations in RCE electrochemical cell

The rationale for the use of the simple ferricyanide reduction reaction as a starting point for the construction of the multi-physics model comes from the experimental observation of a universal correlation for transport and reaction processes in the RCE reactor, which is independent of the nature of the reacting molecule. We have experimentally observed that any molecule being reacted or generated on the surface of the rotating cylinder electrode will have to travel across the same fluid layers making up the turbulent flow conditions around the surface of the electrode [7]. From the transport-limited current densities shown in Fig. 3.1, mass transfer coefficients were calculated according to Eq. 3.6. Fig. 3.2 (a) summarizes the experimentally measured mass transfer coefficients for solutions with high Sc above 100. High Sc indicates that the diffusion boundary layer

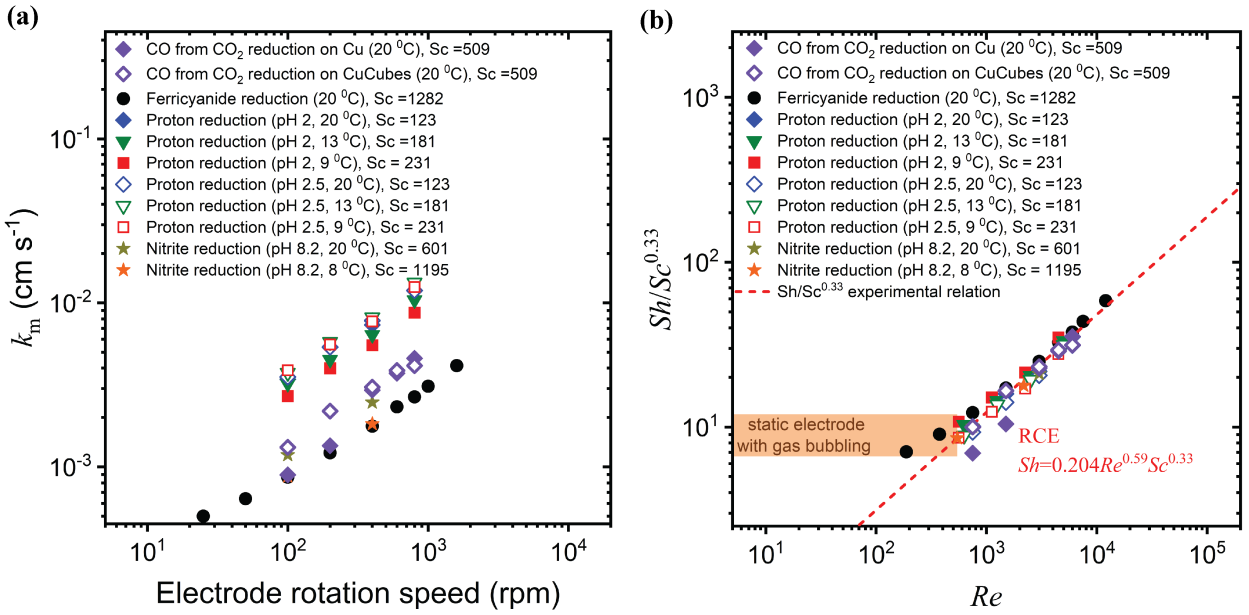

Figure 3.2: (a) Experimental mass transfer coefficients determined under different electrode rotation speeds in the RCE cell. (b) Experimentally determined dimensionless relation between mass transfer and cell hydrodynamics for mass transfer coefficients in (a).

(δ_d) will be small and shorter than the viscous sub-layer (δ_v). The mass transfer coefficients range from 0.0005 cm s^{-1} for the reduction of ferricyanide at electrode rotation speeds of 25 revolutions per minute (rpm), up to 0.01 cm s^{-1} for the reduction of protons at electrode rotation speeds of 800 rpm. Higher temperatures and higher rotation speeds result in higher mass transfer coefficients and thus, higher flux of reactants to the surface of the electrode.

Universal relations for different electrocatalytic transformations tested in the same electrochemical cell can be developed through the use of dimensionless numbers. In the RCE reactor, the experimentally obtained mass transfer coefficient can be transformed into its dimensionless mass transfer coefficient counterpart, Sh number, and can then be plotted against dimensionless descriptors of the hydrodynamics and intrinsic properties of the fluid, such as Re and Sc numbers. When this task is accomplished, a universal correlation emerges between the Sh, Sc, and Re numbers that is governed by the hydrodynamics of the fluid around the surface of the rotating cylinder electrode, and is independent of the nature of the molecules being transported in or out of the surface

of the electrode. The experimental correlation for dimensionless mass transport and momentum transfer is shown in Fig. 3.2 (b) for our RCE reactor. This correlation along with definitions for Re and Sc used in this study are also expressed in Eqs. 3.7, 3.8, and 3.9. Eq. 3.7 is of the same form as other experimental correlations that relate the limiting current densities to a power of the cylinder surface velocity.

$$Sh_{\text{RCE}} = \frac{k_{\text{m}}}{D_i/d_{\text{cyl}}} = 0.204 {Re_{\text{RCE}}}^{0.59} Sc^{0.33} \tag{3.7}$$

$$Re = \frac{\rho U_{cyl} d_{cyl}}{\mu} \tag{3.8}$$

$$Sc = \frac{\mu}{\rho D_i} \tag{3.9}$$

Here the coefficient of 0.204 is a function of the cell geometry while the exponents on Re and Sc are a function of the hydrodynamics governing mass transfer to and from the electrode surface. ρ and μ are the bulk density and viscosity of the fluid, respectively, U_{cyl} and d_{cyl} are surface velocity and diameter of the rotating cylinder electrode, respectively, and D_i is the diffusivity of the reactant or product i. Similar correlations have been developed by [119] and others [120, 121] where an exponent of 0.50 to 0.70 for the Reynolds number has been suggested for smooth cylinders. Our experimental results indicate an exponent of 0.59. Differences in the exponent values are due to differences in convective transport across experimental cells of varying geometries, as discussed later in this work. The dependency of Sh as a power of nearly $2/3$ with respect to Re and $1/3$ with respect to Sc indicate that the penetration of eddies into the laminar sublayer play an important role in the mechanism of the mass transfer in the RCE for $Re > 500$ in the turbulent regime [122].

Fluid layers around the RCE are schematically shown in Fig. 3.3 (a) and have been discussed in detail in the turbulent fluid dynamics literature. Mass transfer near the surface of the RCE is best understood through the description of the three distinct layers that form the hydrodynamic boundary layer (δ). Namely, the viscous sublayer δ_v, buffer layer, and turbulent logarithmic layer

each with a uniquely predominant mode of mass transfer [123]. Near the surface of the electrode, the electrolyte in contact with the surface is in a non-slip condition and results in a quasi-static laminar sublayer or viscous sublayer where the predominant mode of mass transfer is diffusion. Beyond the viscous sublayer is the buffer or generation layer where both viscous shear stress generated at the electrode surface as well as the turbulent shear stress from the outer layer are too important to be ignored. Exceedingly energetic small-scale turbulence is generated here by the instability of the strongly sheared flow as a means to transform mean-flow kinetic energy to turbulent kinetic energy. Some of the turbulence generated here is carried outward into the broad outer layer of flow, and some is carried inward into the viscous sublayer. Finally, the fully turbulent logarithmic layer of the boundary layer is characterized by a mean fluid velocity that follows a logarithmic profile with the distance from the wall. Outside the boundary layer is the bulk flow region that contains most of the fluid and where convection is the predominant mode of mass transfer.

In our previous work in the electrocatalytic reduction of CO_2 on an electropolished polycrystalline copper cylinder electrode, we have found that the residence time of CO near the surface of the electrode determines the degree of CO conversion to further reduced products such as methane, ethylene, ethanol, and propanol [7]. At a fixed surface applied potential, higher electrode rotation speeds, which correspond to higher Sh numbers, favor the production of the CO intermediate rather than the more reduced ethylene, methane, and alcohol products. The change in selectivity as a function of the Sherwood number was rationalized through the approximation of the electrode/electrolyte interface as a continuously-stirred tank reactor (CSTR; i.e., a control volume with inflow and outflow of reactants, intermediates, and products that is internally well-mixed) as schematically shown in Fig. 3.3 (b). By creating a parallel between the different layers that build the turbulent boundary layer and the effects that we observe experimentally, we aimed to describe the rationale behind changes in selectivity as a function of the hydrodynamics in the cell. Faster electrode rotation speeds which result in higher Sherwood numbers result in increased rates of hy-

drogen and formate production, while the rate of CO_2 reduction to CO remains unchanged (Fig. 3.3 (c)). Improved mass transport results in increased bicarbonate concentration and the lowering of the pH at the electrode surface, which should reduce proton concentration overpotentials relevant to the production of hydrogen and formate. On the other hand, the transformation of CO_2 to CO appears to be limited by CO_2 adsorption [124] and is not affected by changes in the concentration of protons which become more available at higher Sh numbers. In the case of CO_2 reduction, the rates of adsorption/electrosorption, as well as desorption are important and need more consideration. It becomes evident from the experimental data in Fig. 3.3 (c) and 3.3 (d) that the steady-state surface coverages of CO and hydrogen on the surface of the electrode are not enough to build micro-kinetic models for CO_2 reduction as these do not account for the residence time of intermediates in the proximity of the surface and the probability of collisions between surface-bound molecules and reactants traveling towards and away from the surface of the catalyst. That is, surface collision rates and the residence time distribution for reaction intermediates in the proximity of the electrode are determined by stochastic processes that can be only captured by molecular dynamic simulations and not by deterministic Fickian diffusion models frequently used in the simulation of CO_2 reduction processes.

The introduction of the concept of the residence time of reaction intermediates in multi-electron transformations is a complex idea to express in mathematical terms. There exists a residence time distribution for species in the proximity of the electrode and the average time that a reaction intermediate is available for further reaction, which will be a function of the diffusion, convection, and migration elements of the transport equations as well as the geometry of the cell. We have previously characterized the relative timescales for competitive transport and reaction processes utilizing experimentally determined Damköhler numbers. Damköhler numbers offer an experimental window into the relative timescales for these processes, but do not offer insight on the absolute timescales relevant to transport and reaction steps. Determining the absolute dimensions and timescales for reaction and transport components relevant to electrocatalysis is only possible

through accurate multi-scale and multi-physics modeling.

However, before building complex multi-scale models, it is imperative to define a hierarchy of modeling techniques and to determine the relevant spatial and temporal resolutions at which each can provide insight (Fig. 3.3 (b)). Typically, the computational cost of simulations increases as the physical scale of the interactions being modeled decreases, thus the timescales associated with these simulations are restricted. Efficient use of resources requires a top-down approach to be taken, where simulations of aggregate interactions occurring in the micrometer or greater scale (as with CFD) are performed first. This is particularly important for complex reactions such as the reduction of CO_2 where transport at the macroscale controls selectivity. Then, once these simulations are able to accurately capture the behavior of the system at the macroscale, more computationally expensive techniques such as MD or DFT, which investigate interactions on the nm and pm scale, can be integrated. Effectively integrating these modeling techniques together requires the delineation of the scales associated with the interactions being modeled, and coordination of the information that is passed between the models as boundary conditions at these scales. In such a manner, multi-scale modeling can be used for the development of accurate theories of electrocatalysis from first-principle quantum mechanics in regimes where reactions are not purely limited by mass transport and interactions are too complex to be evaluated by traditional techniques [108].

Numerous theoretical and computational works have been dedicated to the description of the transport processes in the rotating cylinder electrode reactor. CFD models developed so far, however, do not capture momentum and mass transfer between the solid and the liquid interface with the detail necessary to build high-fidelity multiphysics models of electrocatalytic transformations. That is, the determination of the concentration polarization and gradients in concentration emerging at the nanoscale near the surface of the electrode have not been calculated in multi-physics models.

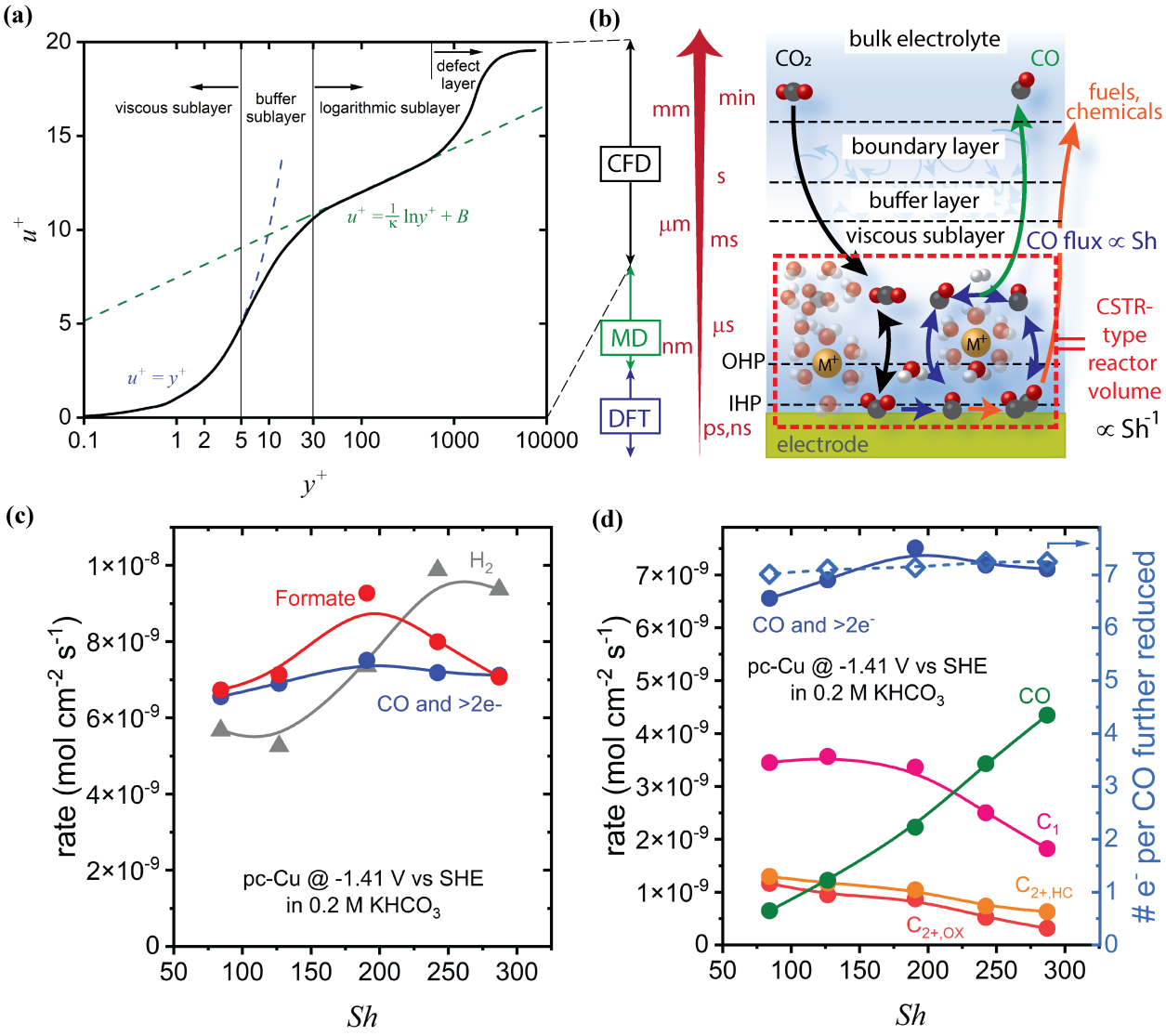

Figure 3.3: (a) Normalized mean velocity profile in a turbulent boundary layer in semi-log coordinates. Illustrated are the various layers that make up the boundary layer. Here the Von Karman constant κ is 0.41 and B is 5 for turbulent flow over a smooth wall. (b) Schematic representation of a CSTR-type reactor volume at the electrode-electrolyte interface where CO production, desorption, re-absorption, diffusion, and further reduction take place. Transport and reactions steps occur at similar timescales within a narrow region inside the viscous sublayer. CO further reduction rates and product selectivity are affected by the mass transport within the cell as described by the Sh number. (c) Changes in the experimentally measured rates for CO_2 reduction in a 0.2 M $KHCO_2$ electrolyte at -1.41 V vs. SHE under different Sh number. (d) Changes in the conversion of the CO intermediate and the selectivity of further CO reduction products as function of the Sh number.

3.4 Formulation of numerical simulation

Simulating fluid behavior is a balance between capturing pertinent details and optimizing the utilization of computational resources. Often times, due to computational resource limitations, relatively coarse meshes and universal velocity functions are used to reduce the computational resources required to run simulations in a reasonable time. These simulations are typically performed using a steady-state solver method, and lack a comparison to transient data. While this approach may be suitable for evaluating the bulk behavior in a reactor, an investigation of the intrinsic fluid behavior and its impact on electrocatalysis requires a more detailed approach that can describe the transient behavior of the reactor, especially near the electrode surface. For example, [125] simulated multi-ion transport in dilute electrolytic solutions around a rotating cylinder electrode and observed fluctuations in all physical fields (electric potential, concentration, and flow fields) occurring near the electrode surfaces. Fluctuation in all physical fields also result in temporal and spatial fluctuations in the boundary mass fluxes and thus, the local current densities and the total measured currents. The fluctuations in current densities and their relation to local mass transfer rates were first described by [126] for turbulent flow in a pipe wall and then by [127] for ferricyanide reduction on a rotating cylinder electrode. It is well understood that the small eddies in the region of the viscous sublayer of a turbulent flow, play an important role in determining the transfer rates to the wall, especially in the case of high Sc. Since the flow of these small eddies is unsteady, the local mass transfer rates to the wall are fluctuating [122]. A complete discussion of early methods utilized for the study of diffusion-controlled electrochemical reactions and their applications in the study of transport phenomena was reported by [117] and [118]. For a model to truly capture the fluid behavior in an RCE, it is necessary to capture the mechanisms causing the fluctuations in current density, as observed experimentally in Fig. 3.1. To do this, careful consideration must be made in developing a method capable of resolving the fluid behavior extensively to the surface of the electrode.

The following sections will discuss the details of our final simulation methods, where multiple iterations of mesh and solution method were tested to determine an accurate approach for simulating the hydrodynamics of the RCE. Understanding why the methods described here were chosen is just as important as understanding why other methods were not. Thus, alongside a detailed explanation of the methods, specific examples are provided to explain why these methods were selected.

3.4.1 Geometry simplification

Experimental data (Fig. 3.3 (c) and Fig. 3.3 (d)) and boundary layer theory (Fig. 3.3 (a)) suggest that the most important hydrodynamic effects in the RCE occur near the electrode surface for mass transport affected reactions. This location is where the diffusion boundary layer is formed that governs the rate at which species can move to and from the catalytic surface inside the viscous sub-layer. In the bulk, turbulent mixing that occurs even at relatively low rpm should ensure a well-mixed solution, and at a first approximation, can be assumed to have little effect on transport at the electrode surface. With this in mind, the geometry of the reactor was simplified to reduce computational cost while maintaining the features necessary to accurately model the reactor behavior.

The geometry of the working electrode compartment in the RCE reactor is not entirely cylindrical, as it has an expanded section in the direction of the counter electrode to accommodate the ionic membrane and counter electrode compartment (Fig. 3.4 (a)). The height and diameter of the fluid phase was maintained in the simulation geometry and was modeled into a symmetric cylindrical geometry shown in Fig. 3.4 (b). The reference electrode and gas sparger are tubes of 4 and 3 mm diameter, respectively, located in the bulk region of the fluid (Fig. 3.4 (a)). Because these tubes are located near the outer wall (more than 1.5 cm from the rotating cylinder surface), they are considered to have a minor role in determining the transport properties relevant to electrocatalysis at the rotation speeds of interest and were removed in the simplified geometry as illustrated in Fig. 3.4 (b). All dimensions of the rotating cylinder electrode shaft were maintained consistently with the

actual RCE reactor. This includes a cylinder diameter of 1.2 cm, an electrode length of 0.8 cm, and location of the electrode and shaft consistent with the RCE reactor. All relevant dimensions are provided in Fig. 3.4 (b). Simulations at rotation speeds between 100 and 800 rpm were performed with this simplified geometry. To verify that the features removed for the simplified geometry do not have a significant impact on the hydrodynamics relevant to electrocatalysis in the RCE, a simulation geometry exactly matching that of the real RCE reactor, including all the features removed in the simplified geometry, was also tested. This reactor accurate geometry was extracted from the CAD file used in the construction of the actual gastight RCE reactor. This accurate geometry was also tested with gas bubbling to verify the insignificance of bubbling on the reaction conditions in the accurate geometry. For simplicity the simplified reactor geometry used for the bulk of the simulations in this study will be referred to as the *simplified geometry* while the geometry used to verify the performance of the simplified geometry will be referred to as the *accurate geometry*.

3.4.2 Mesh generation

A non-uniform mesh with polyhedral mesh type was used in the majority of the geometry volume. Polyhedral mesh creates cells with more faces than other mesh types, and because of this connection with a large number of adjacent cells, is best suited to simulate swirling or mixing flows like those created in turbulent mixing found in the RCE. Finer mesh was used in regions near boundaries and interfaces while coarser mesh was used in regions where gradients in velocity and concentration are expected to be minimal as shown in Fig. 3.4 (c). A structured mesh was used to help capture the boundary layer region near the shaft surface where fluid motion is expected to be primarily in the azimuthal direction. This boundary layer mesh was made of 20 layers with a growth rate of 1.25 and an initial cell height of 3 μm, resulting in a total thickness of 1029 μm. A closeup of the boundary layer mesh with dimensions is provided in Fig. 3.4 (d). These dimensions were chosen after testing other configurations to enable good resolution of the diffusion boundary layer and viscous sublayer to enable accurate simulation of both momentum and mass transfer at

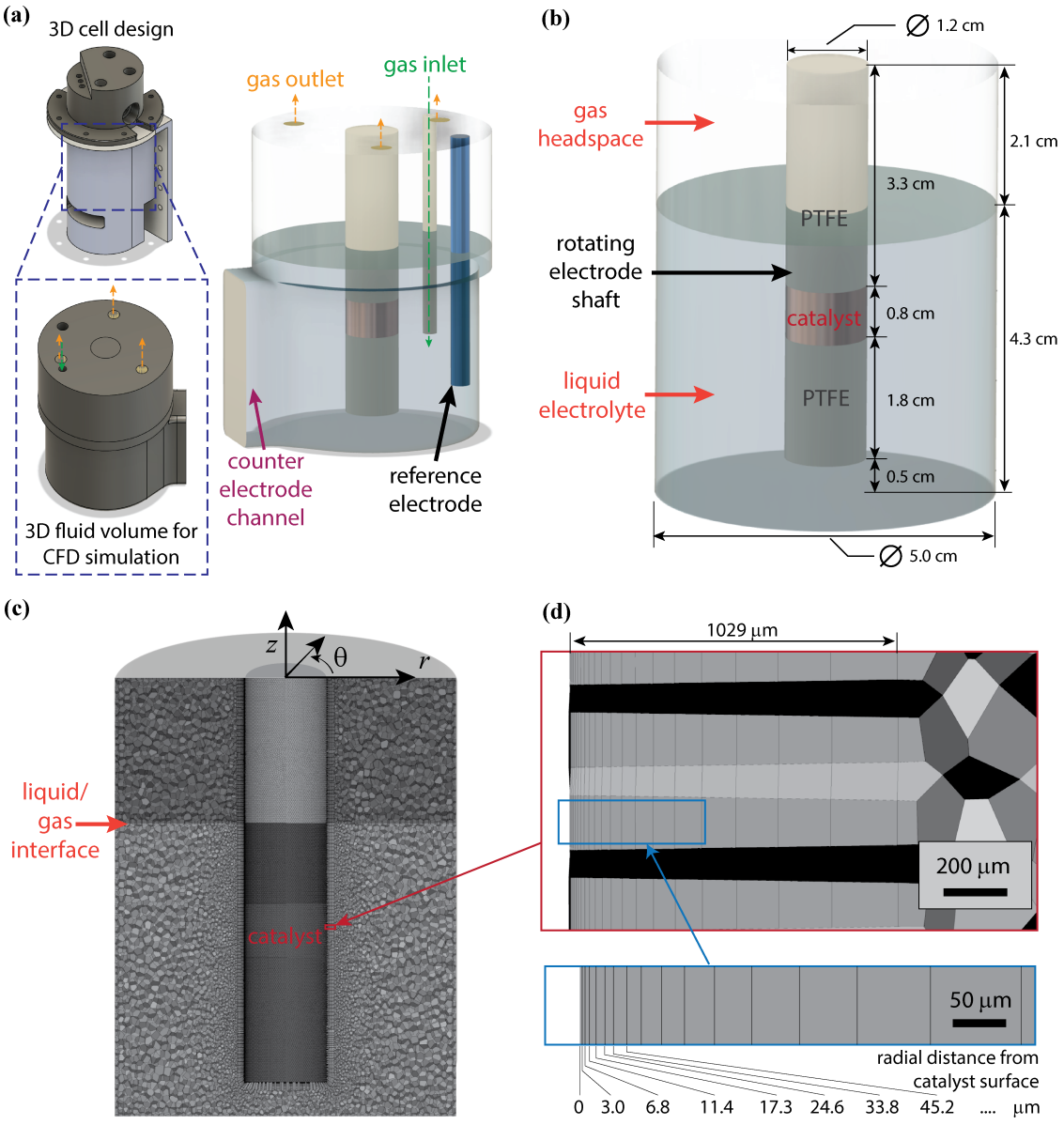

Figure 3.4: 3D geometries used for CFD simulations.
(a) Accurate geometry extracted from gastight RCE Computer Aided Design (CAD) files. (b) Simplified geometry used for simulations. The simplified geometry in (b) does not include the counter electrode channel, reference electrode, gas inlet tube, and bubbling of gas through the inlet which are present in the experimental RCE reactor. Simulation data was primarily collected using the simplified geometry in (b) which results in computation time savings. The accurate geometry in (a) was used to verify that the assumptions made for the simplified geometry do not affect the electrocatalysis simulation results. (c) Cross section of the final polyhedral volumetric mesh used in this study for the simplified geometry. Cylindrical coordinates used in description of the reactor are shown for reference with components u_θ, u_r, and u_z in the respective azimuthal, radial and axial directions (d) Closeup of the structured boundary layer mesh at the surface of the shaft with the corresponding radial positions relative to the electrode.

the shaft surface.

The final mesh resulted in a total of 859,897 cells. Quality measures including the orthogonal quality and squish were both within acceptable ranges, with a minimum orthogonal quality of 0.15 and a maximum squish of 0.85 [128]. Average values for orthogonal quality and squish show much better quality for the majority of the cell, with an orthogonal quality having an average of 0.98, and squish having an average value of 0.023. All lower quality cells reside at the surface near the corner created at the bottom of the shaft due to the sharp curvatures of the geometry. Since these cells have little impact on the overall hydrodynamics, these values were considered adequate. Additionally, the aspect ratio has a maximum value of 356.77 and an average value of 21.45. While the maximum value is outside of the specifications by [128], these cells with high aspect ratio are all located in the boundary layer mesh where fluid flow is known to be almost entirely parallel to the shaft. Because of this, the high aspect ratio in this region should not affect the results of the simulation and allows for a reduction in the cell count and time to run simulations. Overall, the mesh quality of the multi-physics model is classified as *excellent*, the highest level based on specifications outlined in the Ansys Manual, which ensures the convergence of simulations and the accuracy of the numerical solutions [128].

3.4.3 Fluid flow

All simulations were performed with Ansys Fluent simulation software using a finite volume method. A pressure-based, solution method was used along with the multiphase, volume of fluids, and full multicomponent diffusion models. Incompressible fluids under turbulent flow are described by the Reynolds averaged Navier-Stokes (RANS) equation (Eq. 3.10) and the continuity equation (Eq. 3.11).

$$\rho\left(\frac{du}{dt} + u \cdot \nabla u\right) = -\nabla P + \nabla \cdot \left((\mu + \mu_{\mathrm{T}})\left(\nabla u + (\nabla u)^{\mathrm{T}}\right)\right) \tag{3.10}$$

$$\nabla \cdot (\rho u) = 0 \tag{3.11}$$

Here, u is the averaged velocity vector in cylindrical coordinates with components u_θ, u_r, and u_z in the respective azimuthal, radial, and axial directions. ρ is the density, P is the pressure, μ is the fluid viscosity, and μ_{T} is the turbulent viscosity.

The realizable $\kappa - \epsilon$ turbulence model was used to describe the turbulent fluid region where the turbulent viscosity μ_{T} is provided by Eq. 3.12.

$$\mu_{\mathrm{T}} = \rho C_\mu \frac{k^2}{\epsilon} \tag{3.12}$$

in this equation κ is the turbulent kinetic energy, ϵ is the turbulent energy dissipation rate, and C_μ is a turbulence model variable calculated from realizable $\kappa - \epsilon$ theory. Both RANS [129] and realizable $\kappa - \epsilon$ theory [130] have been discussed in detail elsewhere.

To resolve the fluid behavior near the rotating surface, an enhanced surface treatment method was used. This method employs the turbulent viscosity described by Eq. 3.12 in the turbulent logarithmic region and the one equation model of Wolfshtein [131] in the viscous sublayer where μ_T is defined by Eq. 3.13.

$$\mu_{\mathrm{T,lam}} = \rho C_\mu l_\mu \sqrt{\kappa} \tag{3.13}$$

l_μ is a length scale factor calculated using Eq. 3.14 [132].

$$l_\mu = y C_l^* \left(1 - e^{-Re_y/A_\mu}\right) \tag{3.14}$$

where y is the normal distance from the wall, Re_y is the turbulent Reynolds number, A_μ is a constant equal to 70, and $C_l^* = \kappa C_\mu^{-3/4}$ with $\kappa = 0.41$. Turbulent viscosities in this two-layer approach are blended using Eq. 3.15 [133].

$$\mu_{\mathrm{T,enhanced}} = \lambda_\epsilon \mu_T + (1 - \lambda_\epsilon)\, \mu_{\mathrm{T,lam}} \tag{3.15}$$

Here λ_ϵ is a blending function that is dependent on Re_y.

For the momentum balance, the dimensionless velocity is defined separately for the laminar (Eq. 3.16) and turbulent (Eq. 3.17) region near the wall [134, 135]

$$u^+_{lam} = y^+ \left(1 + \frac{\alpha}{2} y^+\right) \tag{3.16}$$

$$\frac{du^+_{turb}}{dy^+} = \frac{1}{\kappa y^+} \left[S' \left(1 - \beta u^+ - \gamma \left(u^+\right)^2\right)\right]^{1/2} \tag{3.17}$$

where,

$$S' = \begin{Bmatrix} 1 + \alpha y^+ & for\ y^+ < y^+_s \\ 1 + \alpha y^+_s & for\ y^+ \geq y^+_s \end{Bmatrix} \tag{3.18}$$

Here, the superscript $^+$ indicates a nondimensionalization by the shear velocity $u_\tau = \sqrt{\tau_w/\rho_w}$, the viscous length scale $\delta_\nu = \mu_w/\left(u_\tau \rho_w\right)$, and ρ_w, where τ_w, ρ_w, and μ_w are the shear stress, density, and dynamic viscosity evaluated on the wall, respectively. For instance, $u^+ = u/u_\tau$, $y^+ = y/\delta_\nu$, etc. Additionally, α, β, and γ are coefficients that account for the influence of pressure and thermal effects and $y^+_s = 60$.

To achieve continuity between the two layers, laminar and turbulent velocities are blended [136] according to Eq. 3.19 and Eq. 3.20.

$$u^+ = e^\Gamma u^+_{lam} + e^{\frac{1}{\Gamma}} u^+_{turb} \tag{3.19}$$

$$\Gamma = -\frac{a\left(y^+\right)^4}{1 + by^+} \tag{3.20}$$

where $a = 0.01$ and $b = 5$. A similar approach is also applied for thermal transfer at the wall. In this way, the simulation is able to utilize a fine mesh near the wall region that is capable of resolving the diffusion boundary layer, while still allowing a coarser mesh to be used in the bulk flow region (Fig. 3.4 (c)). Initial simulations ran with the standard wall function approach did not perform

well when compared with experimental data and theory. This led us to adopt the enhanced surface treatment which was found to adequately capture the behavior of the experimental cell from both a theoretical and experimental standpoint. A more detailed explanation for this approach will be discussed below.

For boundary conditions, a non-slip boundary condition was defined at all walls. Since the reactions of interest occur under mass transport limited conditions and the use of a supporting electrolyte renders migration effect negligible, electrochemical effects can be ignored. Instead, the reaction at the electrode surface was defined as shown in Eq. 3.21 without a dependence on applied potential.

$$\text{rate} = k_0 \cdot C_{i,s} \tag{3.21}$$

Here, the reaction rate coefficient k_0 was selected to be large enough that the ferricyanide concentration at the electrode surface approaches zero for all rotations speeds. This approach allows for the condition of a mass transport limited reaction to be simulated without the complexity of electrochemical interactions. The electrode shaft was set to have an angular velocity ω in rad s^{-1} defined for each rotation speed according to Eq. 3.22.

$$\omega = \frac{2\pi f}{60} \tag{3.22}$$

where f is in revolutions per minute (rpm). All other surfaces were defined as walls without flux or motion. In the simulation, properties for ferricyanide and ferrocyanide were taken to be the same as water due to the dilute nature of the solution. Diffusivity for ferricyanide and ferrocyanide in water were defined as 6.3×10^{-6} cm^2 s^{-1} and 5.6×10^{-6} cm^2 s^{-1}, respectively [137].

Due to the unsteady nature of turbulent flow, a transient solution method was used for all simulations where each simulation started with stagnant fluid and the hydrodynamics were allowed to evolve over time to reach a pseudo-steady-state flow condition before activating the reaction conditions on the surface of the electrode. The reader should be certain to distinguish the steady-state

conditions discussed here from the steady-state solver used in other publications. The steady-state solver provides a single, *average* snapshot of the flow conditions in the reactor at steady-state, whereas our simulation uses a transient solver to resolve the fluid flow over time. Steady-state for the purposes of this publication refers to the condition where the change in average velocity of the fluid in the simulation fluctuates steadily around a single value. In this manner, we can still visualize the local fluctuations in velocity as a function of time throughout the reactor, but also know that the simulation has reached conditions where the momentum generation and annihilation are equal and there is no change in the average velocity field with time. Ensuring this condition before initiating the reaction at the catalyst surface was important for comparison with experimental data where the flow conditions in the reactor have been given time to reach steady-state before inducing an electrochemical reaction.

Simulation time steps used for each rotation speed were tuned to ensure accurate and stable simulation with a Courant number less than one by reducing the time step until further reduction no longer yielded changes in the simulation results. As such, finite time step sizes of 2, 1, 0.5, 0.4, 0.25, and 0.2 milliseconds were used for rotation speeds of 100, 200, 300, 400, 600, and 800 rpm respectively. All simulations were performed on the Hoffman2 Shared Cluster provided by UCLA Institute for Digital Research and Education's Research Technology Group using a 36-core dual processor with 192 GB of RAM. Due to the *steady-state* flow requirement of these simulations, we found that each simulation took about one week to reach a simulated time when this condition was met. While the scaling of the time step size with rotation speed reduced the computer processing time per second of simulated time, the amount of simulated time that was required to reach steady-state flow was longer for simulations with larger step sizes. The increase in simulation time required for low rotation speed was simply due to slower transfer of momentum from the shaft into the bulk of solution caused by the smaller velocity gradient. This resulted in similar computer processing time for all rotation speeds of 7 to 10 days to reach simulated times when steady-state flow conditions were reached. After integrating reaction chemistries in Ansys

Fluent, simulations were run for another 7 to 10 days to reach at least 20 seconds of process time. All simulations required a unique time for the reaction rate to develop mass transfer limited conditions, so steady-state reaction conditions were defined to be after 10 seconds of simulated time with reactions enabled. Estimates of the time required for the diffusion boundary layer to develop, were highest for 100 rpm at approximately 5 seconds. Thus, allowing 10 seconds of simulated time for equilibration was considered adequate, and a minimum of 10 additional seconds to observe the steady-state behavior was used in evaluating reaction conditions at steady-state.

3.4.4 Evaluation of simulation method

The previous sections describe our final simulation method for capturing the hydrodynamics of the RCE reactor. However, the justification for this method is best evaluated in comparison to other methods we tested that did not yield accurate results. As such, this section provides greater detail about the impact of each key method used on the local conditions in the simulation, as well as the overall impact on the simulation performance.

We found that the key aspects necessary to accurately simulate the RCE reactor were the use of the enhanced surface treatment method combined with an adequately refined mesh that together provide good resolution of the concentration and hydrodynamic boundary layer. Initial simulations were performed similarly to previously reported RCE CFD simulations where a universal velocity function was assumed at the wall of the rotating cylinder using a standard wall function. However, this wall treatment method is designed for a coarse mesh where the diffusion boundary layer is not resolved. Because of this simplification, using a mesh that is sized to resolve the boundary layer causes issues when determining the velocity profile at the wall. Fig. 3.5 (a) shows this issue, where a sharp drop close to the wall is observed when the standard wall function is used with our initial mesh, which is problematic for accurately predicting momentum transport at the shaft surface. In comparison, the enhanced wall treatment method, using the two-layer approach, is designed to be used with a fine mesh near the wall that can resolve each layer of the hydrodynamic boundary

layer. Since a fine mesh is required to capture the diffusion boundary layer, the enhanced surface treatment method is well-suited to capture momentum transfer at the wall. As illustrated in Fig. 3.5 (a), the enhanced surface treatment method is better able to capture the hydrodynamic boundary layer by providing a smooth transition in velocity as a function of the distance from the wall. This profile is closely matched to what would be expected based on turbulent boundary layer flow theory. In addition to the enhanced surface treatment methods, an adequately fine mesh is required at the wall to capture both momentum transfer and the physics of the diffusion boundary layer. This can be demonstrated by comparing the results obtained for a boundary layer mesh composed of ten 37 μm thick cells, to our final boundary layer mesh that is 20 layers thick and has a first cell height of 3 μm. While a slight increase in momentum transfer from the wall can be discerned in Fig. 3.5 (a) when the mesh is refined, the effect is more significant for the diffusion boundary layer. Fig. 3.5 (b) shows that while changing to an enhanced surface treatment method helps capture the curvature of the diffusion boundary layer better than the standard wall function, the coarse mesh is simply not fine enough to capture the concentration gradient at the wall. This results in only five cells inside the boundary layer and a near linear approximation for the changes in concentration as a function of position. However, when the refined mesh is used, the full curvature of the diffusion boundary layer is captured (shown in red) by ten cells at 800 rpm. This refinement also improved the ability of the simulation to capture the momentum transfer from the surface to the fluid, allowing the simulation to resolve the viscous sublayer and capture vortex formations near the surface that was obscured by the coarse mesh.

Besides the local differences displayed in Fig. 3.5 (a) and Fig. 3.5 (b), the impact of these methods on overall performance of the simulation in describing the reaction rate or current density can be observed in Fig. 3.5 (c). Here, the standard wall function (shown in black) does not capture fluctuations in the current density. Non-fluctuating current density is to be expected with the $\kappa - \epsilon$ turbulence model and the standard wall function because this model is an averaging approach that does not capture the individual random fluctuations of turbulent flow. However, the magnitude

of the current density is lower than expected. By implementing the enhanced surface treatment method, fluctuations can be observed in the current density (shown in gray). While the $\kappa - \epsilon$ model still does not allow resolution of the random turbulent fluctuations in the velocity field, the two-layer approach employed by the enhanced surface treatment method does allow structured vortices (non-random) inside the hydrodynamic boundary layer to be captured. Further discussion and justification for these surface vortices is provided in the discussion of the simulation results. Further refinement of the mesh to fully resolve the diffusion boundary layer and utilization of the enhanced surface treatment method, together, provided both the disturbances to the current density and the correct magnitude of current density (shown in red). This result is due to the increased resolution of mass transport in the diffusion boundary layer.

3.5 Results and discussion

Accuracy of the simulation in modeling the performance of the experimental RCE reactor can be evaluated by at least two metrics: agreement with the previously discussed universal dimensionless relationship for mass transport and closely matched transient behavior of the current density. While the dimensionless relationship helps evaluate the ability of the simulation to capture the time averaged multiscale nature of the reactor as Re is increased, the transient behavior of the current density informs us of the ability of the simulation to capture the mechanisms of mass, heat, and momentum transfer at the electrode surface. As mentioned previously, small oscillations in the current density as a function of time are commonly observed in experimental electrocatalysis. This has been attributed to eddy or vortex formations [132] on the electrode surface due to the turbulent conditions that are created even at particularly low rotation speeds for rotating electrodes or by the bubbling of gases in cells using static electrodes. The fluctuations in the current density observed experimentally are thought to be a unique fingerprint of the reactor hydrodynamics. Modeling this behavior is necessary to gain insight as to how the hydrodynamics of the RCE affect its perfor-

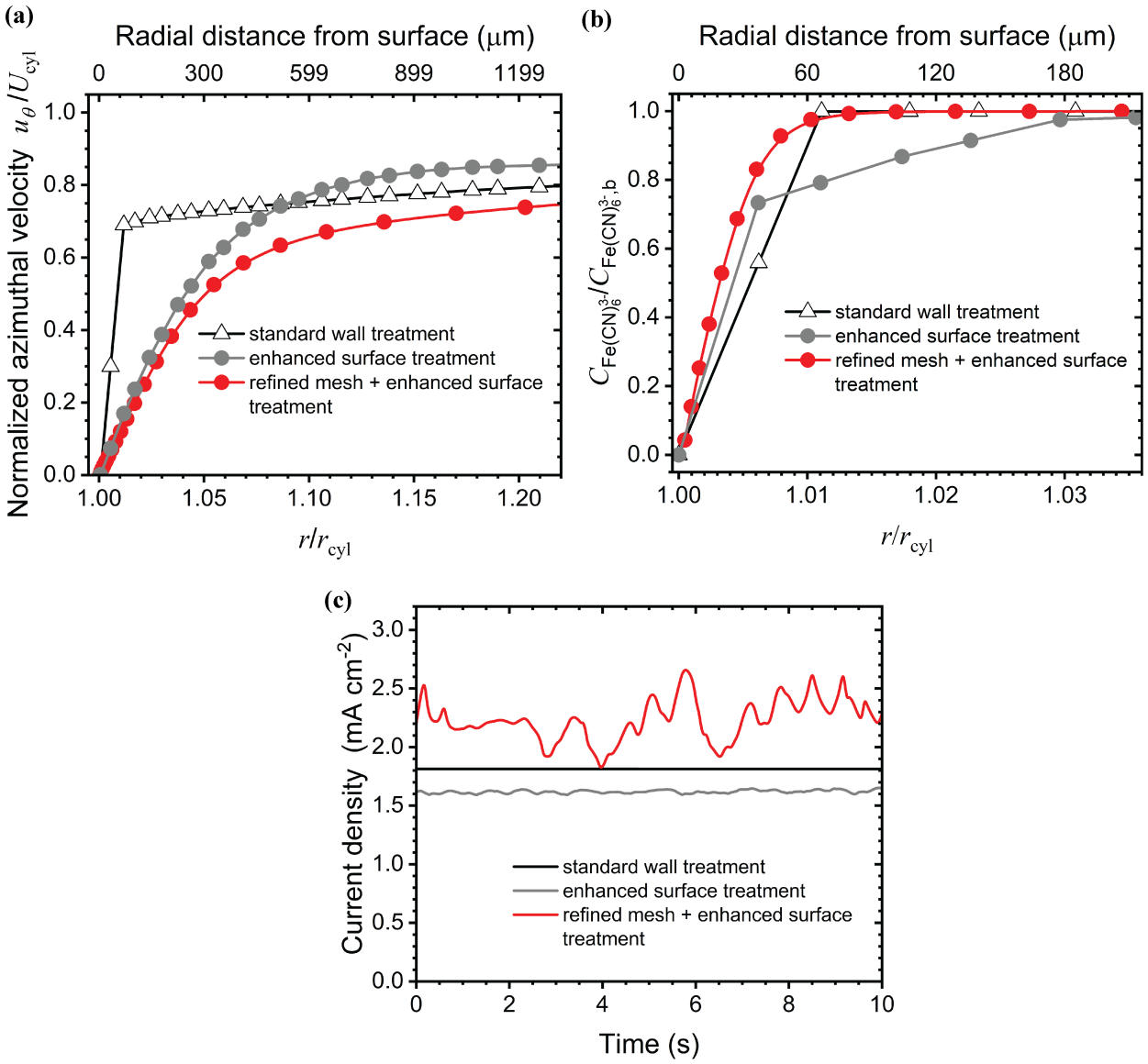

Figure 3.5: CFD simulation results for the electrochemical reduction of ferricyanide in the RCE reactor at a rotation speed of 800 rpm. Effect of surface treatment method and mesh refinement on simulation of the (a) hydrodynamic boundary layer, (b) diffusion boundary layer, and (c) transient current density.

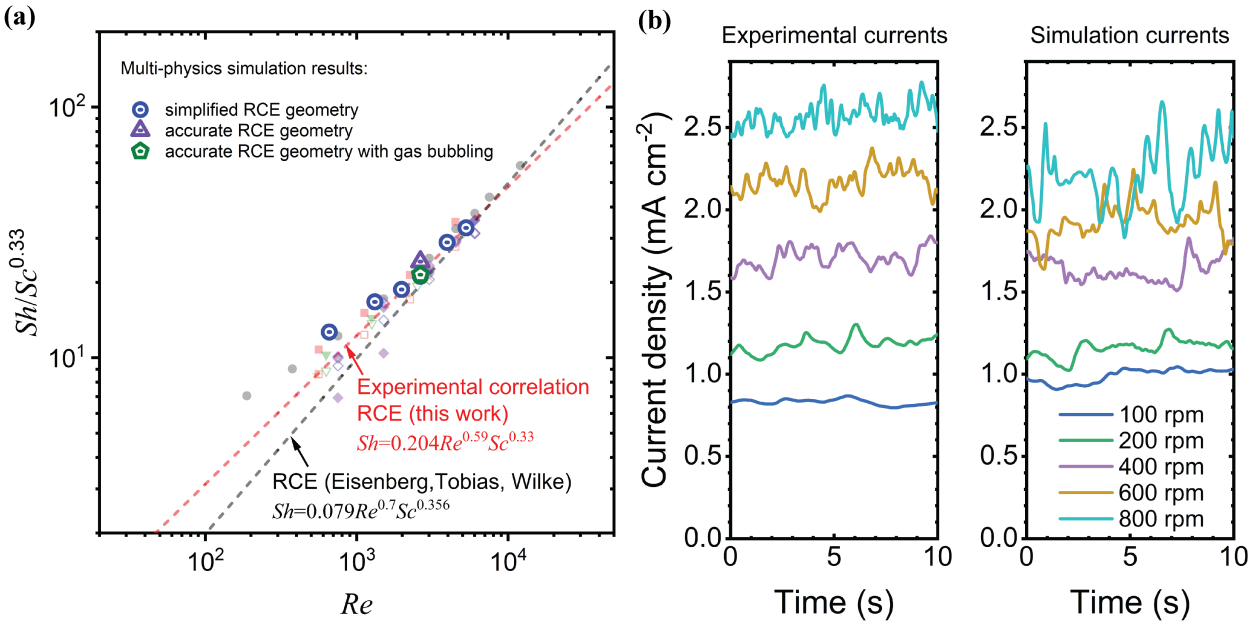

Figure 3.6: Simulated currents for ferricyanide reduction and development of dimensionless relationships between transport and hydrodynamics for results obtained in the multi-physics model of the RCE reactor. (a) Relationship between Sherwood and Reynolds numbers extracted from the multi-physics models and their comparison to experimental relations extracted for the RCE reactor. Experimental data from Fig. 3.2 (b) is shown in the background for comparison. Detailed experimental methods are reported in [7]. (b) Comparison of transient behavior of the RCE current density for ferricyanide reduction at different rotation speeds under mass transport limited conditions, showing the fluctuations caused by vortices near the surface. A 0.1 M potassium perchlorate solution with the addition of 0.01 M potassium ferricyanide was used as electrolyte for the ferricyanide reduction experiments.

mance.

Beginning with the universal dimensionless relationship between Sh and Re shown in Fig. 3.6 (a), we observe that there is excellent agreement between the simulated results and experimental data. High rpm results align closely with the experimentally derived relationship for our gastight RCE reactor. The correlation derived by Eisenberg, Tobias, and Wilke for ferricyanide reduction in an RCE reactor on a flat rotating cylinder electrode is also plotted to show the agreement between the results of our RCE and previously published correlations for similar reactor geometries [119, 138]. Slight differences in correlation constants are common for different reactor and electrode geometries, but all correlations fall close to the same line [113, 139]. At low rpm, the simulation also captures the deviation from the correlation that we observe experimentally for

ferricyanide reduction shown by the black dots. The agreement between the experimental and simulated transient current density can also be discerned in Fig. 3.6 (b). Not only is the magnitude of the current density well-matched, but also the frequency and amplitude of the fluctuations. Most notable is how the frequency and amplitude change with rotation speed in both the experimental and simulation results. Together, agreement with the universal relationship and transient behavior, suggest that the simulation method presented here, accurately captures the hydrodynamics of the RCE reactor. To confirm that the assumptions made in simplifying the reactor geometry used in these simulations were justified, comparison is made to simulations ran using the accurate geometry at 400 rpm. These simulations were performed using meshing and solution methods identical to that of the simplified mesh shown in Fig. 3.4 (c) to ensure a direct comparison. The major assumption used in the geometry simplification was that disturbances in the bulk of the reactor have a minor effect on the hydrodynamics in the near wall region that is relevant to electrochemical reactions. Indeed, we find that bulk disturbances have minimal effect on mass transport to the surface of the catalyst. These disturbances can be identified in Fig. 3.6 (a) by the close alignment of the data points collected using the simplified and accurate geometries. Even when gas bubbling was introduced, the difference between the simplified and accurate geometry results were minimal. This observation is not surprising, as the diffusion boundary layer is significantly smaller than the viscous sub-layer due to the large Sc number used in this study.

Further comparison can be made between the effects of the two geometries by examining the flow patterns of the fluid presented in Fig. 3.7. Here, Fig. 3.7 (a) and Fig. 3.7 (b) show a vertical and horizontal cross-section of the fluid flow patterns in the simplified geometry, while Fig. 3.7 (c) and Fig. 3.7 (d) show the same cross-sections for the accurate geometry. All images are taken at steady-state flow conditions for a cylinder rotation speed of 400 rpm. The horizontal cross-sections are taken at the center of the catalyst, as shown by the red dashed line. The color scale tied to the fluid velocity delineates two main regions in the liquid phase of the reactor. Near the rotating shaft, steep velocity gradients occur where surface vortices can be differentiated. Fluid velocity

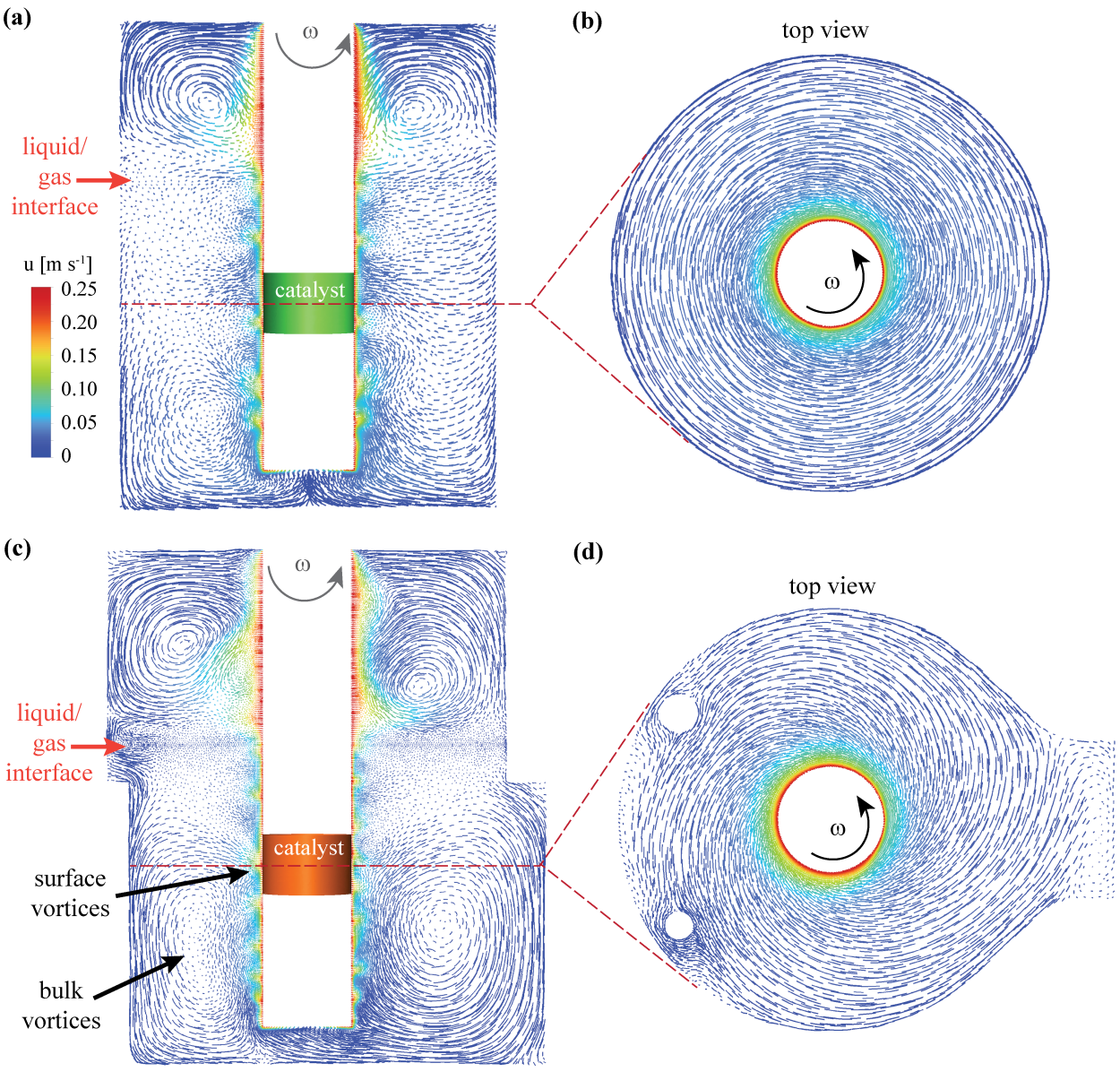

Figure 3.7: Cross-sections of the (a,b) simplified and (c,d) accurate geometry showing the flow patterns of fluid in the RCE reactor at 400 rpm. (b) and (d) show horizontal cross-sections at the location indicated by the red dashed line. Fluid behavior is similar for both geometries, especially in the region close to the shaft surface that is most significant for electrochemical transformations. Here structured vortices cause local disruptions to mass transfer at the catalyst surface while bulk vortices have a negligible effect on the near wall region.

quickly decreases with increasing distance from the surface, and a relatively low velocity region can be observed in the bulk of the fluid shown in blue. Here, large vortices can be identified in this bulk region spanning the annular space between the shaft and the outer wall of the reactor. Slight differences in the flow of bulk fluid can be identified between the two geometries caused by the reference electrode, gas sparger, and counter electrode channel. However, the region close to the electrode that is relevant to electrocatalysis appears identical between the two geometries. In evaluating the effect of bulk flow patterns on mass transport at the surface, a simple comparison can be made between the velocity field shown in the bulk and near the shaft surface. The color scale indicates that fluid near the shaft surface is an order of magnitude higher for velocity relative to the fluid in the bulk. This alone is enough to suggest that disruptions in the bulk of the fluid are unlikely to contribute significantly to the mechanisms of mass transport near the surface of the catalyst, and further validates the assumptions made in simplifying the geometry. This holds true, at least, under conditions of high electrode rotation speeds shown in Fig. 3.7.

3.5.1 Structured flow patterns in the RCE reactor

Now that simulation results have been shown to agree with our experimental observations, a detailed analysis of the simulation results can be used to gain insight about the mechanisms driving mass transport in the RCE. Under the reaction conditions investigated here, we find that two regions with structured vortex formation occur in the RCE reactor. Bulk vortices are identified spanning the annular space between the rotating shaft and the reactor walls, and surface vortices form inside the hydrodynamic boundary layer, close to the electrode surface. Beginning with the bulk vortices, one might be tempted to identify these as Taylor vortices. Taylor vortices have been well documented and are widely known to develop in fluid between rotating concentric cylinders [139–141]. CFD simulations of rotating cylinders consistently predict the formation of Taylor vortices as well: especially with generalized wall functions and coarse mesh [142–145]. This result is to be expected, since Taylor vortices are structured flow patterns that form outside the viscous

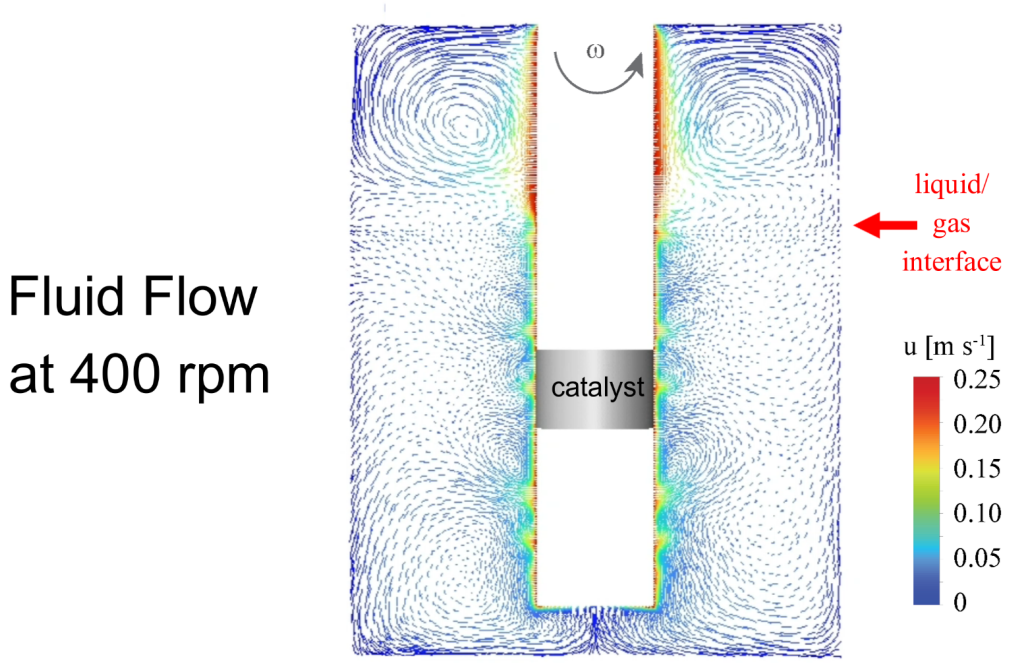

Figure 3.8: A video showing the fluid flow patterns develop in the RCE reactor in real-time. Vortices that resemble Taylor vortices initially form in the bulk, but are quickly disrupted by surface vortices. Surface vortices can be observed to move across the surface of the shaft, while a bulk vortex created by an edge effect at the bottom of the shaft stabilizes in the lower half of the liquid volume. This video is constructed from a series of cross-section images taken from data files in intervals of 0.1 s of simulated time.

sublayer and unstructured turbulent layer. However, as depicted in Fig. 3.7 (a) and Fig. 3.7 (c), only one large vortex is formed in the RCE. If stable Taylor vortices were to form, semi-uniform counter rotating vortex pairs would be expected with approximately equal width and height across the annular space. In fact, this behavior is observed in the first few seconds after rotation of the shaft is initiated, which is also visualized in Video 3.8.

As the simulation time progressed, the Taylor vortices were quickly disrupted by the formation of smaller vortices near the surface of the electrode and a significant edge effect caused by the base of the shaft. The role of the edge effect can be discerned in the video in Fig. 3.8, and in the still images in Fig. 3.7 where the fluid near the base of the reactor flows up near the electrode and down at the reactor wall. This edge effect is caused by the bottom of the shaft where the rotating surface pulls fluid from below to replace fluid being ejected from the sides by centrifugal force. At

the outer wall of the reactor, fluid is being pulled down to replace fluid under the shaft, while the fluid around the base of the shaft is directed upward. The effect is most pronounced at low rpm where the azimuthal velocity of the fluid is lower, and is overshadowed by azimuthal fluid motion as rpm is increased, which is shown in Fig. 3.9 (a) by the disappearance of the bulk vortex as rpm is increased. At first glance, the behavior of the vortex in the bulk might be confused with a Taylor vortex, but the originating mechanism is quite different.

The second distinct region of fluid presented in Fig. 3.7 is the region near the surface of the shaft where small, high intensity vortices form in counter rotating pairs. These vortices remain relatively stable on the surface, increase in frequency with rotation speed, and move across the surface as shown in Fig. 3.8. Looking at Fig. 3.9 (a) and Fig. 3.9 (b), we see that these vortices also become more compact with increasing rotation speed, and appear to have a non-trivial influence on fluid motion close to the electrode surface. The size of these vortices appears to be tied to velocity gradient. In Fig. 3.9 (b) we can see that as the gradient increases with rpm, represented by an increase in color gradient. These vortices also become smaller in Fig. 3.9 (a) and move closer to the surface as illustrated in Fig. 3.9 (b). Vortices particularly similar to these, named Görtler vortices, have previously been shown to occur inside the laminar sub-layer near curved surfaces where steep velocity gradients occur [146]: like those found in this RCE. These vortices are known to develop simultaneously with Taylor vortices and are thought to be a key mechanism in the transition from structured vortex formation to bulk, unstructured turbulent flow [147]. This, along with the flow pattern caused by the bottom surface of the shaft, is likely why Taylor vortices are not observed in this RCE at steady-state flow conditions.

3.5.2 Analysis of surface vortex effects

While azimuthal velocity is still dominant near the surface, we can see that the surface vortices do influence the fluid motion in the radial and axial directions. In between the vortex pairs, a jet-like feature forms where fluid is pulled away from the surface. This feature is best shown in

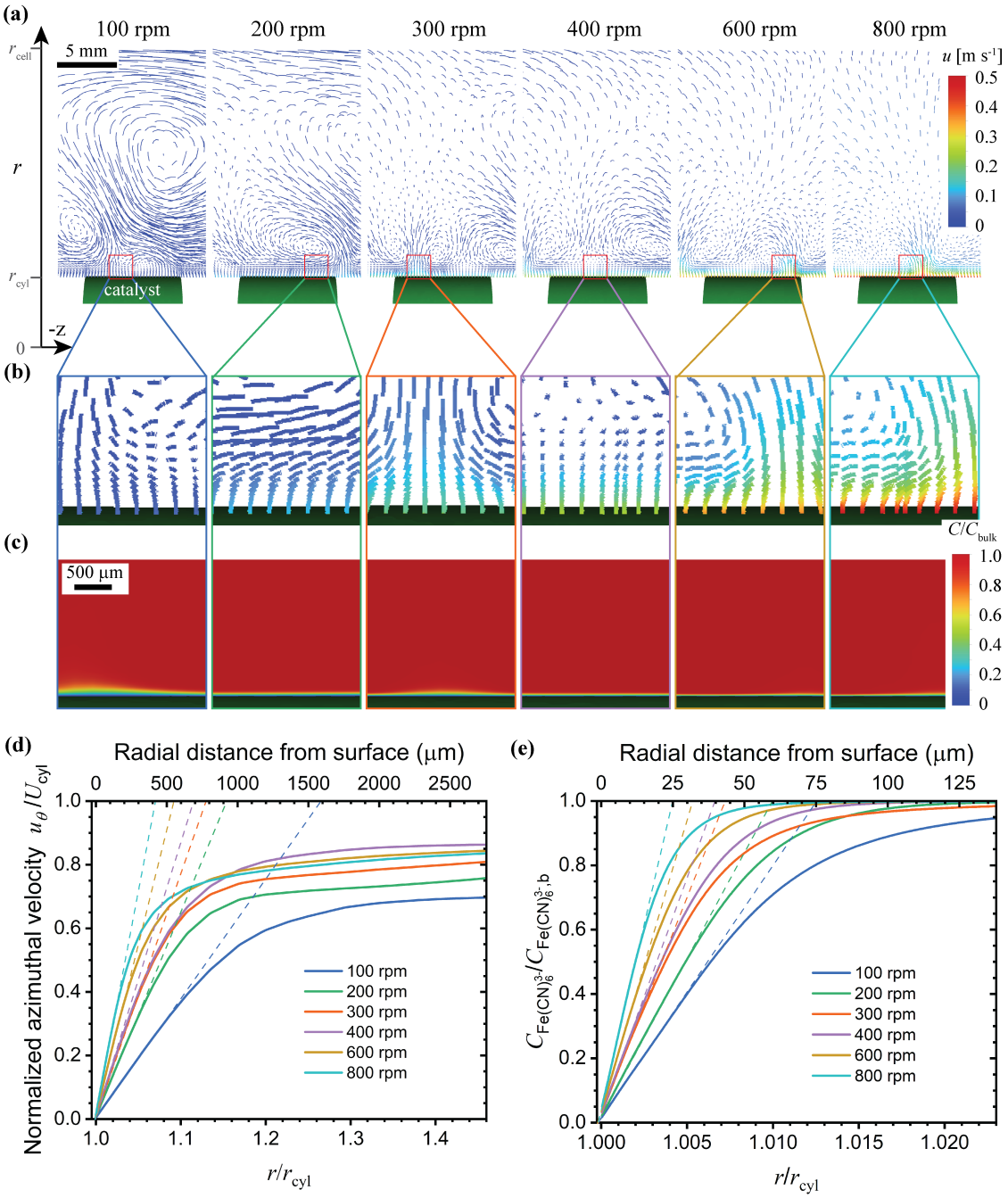

Figure 3.9: (a) Cross sections of the fluid normal to the electrode surface showing fluid flow patterns at each rotation speed. (b) Close up of the fluid flow patterns at the electrode surface showing how the effects of the surface vortices move closer to the electrode surface as rotation speed is increased and how the velocity gradient increases. (c) Heat maps of ferricyanide concentration at different rpm showing the influence of the surface vortices on the diffusion boundary layer and how increasing rotation speed reduces the diffusion boundary layer thickness. Normalized Boundary layers profiles for (d) azimuthal velocity and (e) ferricyanide concentration, showing the reduction in boundary layer size for each as a function of rpm

Fig. 3.9 (b) for 300 rpm. This jet-like feature is tied to a local expansion of the diffusion boundary layer caused by an increased resistance to diffusion in the direction of the catalyst resulting from the radial velocity influence in that region. This behavior is best shown in Fig. 3.9 (c) for 100 and 300 rpm. At the outer edges of the vortex pairs, fluid is directed toward the shaft surface, while directly under the vortex, fluid is directed across the surface in the axial direction. This results in increased mass transfer by bringing bulk fluid close to the surface, and a reduction in the local diffusion boundary layer thickness. This effect is best shown in Fig. 3.9 (c) for 200 and 400 rpm. It should be noted, that while the local diffusion boundary layer thickness is slightly changed by the presence of these vortices, the average value is still dominated by the random turbulence modeled by the $\kappa - \epsilon$ method. However, these local fluctuations in diffusion boundary layer thickness result in local variation in mass transfer rates to the catalyst surface, and are most likely the source of fluctuations in the current density that we observe in the simulations. These surface vortices can be thought of as an additional convective transport mechanism that is unique to the rotating cylinder geometry. The minor role that these vortices play in determining mass transfer rates can be examined by comparing the scale of the vortices to the scale of the diffusion boundary layer. In Fig. 3.9 (d) we see that the hydrodynamics boundary layer calculated from the velocity gradient at the surface ranges between 400 and 1600 μm, while Fig. 3.9 (e) shows that the diffusion boundary layer calculated from the concentration gradient at the surface ranges from 25 to 75 μm. By revisiting Fig. 3.9 (a), Fig. 3.9 (b), and Fig. 3.9 (c) we can see which effects are influential at these different scales. Notably, in Fig. 3.9 (b) and Fig. 3.9 (c) we can see that the region of swirling fluid where surface vortices are present, is far from the region of fluid containing the diffusion boundary layer. Even at 800 rpm, where both boundary layers are the most compact, the velocity in the azimuthal direction (out of plane) is aligned with the surface, showing that the vortices have minimal influence in that region.

While the fluctuations caused by these surface vortices may at first appear to be problematic for the investigation of intrinsic kinetics, a few points should be noted. First, the variation of the local

mass transfer rates is small in comparison to the magnitude of the total mass transfer rates. These mass transfer rates can be studied by comparing the amplitude of the current density fluctuations to the magnitude of the current density in Fig. 3.6 (b), Fig. 3.1 (c), Fig. 3.1 (d), and Fig. 3.1 (e). Second, these fluctuations are due to a convective mixing action that enables control of the mass transfer rate at the surface by controlling the rotation speed. The change in mass transfer rates due to increased convection is far greater than local fluctuations. This change can be examined by comparing the change in current density magnitude as the rotation speed is increased, to the amplitude of the fluctuation in Fig. 3.6 (b), Fig. 3.1 (c), Fig. 3.1 (d), and Fig. 3.1 (e). With the variation in local mass transfer rates being so small in comparison to other effects, the RCE should still allow for the effects of mass transport and intrinsic kinetics to be decoupled effectively.

Current density fluctuation observed in the simulated and experimental studies reported here, are common to many experimental electrochemical reactors that are used to study intrinsic kinetics. In comparison to these, the RCE offers the distinct advantage of being able to precisely define the mass transport conditions over a large catalyst surface whereas other reactors (especially those with large surface areas such as the compression H-cell commonly used in electrochemical CO_2 reduction studies) have poorly defined hydrodynamics conditions that can be significantly influenced by slight variations in experimental conditions, such as the rate at which gas is bubbled through the bulk of the solution or the rate of rotation of the stirrers reported to be used in some of these cells.

3.5.3 Effects of rotation speed on boundary layer development

Further insight as to the behavior and contribution of both the bulk and surface vortices can be gained by comparing the nondimensionalized hydrodynamics boundary layer profiles. Fig. 3.10 (a) shows the nondimensional velocity (u^+) vs. the nondimensional distance (y^+) for each rotation speed averaged at three lines located at 1/4, 1/2, and 3/4 of the electrode height. These are compared to the universal boundary layer profile for turbulent flow over a smooth surface, indicated by

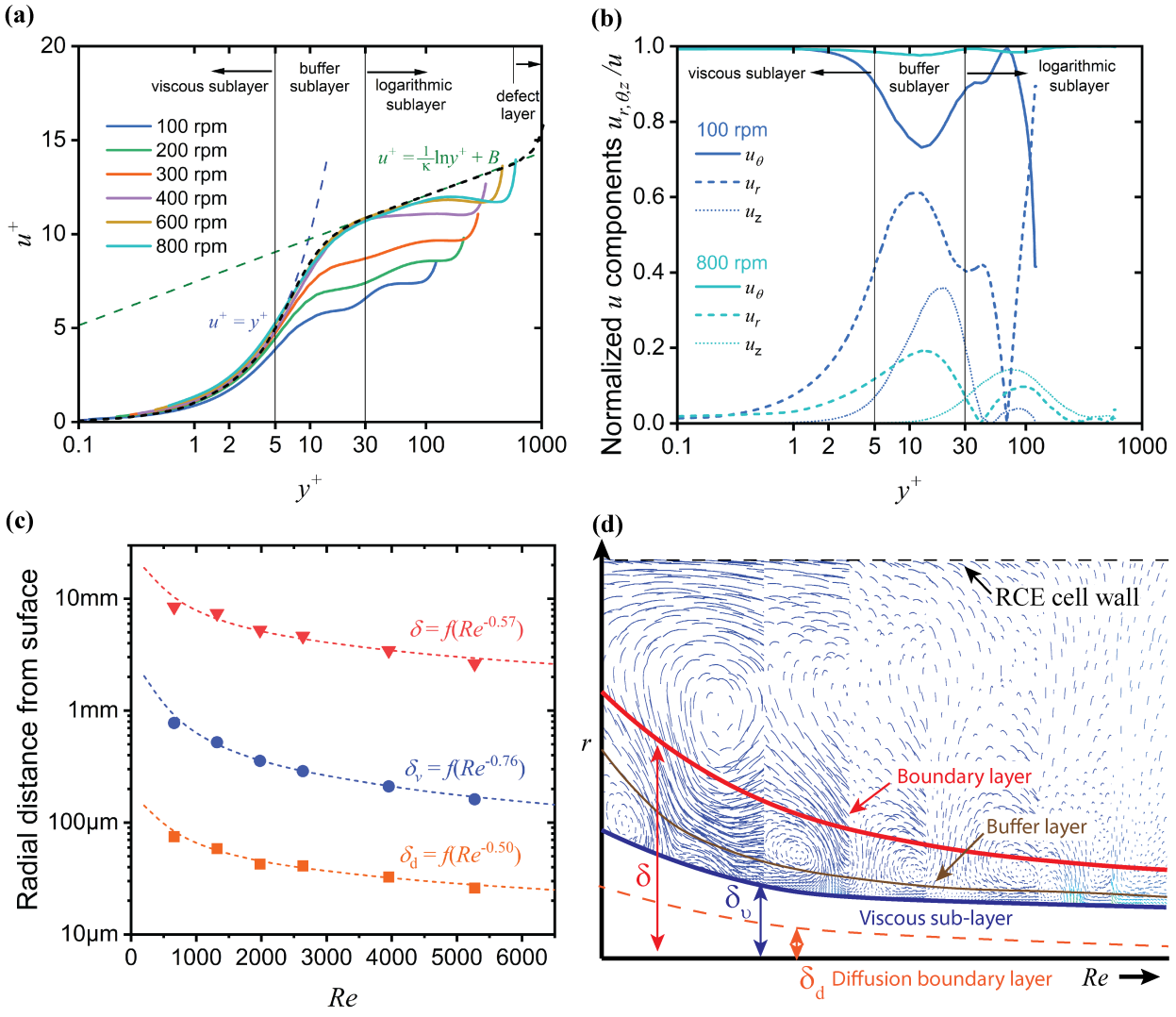

Figure 3.10: (a) Nondimensionalized velocity (u^+) vs. distance from the wall (y^+) showing the degree of agreement between simulated velocity profiles and experimentally measured, universal velocity profiles for turbulent flow over a smooth surface. Here κ is the Von Kármán constant, 0.41, and B is experimentally determined to be 5 for turbulent flow. Profiles at low rpm deviate significantly from ideal behavior due to vortex contributions. (b) Relative contributions of each component of the total velocity vector vs. y^+. Here, the velocity component is normalized to the magnitude of the total velocity to show how at low rotation speeds, radial and velocity components contribute more significantly than at high rpm. (c) Hydrodynamic boundary layer (δ when u is 99% of the bulk velocity), Viscous sublayer (δ_v), and diffusion boundary layer (δ_d) thickness and their dependence on Re. (d) Exaggerated representation of the different boundary layer regions showing their positions relative to each other and how they change with Re. The background shows how the flow field develops so that surface vortices are contained in the region between δ and δ_v and bulk flow vortices are overcome by the azimuthal velocity

the dashed lines. Inside the laminar sublayer $u^+ = y^+$, while in the turbulent or logarithmic sublayer u^+ is a logarithmic function of y^+. Between these two layers, the velocity holds to a blended function of the two regions. In the logarithmic relationship, κ is the Von Kármán constant 0.41, and B has been experimentally determined to be 5 for turbulent flow over a smooth surface. In our simulations, we see that at low rotation speeds of 100 to 300 rpm, the profile deviates significantly from the universal profile, while at speeds above 400 rpm, the profiles behave more ideally. This correlates with what we see in Fig. 3.6 (a) where at low Re, Sh is higher than the correlation would suggest it should be. The reason for this deviation from ideal behavior can be identified by comparing the relative contributions of each component in the velocity vectors depicted in Fig. 3.10 (b). Here, the magnitude of each velocity component is divided by the magnitude of the total velocity vector to show the contribution of each component relative to the total velocity magnitude. 100 and 800 rpm are compared to provide contrast between low and high rotation speeds. At both 100 and 800 rpm, u_θ is the dominant component of the velocity across most of the fluid. However, at low rpm, u_r and u_z contribute far more significantly than at high rpm. Notable contributions from u_r can be observed as close to the surface as $y^+ = 2$ (well inside the viscous sublayer). At high rpm similar levels are not reached until $y^+ = 10$ (in the buffer layer). Under vortex free flow, there would be little to no u_r or u_z contributions.

These contributions from u_r and u_z originate from the development of vortices that mix fluid near the wall with fluid from the bulk. The mixing action of these vortices causes two significant effects. First, low and high velocity fluid are mixed in regions where vortices are influential. This behavior is why the velocity (u^+) is lower in the regions where u_r and u_z have significant contributions. At higher rpm, this vortex induced mixing action is less influential than the momentum being transferred from the wall and the velocity increases until it aligns with the universal velocity profile as illustrated in Fig. 3.10 (a). There, the direction of fluid flow is primarily aligned with the rotation of the shaft in the azimuthal direction. The second effect is that this vortex induced mixing action also enhances mass transport by bringing bulk concentration fluid to the surface and

mixing it with lower concentration fluid in the boundary layer. This effect is why the Sh is higher than the expected value for 100 and 200 rpm. Here the influence of the surface vortices is simply significant enough in regions near the diffusion boundary layer to enhance mass transport. It is especially helpful to note, that the outer edge of the diffusion boundary layer is located at $y^+ = 1$ for all rotation speeds. Knowing this we can again refer to Fig. 3.10 (b) and see that at 100 rpm, the influence of u_r does indeed influence the region closer to the surface than $y^+ = 1$ suggesting that vortices do influence the concentration boundary layer at this rotation speed. Whereas at 800 rpm, u_r does not start becoming influential until $y^+ > 1$. Explained simply, at low rotation speeds, the increased contributions of u_r and u_z signify an increased convective mass transport effect caused by vortex formation that is reduced as rpm is increased and both δ_v and δ_d are compressed closer to the wall.

Finally, extraction of boundary layer thicknesses enables the identification of their relationship to rotation speed and to each other. Three boundary layers of importance are plot as a function of Re in Fig. 3.10 (c). The hydrodynamic boundary layer, δ is found to relate to the Re by an exponent of -0.57. Here δ is defined as the distance from the wall where 99% of the bulk velocity is reached. We can see that as Re is increased, δ decreases from around 10 mm at 100 rpm, to 2 mm at 800 rpm. As shown in the exaggerated representation of the flow development observed in Fig. 3.10 (d), the surface vortices fall inside this boundary layer.

The viscous sublayer, δ_v on the other hand, falls in the 0.1 to 1.0 mm range: below the region where surface vortices form. Here δ_v is defined as the distance from the surface at $y^+ = 5$. In this region, azimuthal velocity dominates and nearly laminar flow is observed as shown in Fig. 3.10 (a) and Fig. 3.10 (b). We find that δ_v is related to Re by a power of -0.76 shown in Fig. 3.10 (c). Since y^+ is normalized by the shear stress at the wall, and the shear stress is proportional to the velocity gradient at the wall, this means that the velocity gradient at the wall has an identical dependency on Re. For flow over a flat plate, the laminar boundary layer was found by the Blasius solution to have a power of -0.5 dependency on Re. Thus, we find that the effect of turbulence on

the laminar sublayer is the difference in exponent of -0.26, indicating that the laminar sublayer is smaller than what would be expected for laminar flow.

Likewise, the diffusion boundary layer is plotted as δ_d where we see a dependency on Re to the power of -0.5. In this case, δ_d is defined as the linear diffusion boundary layer thickness calculated by the concentration gradient at the wall and the bulk concentration of ferricyanide. δ_d is observed to be in the range of tens of micrometers and is deep inside the viscous sublayer. It should be noted here that δ_d is the linear approximation presented in Fig. 3.9 (e) and does not capture the enhanced mass transfer caused by convection at the outer edge of the diffusion boundary layer. This relationship of $Re^{-0.5}$ is significant in that the same relationship is observed for Fickian diffusion in the RDE described by the Levich equation [122]. This tells us that at a region near the wall of the electrode, mass transport is described by Fickian diffusion. It must be noted here that Fickian diffusion can be applied only for simple electrocatalytic transformations, such as the reduction of ferricyanide, as this does not involve the reabsorption and further transformation of reaction intermediates. As pointed out in Section 3.3, Fickian diffusion can not be applied to rationalize stochastic transport-reaction processes relevant to more complex electrocatalytic processes, such as the reduction of CO_2 on copper electrodes. Additionally, we know that δ_d is inversely proportional to Sh which means that mass transport in our reactor is related to the Re in our RCE reactor as expressed in Eq. 3.7 by a power of -0.59. From this relationship, we can then determine that the turbulent contribution to mass transport at the catalyst surface is described by the difference in the exponent experimentally measured and that calculated for the local mass transfer within the first layers of fluid at the electrode (-0.09). Lastly, from literature it is commonly known that the diffusion boundary layer thickness is proportional to the laminar boundary layer thickness by $Sc^{-1/3}$ for flow over a flat plate. However, using the relationships we have determined here, we see that there is an additional dependency of the Reynolds to the power of 0.26 such that $\delta_d \propto \delta_v Re^{0.26} Sc^{-1/3}$. Note that while changing the properties of the dilute reacting species in solution will change δ_d, the effects of the hydrodynamic boundary layer behavior will remain the

same.

The effect of the electrode roughness on the hydrodynamics around the RCE has not been discussed here, but it is also an important parameter for electrocatalysis. As the viscous sublayer thickness in the rotations studied here remains large and in the order of a few tens of micrometers, the RCE cell should allow the decoupling of internal and external mass transport in porous electrodes where the length of the pore is smaller than the viscous sublayer, which is the case for most of the nanostructured coatings used in catalysis where the porous catalyst films range from a few nanometers to a few micrometers in size. Depending on the roughness and aspect ratio of the porous film, however, it is expected that roughness will start to play a role in affecting the structure of the viscous sublayer as the dimensions of the catalyst particles and the viscous sublayer thickness become closer in magnitude.

3.6 Conclusions

Developing advanced electrochemical reactors capable of efficiently producing chemicals at industrial scales requires a deep understanding of the underlying processes that govern reactor performance. The complex interactions between mass, energy, and charge transport as well as reaction kinetics makes gaining this understanding difficult, especially when attempting to apply these principles across multiple scales. Developing reliable relationships requires collection of high fidelity data sets with specialized reactors, like the gastight RCE, that enable the contributions of individual effects to be decoupled. Still, effectively utilizing the information gained by these experiments to inform the design of large scale reactors can be difficult due to the nonlinear complexity of the mass, heat, and charge phenomena involved. Utilization of multiscale computer modeling can enable the combination of these effects into a single model that covers a wide range of time and length scales. With correctly defined parameters, multiscale modeling methods such as CFD, MD, and DFT can be integrated to provide accurate simulations of complex reactor behavior

and provide detailed information about the intrinsic behavior of a reactor. This information can then be used to inform the design of industrial scale reactors or even test these designs *in silico*.

Here we have provided a detailed account of the first step in our development of a CFD model capable of capturing the performance of our gastight RCE reactor. In the pursuit of a model that can predict the behavior of our reactor for CO_2 reduction, we have divided the model development in to a series of experimentally verifiable stages. The first stage, presented here, is establishing the hydrodynamics in the reactor. This was accomplished by developing a simplified model capable of simulating the transient and time averaged behavior of the mass transport limited ferricyanide reduction reaction. Under the conditions of interest in this reactor, the diffusion boundary layer is well within the hydrodynamic boundary layer. Turbulent flow is known to disrupt this diffusion boundary layer, causing frequent low intensity fluctuations in the current density that can be detected experimentally. Capturing this unique behavior was the key to ensure an accurate model of the hydrodynamics in revealing the need to utilize enhanced surface treatments and fine mesh to describe the electrode/electrolyte interface.

We find that surface vortex formation near the outer edge of the viscous sub-layer is primarily responsible for these fluctuations. The ability of the model to capture this behavior as well as the correct magnitude of the current density across a rotation speed range of 100-800 rpm is primarily due to two features of the simulation: the use of an enhanced surface treatment method and a fine mesh near the surface. Due to the small size of the diffusion boundary layer compared to the hydrodynamic boundary layer, an appropriately fine mesh was required near the electrode surface to capture the concentration gradient. On the other hand, the enhanced surface treatment method implemented a two layer approach to model fluid flow near the wall that allowed for the use of this fine mesh near the surface, and a coarse mesh in the bulk of the fluid. This refined mesh near the surface was also responsible for allowing the model to capture the development of surface vortices in the near wall region. We also note that this characteristic flow pattern can be obscured by a more coarse mesh and simplified wall treatment. Additional simulations with a

reactor accurate geometry also show that changes in the bulk flow outside the boundary layer, have minimal effect on the performance of the reactor model, which is consistent with experimental observations. We find that as the rotation speed increases and the boundary layer shrinks, the effect of the surface vortices is shown by an increase in amplitude and frequency of current density fluctuations. However, above 400 rpm the change in boundary layer thickness is smaller relative to the change in rpm and the frequency of surface vortices increases, thus causing a reduction in amplitude and an increase in frequency of current density fluctuation.

In addition to capturing the transient behavior of the RCE reactor, the simulation also captures the relationship between Sh and Re that was previously determined for this RCE reactor and closely aligns with other published correlations. The simulation method presented here was found to provide an accurate representation of the hydrodynamics of the RCE that are pertinent to modeling electrochemical reactions at the surface of the electrode. This method can be applied to reactors with similar architecture to provide insight into the hydrodynamics of the reactor. Future work will systematically add electrochemical reactions to the RCE CFD model in a way that allows for each simulation improvement to be experimentally verified until a model is created that can accurately predict the performance of CO_2 reduction in the RCE.

Chapter 4

Computation fluid dynamics simulation of the hydrogen evolution reaction in the RCE: Evaluating the effects of electrochemical reactions on the local conditions at the electrode surface

4.1 Introduction

The Hydrogen Evolution Reaction (HER) is an electrochemical reaction that is ubiquitous with aqueous electrochemistry. This reaction proceeds through a multi-step mechanism beginning with the absorption of a proton on the surface of the catalyst at an available active site, along with the transfer of an electron. This step is called the Volmer step, and in acidic media is facilitated by the hydronium cation (H_3O^+). In basic media, the proton is sourced from molecular water. The following step involves two possible mechanisms. In the Tafel reaction, two adsorbed hydrogen

atoms combine on the surface of the catalyst and desorb as molecular hydrogen. In the Heyrovsky step, a second hydronium ion releases a proton to combine with the absorbed hydrogen atom from the Volmer step while a second electron is transferred to the catalyst [148]. While selectivity for HER through molecular water (Eq. 4.1) or hydronium cations (Eq. 4.2) is related to the pH of the solution, it should be recognized that the pH of relevance is that of the fluid in the region close to the catalyst surface [149]. In other words, the selectivity is dependent on the concentration of hydronium ions at the electrode surface.

$$2H_2O + 2e^- \rightleftharpoons 2OH^- + H_2 \tag{4.1}$$

$$2H_3O^+ + 2e^- \rightleftharpoons 2H_2O + H_2 \tag{4.2}$$

This effect is obvious upon comparison of the polarization curves for water at different levels of acidity when the mass transport rates are controlled by rotating the working electrode in a rotating cylinder electrode (RCE) or rotating disk (RDE) reactor as shown in Fig. 4.1. Under more basic conditions (pH=5.23) reduction of water is dominant due to a low concentration of hydronium ion (heretofore referred to as protons) in the solution. The polarization curve for this condition is shown in black. However, when acid is added resulting in pH=3.79, contributions from proton reduction can be observed starting a potential of about -0.4 V vs. SHE (red curve). the dependency of this reaction is clearly seen in the mass transfer limiting current behavior indicated by the plateau before converging with the water reduction curve. This plateau indicates that at potentials more negative than the start of the plateau, the driving force for the reaction is great enough that the region near the surface of the electrode is depleted of protons and the reaction rate is limited by the rate of protons diffusing to the surface of the catalyst. The current density at which this plateau is observed is called the limiting current density (j_{lim}). This value can be easily manipulated by controlling the rotation speed of the RDE or RCE. Increasing rotation speed results in increased mass transport and j_{lim}. This suggests that the conditions at the surface of the electrode are very

different than in the bulk. In general, HER results in pH at the electrode surface that is higher than the bulk pH. This is caused by both the depletion of H^+ at the electrode surface in Eq. 4.2 and generation of OH^- from Eq. 4.1. The water dissociation reaction also plays a role in balancing the concentration of H^+ and OH^- at the electrode surface working to further reduce the proton concentration at the electrode surface as excess OH^- is produced from water reduction. This effect can be seen clearly when the individual contribution of proton reduction to HER is extracted from the polarization curves by subtracting the high pH curve from the low pH curve (subtracting black from red). The resulting curves in Fig. 4.1 (c) and (d) are shown in red. While the behavior is distorted for the RCE, the RCE curve clearly shows that the proton reduction contribution peaks, then rapidly decreases as the water reduction reaction becomes dominant at high potentials.

The situation becomes more complicated when a buffer (KH_2PO_4) is added to the solution. The polarization curve for this case is shown in blue. While the current density due to proton reduction at low potential is still present it is slightly decreased, and an additional contribution added by the buffer addition can be seen before water reduction takes over. Subtracting the polarization curve for high pH allows the contribution of the buffer to be clearly seen in addition to the proton reduction contributions. The mechanism for this additional contribution is not entirely understood although it may be due to the buffer adjusting the local pH at the surface of the electrode or participating in the electrochemical reactions as a proton donor depending on the system being investigated [150]. For example, in electrochemical CO_2 reduction Resasco and co-workers have reported that the production of H_2 and CH_4 is affected by the addition of buffer and that the effect is dependent on the concentration and composition of the buffer anion [29]. However, the influence of buffers on electrochemical reaction like CO_2 reduction require further investigation to fully comprehend. Being able to model the HER along with buffer effects will clearly be necessary to develop a fully parameterized simulation of electrochemical CO_2 reduction in the RCE. Additionally well parameterized multi-scale modeling of these reactions, paired with high fidelity experimental data can provide insights about the local environment at the electrode surface enabling a more compre-

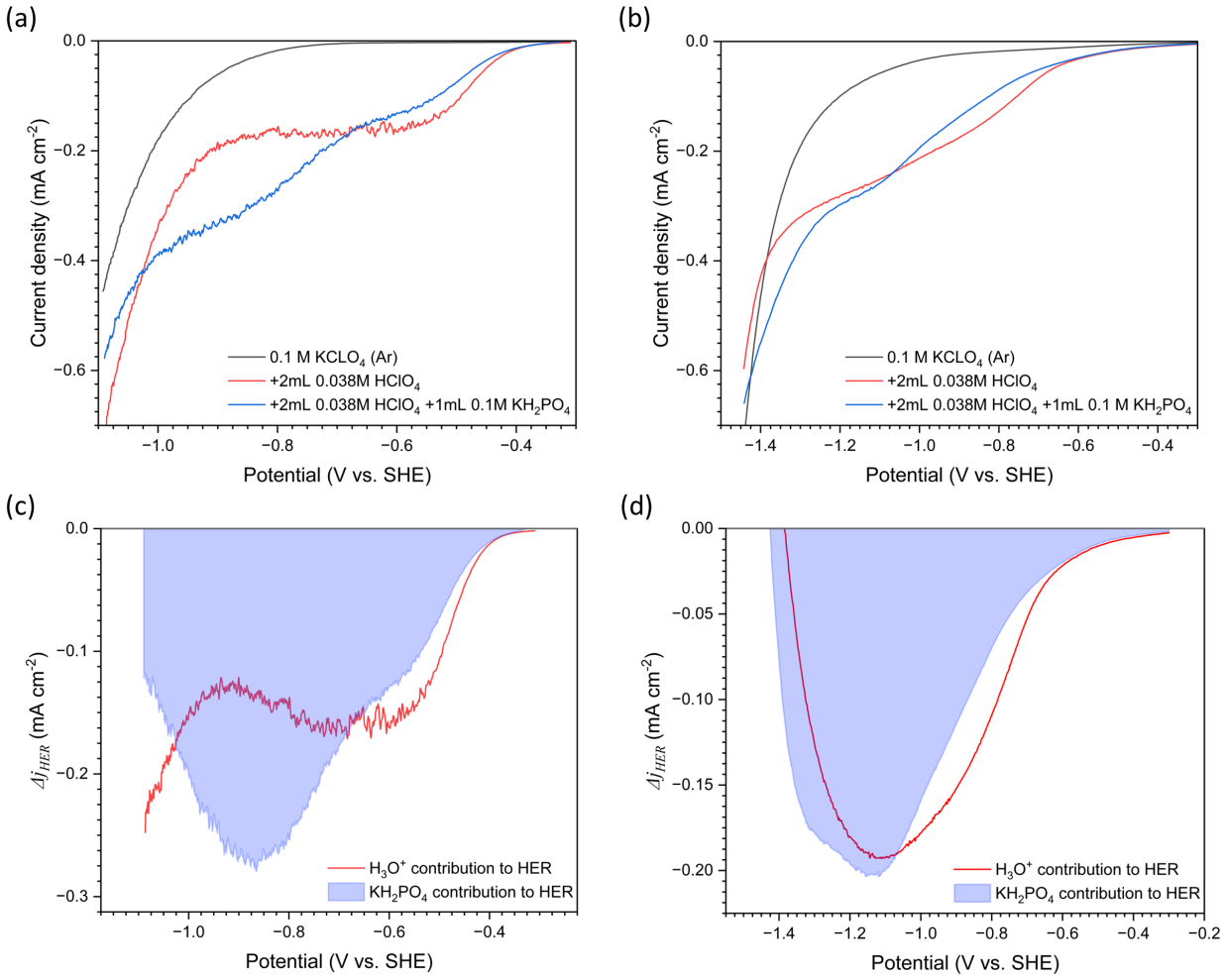

Figure 4.1: Experimental data showing the effects of acid and buffer on the polarization curve for HER. (a) Polarization curves for experiments using the RCE. (b) Polarization curves for experiments in the RDE. (c) The contribution to HER when acid an buffer are added to solution in the RCE. Curves are obtained by subtracting the polarization curve when water reduction is dominant. (c) The contribution to HER when acid an buffer are added to solution in the RDE.

hensive understanding of how to control selectivity and reactivity for complex reactions like CO_2 reduction.

However, developing accurate simulation techniques must be done systematically to ensure simulation accuracy. First the hydrodynamics of the experimental RCE were modeled using a ferricyanide as an experimental probe of the boundary layer behavior [5]. This is the simplest scenario that can be measured experimentally. Ferricyanide reduction is a simple one step electron transfer reaction. This data was used to validate the results of the CFD simulations before adding more complex interactions. In this study we report our efforts in the next development stage of this reactor simulation: the addition of the hydrogen evolution reaction (HER) and buffer equilibrium reactions. This step has proven to be challenging due to software limitations, but useful information can still be extracted from the current stage of the simulation efforts. As such, details of the challenges faced when modeling HER in Ansys Fluent will be discussed along with the results of the simulations and experiments that the simulations attempt to replicate.

4.2 Experimental methods

All experiments were conducted using an RDE or RCE with identical equipment and chemicals. A single compartment glass cell was filled with 100 mL of 0.1 M $KClO_4$ (99.99% trace metals basis, Sigma-Aldrich). The counter electrode (Pt wire) was placed along with a small amount of the electrolyte in a glass tube with a glass frit at the end and submerged in the electrolyte along with a Ag/AgCl reference electrode. Titanium working electrodes polished to a mirror finish with 0.5 μm alumina dispersion were used for both the RDE and RCE. UHP Ar was bubbled through the solution to remove dissolved oxygen and maintain an inert atmosphere during the experiments. A Metrohm PGSTAT302N was used for all electrochemical experiments along with a modulated speed rotator from Pine Instruments to control the rotating speed of the RCE and RDE. All experiments were conducted at a rotation speed of 400 rotations per minute (RPM) and cyclic voltamo-

grams were performed with a scan rate of 10 mV s^{-1}. Initial measurements were taken in the 0.1 M $KClO_4$ solution with a measured pH of 5.23. 2 mL of 0.038 M $HClO_4$ (Optima, Fisher Scientific) was added to the electrolyte resulting in a measure pH of 3.79 for proton reduction experiments. Acidic measurements was followed by 1 mL of 0.1M KH_2PO_4 (99.99% trace metals basis, Sigma-Aldrich)

4.3 Simulation methods

Simulations were performed using Ansys Fluent 2022R2 software running on the Hoffman2 Shared Cluster provided by UCLA Institute for Digital Research and Education's Research Technology Group using a 48-core dual processor with 512 GB of RAM. Identical methods were used to model the hydrodynamics as detailed in Richard et. al. [5]. Geometry and mesh were modified to use electrochemistry models as follows:

- The real reactor geometry was used instead of the simplified geometry.
- The geometry was reduced to only the parts that contained liquid (ie. the headspace was removed from the geometry).
- A counter electrode surface was defined as shown in Fig. 4.2
- A structured boundary layer mesh was added in the electrolyte region at the counter electrode surface to capture gradients in concentration at this interface (Fig. 4.2).

The quality of the mesh used in this study is considered *excellent* by Ansys standards [128] with a cell count of 1,290,631. Details of the relevant quality measurements are outlined in Table 4.1. Boundary conditions for the hydrodynamics were specified to have zero slip conditions at all fluid wall interfaces except the top surface where the liquid would be in contact with the gas phase. Since the gas phase was removed for this study, a zero shear boundary condition was set at this interface

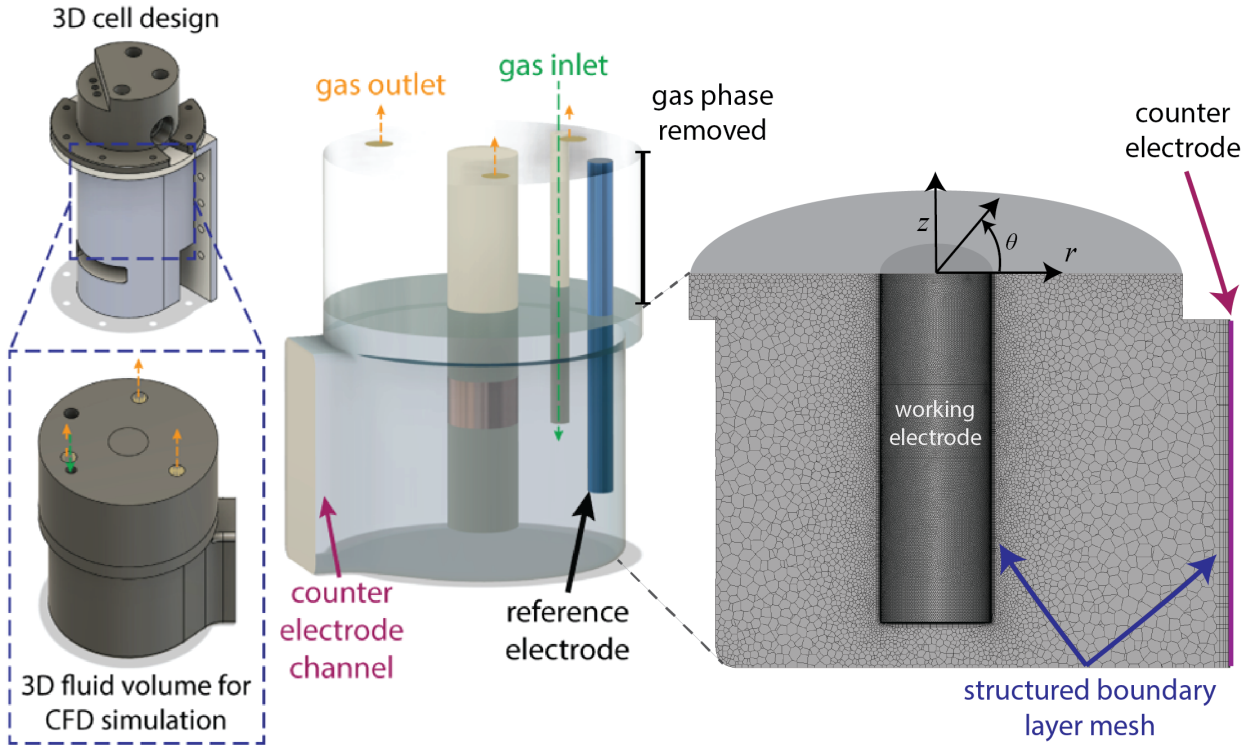

Figure 4.2: Three dimensional renderings of the RCE reactor geometry showing the region that was used for simulation and the mesh generated for the liquid region investigated in this study. Adapted [86], Copyright 2022, with permission from Elsevier.

to approximate the interactions between the liquid and the gas surfaces. The surface of the rotating shaft was set to have an angular velocity ω=41.89 Rad s^{-1} or 400 RPM. For the electrochemistry, boundary conditions of 0 mA cm^{-2} were specified on all non-electroactive surfaces. The counter electrode (oxidizing reactions) was specified to have a constant potential of 0 V while the potential of the working electrode was set according to the condition of interest at a negative value for reduction reactions. During simulation startup it was found that an initial boundary condition on the working electrode of -1 μA cm^{-2} was required to solve the initial potential field. The first ten time steps (step size = 0.1 ms) were solved under this constant current boundary condition on the working electrode, while the potential boundary condition was specified for all remaining time steps. After establishing the potential field at constant current, the surface potential of the working electrode was computed and used as the starting point for the electric potential boundary condition

	Orthogonal Quality	Squish	Aspect Ratio
Maximum	0.200	0.800	300.063
Average	0.980	0.020	16.761

Table 4.1: Quality Metrics for the mesh used in this work.

on the surface of the working electrode. Ramping the electric potential boundary condition on the working electrode was necessary to ensure convergence, as the solution for the electric field when coupled with electrochemical reactions becomes highly nonlinear and difficult to solve if the change is too large between time steps. potential ramp rates less than 5 V s^{-1} were found to be adequate for convergence under most conditions. The electric potential package along with electrochemical reactions were enabled in Fluent to simulate the electric field (Eq. 4.3), charge conservation (Eq. 4.4), and Butler-Volmer kinetics (Eq. 4.5).

$$\nabla \cdot (\sigma \nabla \phi) = 0 \tag{4.3}$$

$$\nabla \cdot \mathbf{j} = 0 \tag{4.4}$$

$$j_{F,r} = j_{o,r} \prod_{i=1}^{N} \left(\frac{Y_{i,r}}{Y_{\text{i,r}}^{\text{ref}}} \right)^{\gamma_{i,r}} \left[\exp\left(\frac{\alpha_{a,r} F \eta_r}{RT} \right) - \exp\left(\frac{-\alpha_{c,r} F \eta_r}{RT} \right) \right] \tag{4.5}$$

Here, σ is the conductivity of the electrolyte (1.1514 S m^{-1} for 0.1 M $KClO_4$ [137]), ϕ is the electric potential, *j* is the current density vector, the subscript i is a given species, while r is the reaction of interest, $j_{F,r}$ is the Faradaic current density, $j_{o,r}$ is the exchange current density, N is the total number of chemical species, Y is the species mass fraction, Y^{ref} is the species' reference mass fraction, γ is the order of reaction, α_a and α_c are the anodic and cathodic charge transfer coefficients, F is Faraday's constant, R is the universal gas constant, T is the Temperature, and η is the overpotential. For these simulations, the overpotential is defined as:

$$\eta_r = \phi_{ed} - \phi_{el} - E_{eq,r} \tag{4.6}$$

	Electrochemical Reaction	α_a	α_c	i_o (A m^{-2})	Species	Diffusion Coefficient ($\times 10^{-9}$ m^2 s^{-1})
1.	$2H^+ + 2e^- \rightleftharpoons H_2$	0.39	0.61	5.5×10^{-8}	H_2	4.580
2.	$2H_2O + 2e^- \rightleftharpoons 2OH^- + H_2$	0.72	0.28	1.23×10^{-6}	H^+	9.311
3.	$4OH^- \rightleftharpoons 2H_2O + O_2 + 4e^-$	1	0	10	OH^-	5.273
4.	$2H_2O \rightleftharpoons 4H^+ + O_2 + 4e^-$	1	0	10	O_2	2.010
	Homogeneous Reaction	k_f (s^{-1})	k_b (M^{-1} s^{-1})			
5.	$H_2O \rightleftharpoons H^+ + OH^-$	2.4×10^{-5}	1.5×10^{11}			

Table 4.2: Charge transfer coefficients, exchange current density, rate constants, and diffusion coefficients used in work simulation for each reaction and species.

where ϕ_{ed} is the potential on the surface of the electrode (the boundary condition), ϕ_{el} is the potential of the electrolyte immediately adjacent to the electrode surface, and $E_{eq,r}$ is the equilibrium potential of the reaction. $\alpha_{a,r}$, $\alpha_{c,r}$, and j_o for reaction 1 and 2 (working electrode) where derived from fits of experimental data where $E_{eq,r}$ was set to be 0 vs the standard hydrogen electrode for both reactions. For reactions 3 and 4 (counter electrode) α and j_o where chosen to provide fast enough kinetics as to have an insignificant effect on the potential field. All electrochemical reactions were specified to be first order with respect to the concentration of the reacting species. The homogeneous water dissociation reaction (reaction 5) was also considered in the bulk liquid. Forward and backward reaction rates were defined according to Eq. 4.7 and Eq. 4.8.

$$r_f = [H_2O]\, k_f \tag{4.7}$$

$$r_b = \left[H^+\right] \left[OH^-\right] k_b \tag{4.8}$$

Here, $[i]$ are the concentrations of species i, and k_f and k_b are the forward and backward rate constants respectively [151]. The total Faradaic current density (j) at the electrode surface is taken to be the sum of the current densities ($j_{F,r}$) for the reactions taking place on that surface. Migration is assumed to be insignificant due to the high concentration of supporting electrolyte and was not con-

sidered in this model. However, multi-component diffusion was included. Diffusion coefficients of each species in water were sourced from the CRC Handbook of Chemistry and Physics [137], and are provided in Table 4.2. Heat of reaction and joule heating were also no considered due to the low current density and high conductivity of the electrolyte under the conditions investigated. A constant temperature of 293.15 ^{o}C was specified throughout the reactor.

4.4 Simulation challenges

Attempts to simulate electrochemical reactions in Fluent, have faced many challenges with the software. Initial efforts were stalled by lack of clear information about how the electrochemical packages work in Fluent. In previous simulations where Ferricyanide was reacted on the working electrode surface to evaluate the hydrodynamics, only the working electrode surface needed to be defined. However, the electrochemistry package required the definition of a separate counter electrode and simulation of the oxidation reactions to balance the reduction reactions of interest on the working electrode. This required reworking of the geometry file and re-meshing to account for this additional surface region. Additionally, lack of detailed manuals or previous publication demonstrating aqueous electrochemistry simulations with Fluent, made it unclear about how some boundary and material conditions should be defined in the system.

First was the definition of the potential and current boundary conditions. While in hindsight it seems obvious that the boundary condition of potential or current should be specified as a negative value to specify a cathodic reaction, this was not made clear by the manual. Additionally, the Fluent theory manual suggests that the conductivity of the solution is calculated from the concentration of ionic species in the fluid region that is defined as the electrolyte. We found that this was only the case for specific electrochemical packages specializing in modeling of batteries and fuel cells. For the case of the simulations discussed here, where only the electric potential and electrochemical reaction packages were active, the electrolyte conductivity was instead specified as a material

property and did not require the specification of supporting ions as separate species in the liquid phase. It is unclear how migration would be modeled with aqueous electrochemistry in Fluent due to the need to activate irrelevant additional packages intended for specific electrochemical systems. These packages are specifically designed to simulate a subset of electrochemical systems that are not compatible with simulating aqueous electrochemistry. We also found that Fluent does not include the number of electrons transferred (n) in calculation of current density from the Butler-Volmer kinetics. As such, all kinetic parameters for the electrochemical reactions were based on fits of experimental data assuming that $n = 1$. Finally, it is worth mentioning that the temperature of the simulation could not be set globally through the *operating conditions* tab as typically done for these simulations. Instead, it was necessary to define the temperature of at least one surface to be at the desired temperature in addition to the global initial condition.

Incompatibilities were also identified between the hydrodynamics and electrochemistry package. These resulted in *phantom* velocity components. This issue was initially recognized when simulating with two phase flow. In these simulations the gas phase in the headspace was included. When simulations where run for longer than a few seconds, it became obvious that the simulation was not behaving as it had when only the hydrodynamics were simulated. In the liquid phase, the fluid could be seen to accelerate in the Axial direction toward the base of the reactor ($-z$) reaching velocities greater than 1 m s^{-1}. In the gas phase a $+z$ velocity component would be generated. Additionally, the liquid level of the electrolyte would fluctuate erratically and eventually lead to divergence if the liquid level fell below that of the working electrode. A contour plot of the z component of the velocity vector is provided for reference in Fig. 4.3. The velocity is seen to be directed in the $-z$ direction for blue regions and $+z$ for red regions. Other components of the velocity vector are negligible in comparison to the z component. As the liquid level could not be maintained it is likely that there is an incompatibility between the conservation equations and the electric potential package when simulating with multiphase. It should be noted that this behavior was observed when the electrochemical reactions were disabled, suggesting that the electric

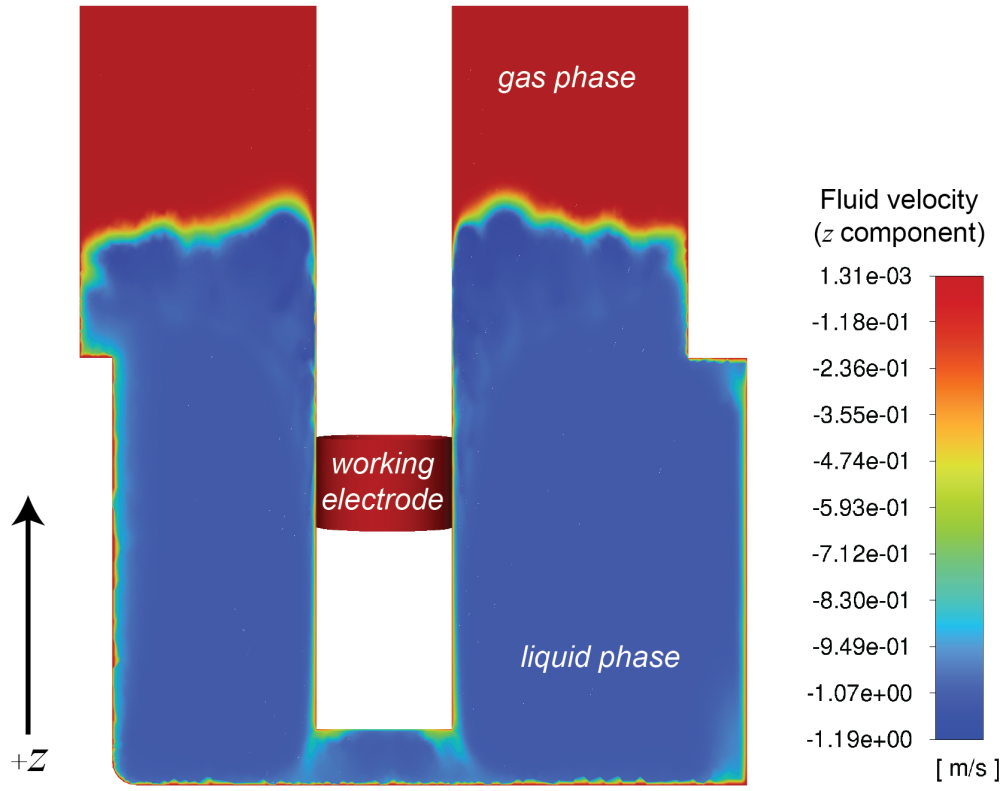

Figure 4.3: Velocity contour of the z component in a multiphase simulation with electric potential package enabled. Unexpected, large $-z$ velocity is seen in the liquid region which is primarily contained in the blue region. Additionally, the liquid level is above the initialization level although there are no inlets or outlets specified in simulation.

potential package is the source of the error. To avoid this problem, the simulation was simplified to a single phase and only the electrolyte region was modeled. It was recently discovered that a phantom velocity component directed radially, $(+r)$ is also generated in the single phase models. However, these velocities are much smaller in magnitude and seem to have little effect on short simulations beyond distorting the velocity contours.

After changing to a single phase simulation, electrochemical reactions could be simulated without convergence issues as long as only one reaction reached significant current densities. This water reduction was successfully simulated on the working electrode without including the proton reduction reaction. The simulation results for this kinetically limited reaction were in excellent agreement with the experimental data. Successful simulations were also performed when the pro-

ton reduction reaction was active and the conditions in the reactor represented neutral pH. Under these conditions the contribution of proton reduction to the total current was negligible. However, when simulations were attempted at a pH of 4, the proton reduction reaction represented a significant portion of the total current. Under these conditions the proton reduction reaction reaches a mass transfer limited current density of approx. -0.1 mA cm^{-2} and -0.85 V vs. SHE. For all simulations where proton reduction was included at low pH, the simulation was unable to converge at potentials more negative than approx. -0.95 V vs. SHE. This point coincides with the region where the second electrochemical reduction reaction (the reduction of molecular water) starts to reach significant current densities. This suggests that Fluent has difficulty in solving the highly non-linear equations resulting from the multiple electrochemical reactions interacting with the potential field and current density calculations on the electrode surface. While one reaction is dominant, the simulation can find a solution since the other has little influence on the solution. However, when multiple reactions are influencing the potential and current density fields, it becomes difficult to converge on a single solution. This problem has been recognized elsewhere and can be addressed by linearizing the equations describing current density [152]. Fluent does not appear to have this capability built into the software, although limited information exists detailing the methods that Fluent uses to solve the system of equations for the electrochemical packages used in this study.

While many of these issues will need to be addressed to build a complete simulation of buffer reactions in the RCE, some useful information can be extracted from the simulation results already generated. The following section will highlight results from simulations without proton reduction where the simulation was able to reach current densities of up to 1 mA cm^{-2}. Additionally, mass transport limited conditions where proton reduction is dominant will be compared with simulations where water reduction is dominant to evaluate the difference between mass transport and kinetically limited reaction conditions at the surface of the working electrode. These cases represent conditions where the simulation is able to reliably find the solution, and will provide insights about the local conditions at the electrode surface.

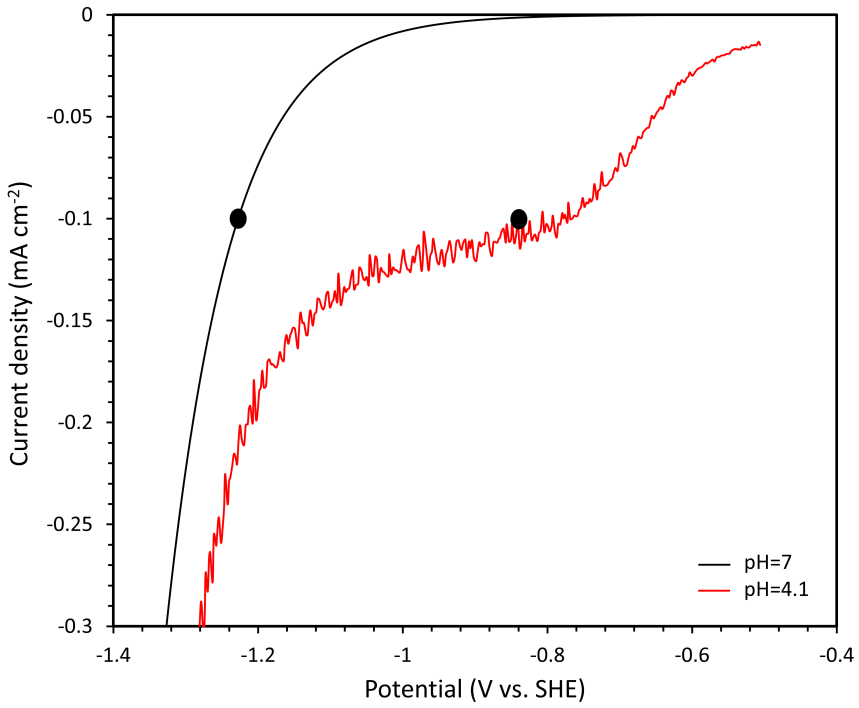

Figure 4.4: experimental polarization curves for HER at neutral pH and acid pH showing the two points where simulation results at each condition where taken for comparison.

4.5 Simulation results and discussion

In experimental electrochemistry, the fact than what we measure experimentally is bulk values is often ignored. In reality, the local conditions on the surface of the electrode can vary significantly depending on many factors including conductivity of the electrolyte, reactor geometry, the kinetics of the reaction, and mass transport conditions. To estimate the local conditions in a reactor, mathematical models and simulations have previously been used to evaluate the suitability of various reactor geometries. While the gastight RCE provides uniform hydrodynamics for large surface areas due to it's symmetry, the electric field is not symmetric due to the counter electrode being located only on one side of the working electrode. How does this affect the conditions on the electrode surface and are the average values that we measure experimentally representative of the conditions at the electrode surface?

To answer these questions, the following discussion will focus primarily on three sets of sim-

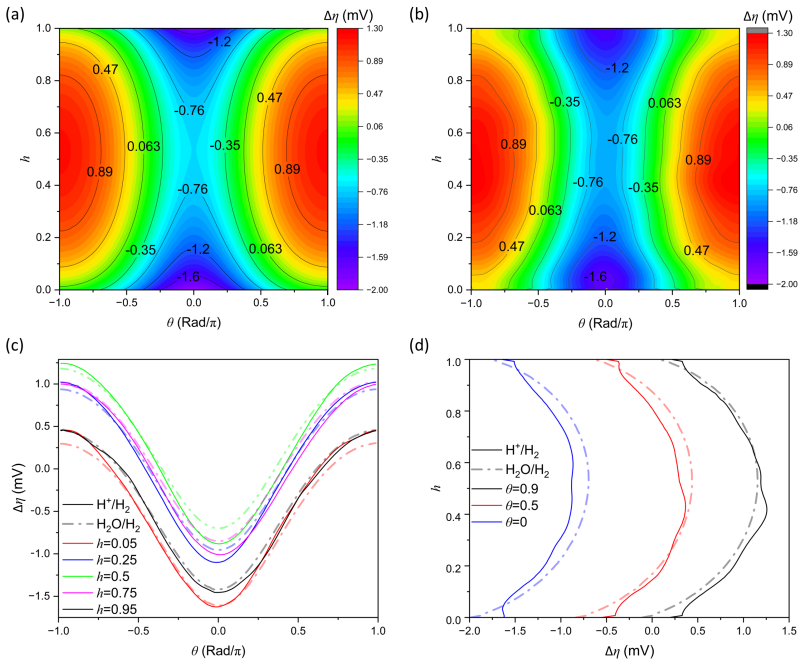

Figure 4.5: Contours and line profiles for $\Delta\eta$ showing the variation in overpotential across the cylindrical working electrode surface . (a) $\Delta\eta$ for kinetically limited conditions where HER is primarily from molecular water. (b) $\Delta\eta$ for mass transfer limited conditions where HER is primarily from proton reduction. (c) Azimuthal line profiles of $\Delta\eta$ taken from (a) (dashed line) and (b) (solid line) at various values of h. (d) Axial Line profiles of $\Delta\eta$ at various values of θ.

ulated conditions in the RCE for HER. The first condition is that of kinetically limited reaction conditions on the surface of the working electrode. This condition represents a case where the fluid is basic enough that proton reduction is negligible and nearly all of the current density can be attributed to water reduction. The second condition is under acidic conditions where pH=4. Under this conditions at a rotation speed of 400rpm, proton reduction reaches mass transfer limited conditions at a current density of 0.1 mA cm^{-2}. We will begin with a comparison between these two conditions (kinetically and mass transfer controlled) when both are at a current density of 0.1 mA cm^{-2}. These two points are shown as black circles in reference to the experimental data they are based on in Fig. 4.4. The last set of conditions will evaluate how the potential field on the electrode changes for a kinetically limited reaction as a function of current density between 0.001 and 1 mA cm^{-2}.

We will begin by examining the potential field across the working electrode surface. Fig. 4.5 (a) provides a two-dimensional contour of the variation in overpotential under kinetically limited conditions at 1 mA cm^{-2}. Fig. 4.5 (b) shows the same contour under mass transfer limited condition (also at 1 mA cm^{-2}). Variation in overpotential ($\Delta\eta$) is defined to be the difference between the local overpotential ($\eta_{(\theta,h)}$) measured on the surface of the electrode and the area-average overpotential (η_{ave}). Here h is defined to be axial distance along the electrode in the $+z$ direction normalized by the total electrode height of 0.8 cm and θ is the azimuthal angle (in Rad/π) relative to the counter electrode, where $\theta = 0$ is the side of the working electrode facing the counter electrode and -1 and +1 correspond to the opposite side of the working electrode cylinder. Visual inspection suggests similar contours for both conditions with the most negative overpotentials being located at $\theta = 0$ and the smallest overpotentials corresponding to the opposite side of the working electrode. Azimuthal line profiles at various values of h (Fig. 4.5 (c)) and vertical line profiles at values of θ (Fig. 4.5 (d)) help to visualize how the geometry of the system influences the potential field on the surface of the electrode.

Due to the cylindrical shape of the working electrode, and the position of the counter electrode on one side, the azimuthal profile of the potential potential shows a sinusoidal shape on the cylindrical working electrode. This profile is to be expected due to the circular nature of the geometry. While the variation in overpotential is small for the conditions examined here, it should be recognized that since the electrode is rotating, assuming a non slip boundary condition, this profile can be paired with the electrode's frequency of rotation to describe the changing overpotential that a species at the surface of the electrode will experience as a function of time. In Fig. 4.5 (d) a parabolic profile can be seem in the axial plane of the electrode surface. This is caused by the edge effects of the electrode where they are in contact with the insulating electrode shaft. It is well known in the theory of electrochemistry that the edge of an electrode that is in contact with an insulator at an angle of 180^{o} will have the smallest Ohmic resistance at this interface due to the larger number of paths that ions can take to the surface [112, 153]. On the other hand, the middle

of the electrode will have the highest resistance, since ions can only move perpendicular to the working electrode surface. As such, the general parabolic shape of the axial profile is also to be expected. In both cases (kinetically and mass transfer limited), we see that the line profiles and contours are similar in shape and scale.

Slight fluctuations in potential are observed for the mass transfer limited case (H^+/H_2). These fluctuations are primarily due to variations in current density across the surface of the electrode as shown in Fig. 4.6 (a) where the local current density (j) is shown normalized by the average current density (j_{lim}). These fluctuations in j/j_{lim} are subsequently caused by variations in concentration which in turn are governed by the hydrodynamics. In Fig. 4.6 (b) the local concentration of protons (C_{H^+}) is normalized by the bulk concentration ($C_{H^+,bulk}$) to better visualize the variation across the surface. Comparison of Fig. 4.6 (a) and (b) reveals a clear correlation between the concentration and current density due to the mass transfer limited conditions. Near the center of the electrode, the current density is near the average value and the concentration of protons is very low. At the edges however, the concentration of protons is much closer to bulk values since diffusion can also occur axially, while in the center of the electrode diffusion can only occur radially. However, this edge effect has little impact on j_{lim}. Evidence for this is provided by Fig. 4.6 (c) and (d) which show that the majority of the electrode surface has a current density close to the average. Overall, the variation in j is seen to be within 25% of j_{lim}. An additional point worth noting is that the current density for the kinetically limited case shows insignificant variation from j_{lim}. Comparing to theory for primary, secondary, and tertiary current density distributions on electrodes, we find that under the conditions studied here, we see almost perfect representations of reactions where the secondary and tertiary current density are dominant. While the primary current density for this electrode would be expected to show a similar profile to that of the mass transfer limited case (tertiary current density) it would not show the fluctuations due to variation in proton concentration. Additionally since the water reduction case shows only slight variation across the electrode surface, we can conclude that the primary current density is insignificant in comparison to the secondary

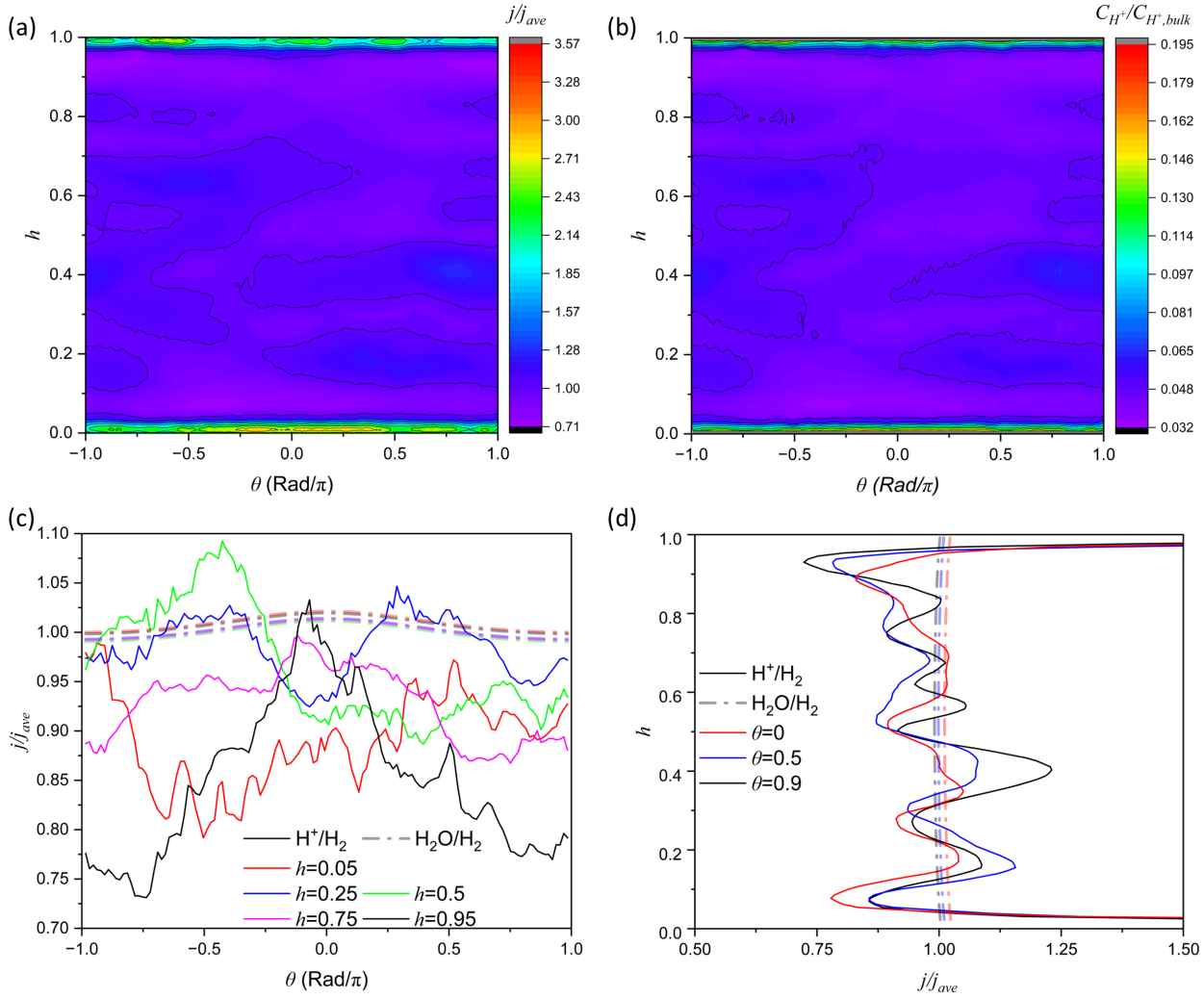

Figure 4.6: Contours and line profiles for j/j_{ave} showing the variation in current density across the cylindrical working electrode surface . (a) A contour of j/j_{ave} for mass transfer limited conditions where HER is primarily from proton reduction. (b) a contour of the concentration of H^+ normalized to the bulk concentration. Comparison with (a) shown the dependency of j on the local concentration of H^+ . (c) Azimuthal line profiles of j/j_{ave} under kinetically limited (dashed line) and mass transfer limited (solid line) conditions at various heights of the electrode surface. (d) Axial Line profiles of j/j_{ave} at various values of θ on the surface of the electrode.

and tertiary current densities. In other word, under the conditions studied here, Ohmic losses have an insignificant effect on the current density distribution. However, it should be noted that the Ohmic losses *are* primarily responsible for the potential profile on the electrode surface as evidenced by the minimal impact of current density fluctuations on the potential field.

While this may be hold true for low current densities, at higher current densities, the Ohmic losses are made more significant and the kinetics of HER from water reduction become much faster. This leads to a higher amplitude of the sinusoidal and parabolic potential profiles on the electrode surface (Fig. 4.7). Here we can see that increasing the potential an order of magnitude to 1 mA cm^{-2} increases the variation in overpotential to 15 mV. Plotting the amplitude for $\Delta\eta$ as a function of the current density shows a near linear trend with the amplitude increasing almost an order of magnitude for every order of magnitude change in j_{ave}. Once simulations capable of simulating above 1 mA cm^{-2} are developed, higher current densities should be investigated to further evaluate the variations on the surface of the electrode. Furthermore, to improve the local conditions at the working electrode, a more symmetric counter electrode configuration could be devised to reduce variations in the potential profile.

4.6 Conclusions

In conclusion, this study highlights recent progress in our efforts to develop continuum level CFD simulations of complex electrochemical reactions in the gastight RCE reactor. This stage of development involved the simulation of HER which it ubiquitous in aqueous electrochemistry. Because this reaction will be present as a competing reaction in any simulation involving aqueous electrochemistry, HER is the obvious next step in adding complexity to the existing model of the reactor hydrodynamics. Additionally, motivation for the inclusion of buffer reactions is provided, as these reactions are common in electrochemical systems like CO_2 reduction and are known to affect the HER reaction. Thus far, conditions where only one electrochemical reaction is dominant

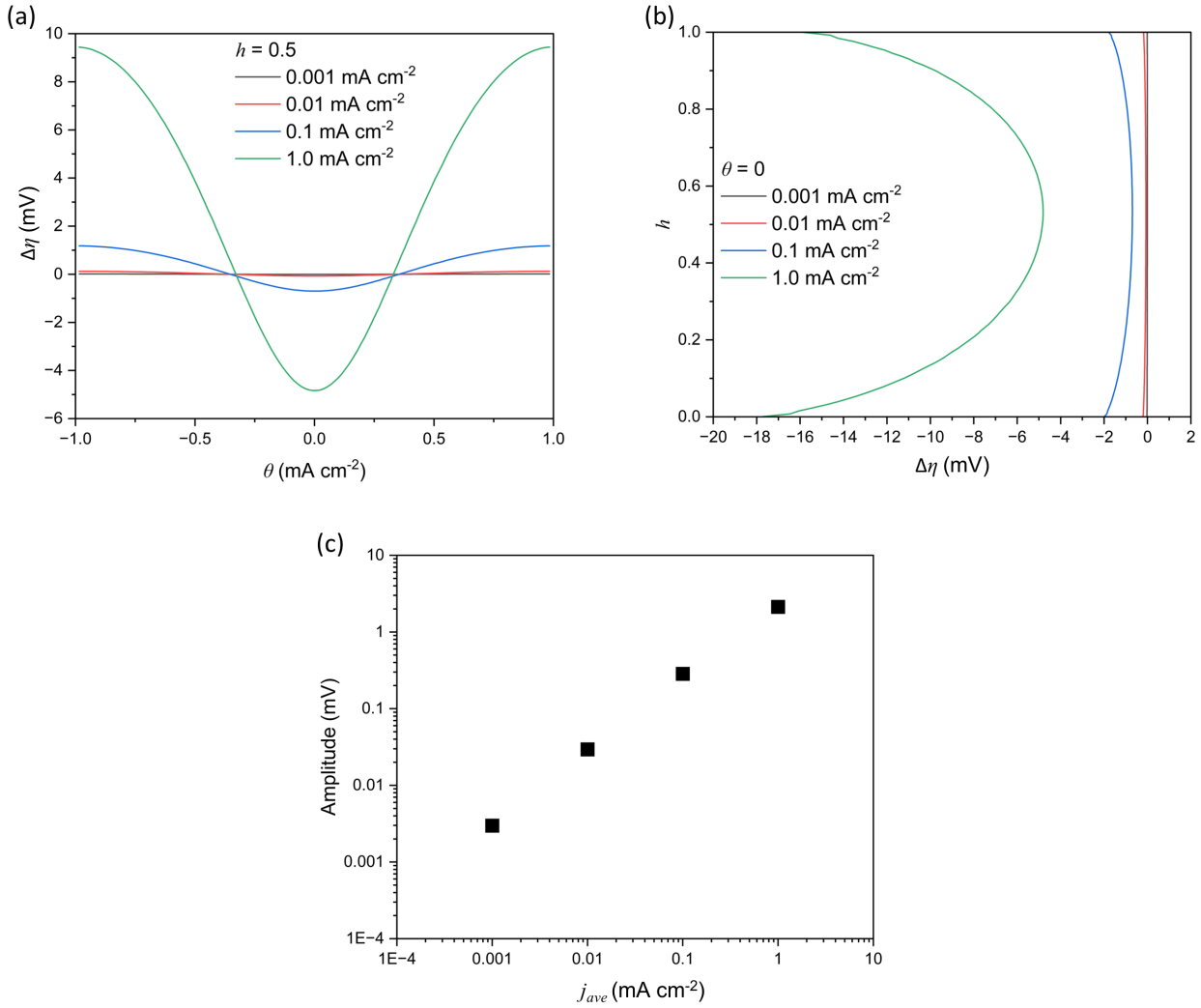

Figure 4.7: Line profiles taken at $\theta = 0$ and $h = 0.5$ showing how $\Delta\eta$ changes for j_{ave} between 0.001 and 1 mA cm^{-2}. (a) Azimuthal line profiles of $\Delta\eta$ (b) Axial line profiles of $\Delta\eta$. (c) Amplitude of $\Delta\eta$ as a function of j_{ave} showing a near linear relationship.

have been modeled successfully due to difficulties with the Ansys Fluent modeling software. As such, details of the key simulation issues are discussed along with possible sources and solutions that have been identified to overcome these issues.

Simulation results from successful simulations of HER from molecular water and protons respectively provide insights about the local conditions at the electrode surface under kinetically limited current densities and under mass transport limited current densities. We find that Ohmic losses due to resistance of the electrolyte produce a sinusoidal potential profile in the azimuthal direction and a parabolic axial profile with the most negative overpotentials observed at h=0 and 1 at $\theta = 0$. A slight variation in this potential field is observed for the mass transfer limited case due to variations in the current density cause by turbulence induced H_+ concentration fluctuations. The magnitude of the variations in overpotential is seen to increase almost linearly with increasing j_{lim}. At 0.1 mA cm^{-2} the current density profiles agree with the ideal secondary current density distribution under kinetically limited water reduction, and the ideal tertiary current density distribution under mass transport limited conditions. As such, Ohmic losses have an insignificant effect on the current density profile at this current density. Since the magnitude of the potential variation increases with current density, the assumption of negligible Ohmic effects on j should be reevaluated when considering reactions with faster kinetics and mass transport at high current density. Finally, the effect of the counter electrode being located on only one side of the working electrode is found to be negligible for low current density conditions and average values measured experimentally can be considered representative of the local conditions at the electrode surface for kinetically limited reactions, while the local current density is seen to vary (on average) within 25% of j_{lim} for mass transfer limited reactions under turbulent flow at 400 RPM.

Chapter 5

Recent advances in the electrochemical production of chemicals from methane

Methane, the primary component of natural gas, is broadly used as raw material for production of base chemicals such as hydrogen, syngas, methanol, and ammonia. Natural gas is projected to continue to be an energy and feedstock staple for the chemical manufacturing industry [154], and although its continued use offers a significant global competitive advantage, the associated greenhouse gas (GHG) emissions can have a major impact on the climate and environment [155]. The global chemical and petrochemical subsector is responsible for over 1.2 Gt of CO_2 emitted every year [122]. Replacing fossil resources with synthetic fuels and sustainably produced chemicals would, in theory [156], allow us to close the carbon cycle and eliminate CO_2 emissions. However, our products are made up of 50% carbon and are not degraded or consumed at the instantaneous rates required to sustain a truly closed feedstock-product-feedstock carbon cycle [157, 158]. A carbon-free chemical industry is simply not possible until inexpensive and scalable methods for direct air capture become widely available [159]. The reduction of GHG emissions from the chemical industry is still possible through the use of abundant, cheap renewable energy and a convergence of the chemical and energy markets [160]. The higher the synergy and flexibility of this conver-

gence, the less carbon-capture utilization and sequestration is needed to reduce carbon emissions and meet future zero-emission targets in this sector [161–163]. The use of renewable electricity as a source of heat for furnaces [164, 165] and the use of electrocatalytic processes [166, 167] to drive energy-intensive chemical transformations promise to (i) displace natural gas combustion as a source of heat and (ii) deliver more compact, economic, efficient, and thus more competitive chemical manufacturing units. In this review, we highlight the most recent developments in the direct transformation of methane to chemicals using electrochemistry. Emphasis is given to high-temperature electrochemical processes that use solid electrolyte membranes, where product separation and heat integration have already been integrated as part of the chemical production system. Recent ambient temperature processes for the transformation of methane to chemicals are also summarized in this review, highlighting the research and development gaps toward the scale-up of these technologies.

5.1 Current and future chemical manufacturing practices

Primary products derived from methane (Fig. 5.1) include syngas, hydrogen, ammonia, and methanol with market shares of over $47 billion, $117 billion, $54 billion, and $32 billion, respectively [168] [16]. Almost every commercial process synthesizing higher-value products from methane starts with steam methane reforming (SMR), a high-temperature and -pressure process that produces hydrogen and carbon monoxide used for synthesis of other chemicals. SMR is highly endothermic ($CH_4+H_2O=CO+3H_2$, ΔH^o_{RXN}=208.7 kJ mol^{-1}) and requires high temperatures for methane activation, where the necessary heat is provided by natural gas fired heaters. Water gas shift ($CO+H_2O=H_2+CO_2$, ΔH^o_{RXN}=-41.1 kJ mol^{-1}) is mildly exothermic and is used to further convert CO to CO_2 and increase hydrogen yield. Depending on process configuration, the hydrogen and carbon products can be used as precursors for a variety of carbon-based chemical synthesis processes or separated to use hydrogen as a fuel in transportation. Demand for hydrogen,

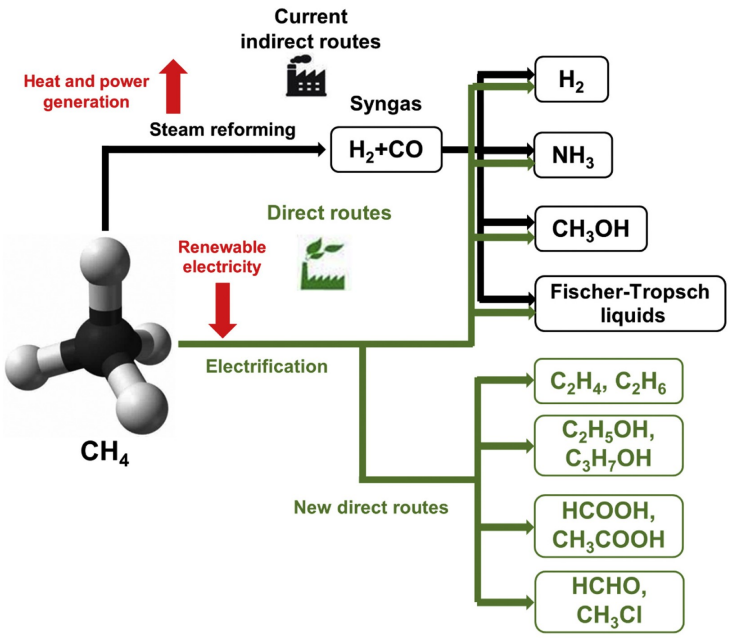

Figure 5.1: Established industrial processes of methane conversion for production of chemicals and potential alternative routes powered by renewable electricity.

methanol, ammonia, and other syngas derivatives is expected to continue to increase in the future. Thus, the development of advanced processes that efficiently activate and transform methane and that reduce GHG emissions is of paramount industrial importance [169].

Because natural gas is used as both feedstock and fuel to provide the necessary heat for reaction, development of alternative synthesis pathways that utilize renewable electricity is being pursued to reduce or eliminate GHG emissions. A first step toward electrified chemical manufacturing is to convert processes to utilize electrically driven resistive or *Joule* heating instead of combusting natural gas. Existing plants could be retrofitted to utilize electric heating, eliminating GHG emissions linked to fuel burning, increasing thermal efficiency, improving process control, and allowing them to operate under more stringent emission standards [9, 170]. For hydrogen production, elimination of combustion-derived heat would reduce carbon emission by 25-30% when utilizing renewable sources of electricity [170]. Likewise, there is an energetic advantage to making hydrogen from methane using electricity. The production of hydrogen from SMR only requires

41.9 kJ to produce a mole of hydrogen, whereas electrolysis requires 285 kJ per mole of hydrogen. Furthermore, when combined with utilization of carbon products (i.e. CO, CO_2) from SMR to produce higher-value products (such as methanol, olefins, or liquids), SMR could be made essentially emission free. Conversion of existing processes to electric heating and integrated utilization of carbon products could also allow continued use of existing chemical plants with significantly reduced emissions until replacement technologies are implemented at scale [10]. A second step toward electrified chemical manufacturing is to use electrochemistry to drive endothermic synthesis and separation processes. Although research efforts in electrochemical synthesis have increased over the last decade, it is notable that separation processes are often omitted and rarely discussed in the electrochemistry literature. This highlights a lack of a system approach to the development of these processes. The use of applied electrical potentials can be used not only to drive catalysis but also to drive separation and compression processes to directly produce hydrogen, methanol, and ammonia from methane using electrochemical cells [4, 13, 17, 168, 171]. Furthermore, electrochemistry could enable new synthetic pathways for the direct synthesis of higher-value chemicals from methane such as olefins [16], formaldehydes, and other oxygenate [172] products which are not currently available (Fig. 5.1).

5.2 Process energetics for methane activation and product synthesis and separation

Methane, due to its symmetry and lack of polarity, is a highly stable molecule that is difficult to activate. As such, the rate-limiting step is the activation of the initial C-H bond [13, 15]. Conventional catalytic processes utilize extreme temperatures to provide the energy needed to activate methane, requiring sophisticated heat integration networks and large scales to reach high overall process efficiency [173]. While heterogeneous thermal and electrochemical activation of methane occurs by identical mechanisms (dehydrogenation or deprotonation) [13], the operating conditions

in electrochemical systems can be tailored to enhance the rate of methane activation while integrating product separation and purification into the same unit.

Fig. 5.2 compares the energy flow in the production of hydrogen by thermal SMR and a thermo-electrochemical process in a high-temperature, ceramic-based protonic membrane reformer (PMR). The minimum energy required for conversion of methane to hydrogen is equal for both processes. However, the energy pathways, sources of energy loss, and GHG production are markedly different. For example, the energy source for thermochemical methane activation is the combustion of methane in the radiant section of the reformer that provides the heat for the endothermic SMR reaction. Although excess heat can be recovered from the flue gas in the convection section of the reformer, the waste heat lost in the flue gas and the irreversibility of heat transfer processes in the exchanger network limit the efficiency economically achievable through heat integration [174–176]. In electrochemical systems and electrically driven thermochemical systems, heat necessary to drive the reforming reaction can be produced by integrating resistive heating directly into the catalyst architecture. Heat is generated by electric current passing through a resistive metal in thermochemical systems or by the transport of ions through the electrolyte in electrochemical systems. The governing equation is $Q = I^2R$, where Q is the rate of energy converted to heat, I is the current of electrons or ions, and R is the resistance of the metal or electrolyte. The reduction in system size due to elimination of fired heaters allows for easier insulation and reduced thermal losses without the need for external heat integration with the reactor [4, 9, 164].

In PMRs, the electrolyte allows for selective transport of ions driven by a difference in potential across a membrane in addition to its function as a heating element. In systems with anion conductive electrolytes, oxygen anions can be selectively transported to the catalyst surface, increasing the rate of M-O active site formation [13, 177]. This can allow materials with weak oxygen binding energies to show improved reaction rates at significantly lower temperatures and pressures than thermochemical processes. However, in aqueous systems, forced M-O formation is usually limited by the competing oxygen evolution reaction occurring under conditions of high oxygen

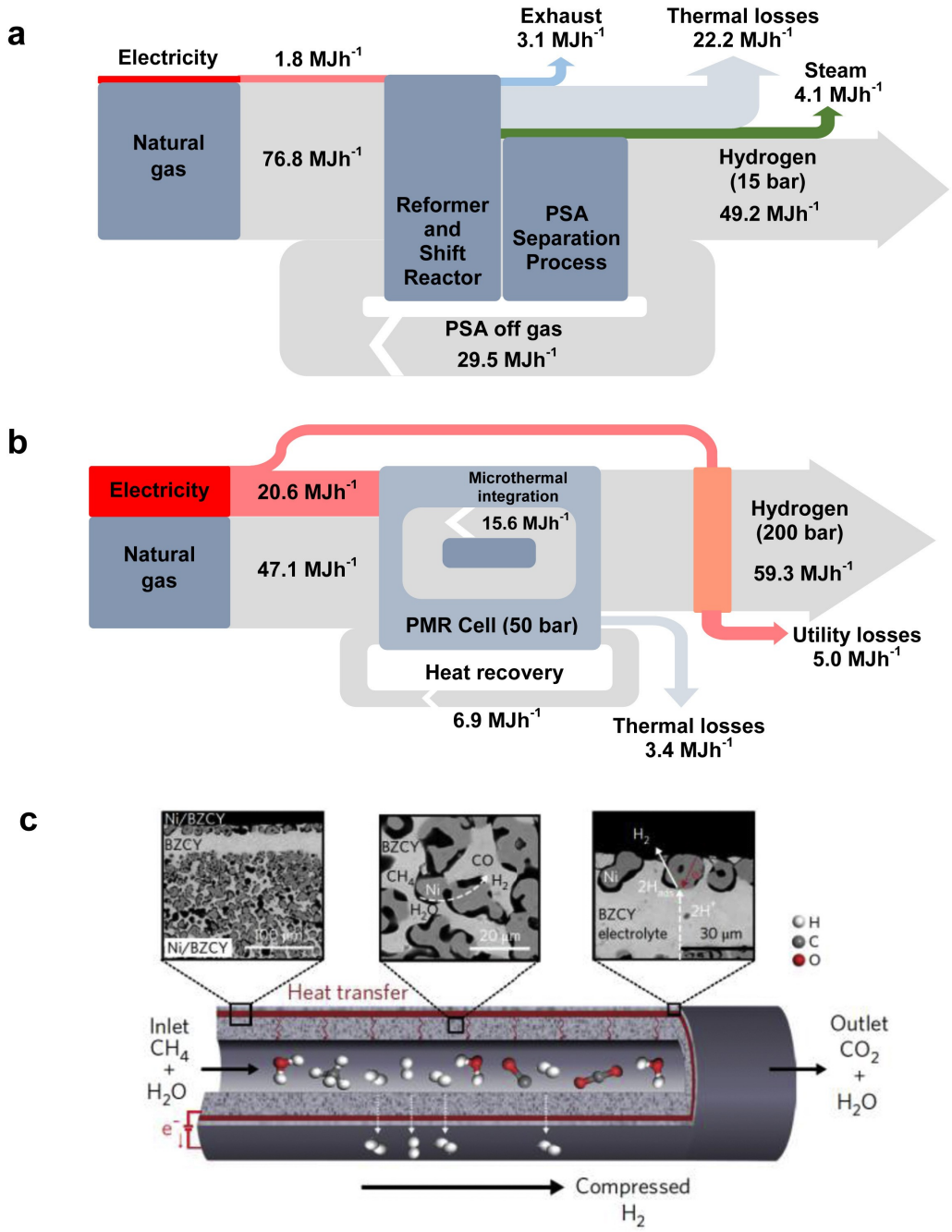

Figure 5.2: The Sankey diagram for the energy flow in the production of 10 kg day^{-1} hydrogen from methane based on (A) large-scale steam methane reforming processes using pressure swing adsorption (PSA) to separate hydrogen [174, 175] and (B) distributed production facilities utilizing a protonic membrane reformer. (C) Schematic of the membrane electrode assembly for a ceramic-based protonic membrane reformer to electrochemically produce compressed hydrogen from methane. The Sankey diagram and schematic for the protonic membrane reformer have been adapted from Ref. [4] with permission from Springer Nature, Copyright 2017.

coverage [13, 15, 177, 178]. In a similar manner, electrochemical SMR reactors using cationic conductive electrolytes can selectively remove protons from the anode side of the membrane and generate compressed hydrogen at the cathode. Separation of the hydrogen from the reaction stoichiometry in the anode has the added benefit of shifting equilibrium to enhance water gas shift and force complete conversion of methane to CO_2 while simultaneously producing high-purity hydrogen at high pressures in the cathode. Heat generated due to compression and separation of hydrogen through the electrical operation of the membrane can be utilized by the endothermic reforming reaction, whereas in thermochemical systems, this energy would be lost. The combination of these functions in a single spatially integrated stage at the micro-scale (Fig. 5.2 (c)) confers high overall energy efficiency, process simplicity, and compactness in PMRs [4].

The development of any advanced chemical manufacturing system must address the challenges associated with product separation and overall conversion. Fundamental studies in electrocatalysis are necessary but must be integrated within the development of product separation and energy integration systems. Otherwise, it will be difficult to consolidate a research and development effort that could truly drive the decarbonization of the chemical industry. In this regard, high-temperature and mid-temperature electrochemical cells are unique in that they integrate multiple steps into single units through the highly efficient internal heat integration and utilization of applied potentials. Although these systems still suffer from poor stability and high cost for fabrication, thermo-electrochemical cells are leading the way in development of competitive processes needed to displace traditional thermochemical systems [4, 168, 169, 179, 180].

5.3 Current state of electrochemical methane transformation to chemicals

Research in electrochemical methane activation and transformation to chemicals has made major advances in the past five years. Most notable is the development of highly conductive proton

conducting ceramic electrolytes for use in high-temperature (800 °C) membrane electrode assemblies (MEAs). A $BaZr_{0.8-x-y}Ce_xY_yO_{3-\delta}$ ceramic tube coated with a nickel oxide catalyst, similar to that found in thermal catalyst systems, was used to produce high-purity compressed hydrogen at 91% faradaic efficiency (FE) with nearly complete methane conversion to CO_2. Technoeconomic analysis indicates that a system based on this design could be competitive with conventional large-scale SMR and could be easily scaled to smaller applications. Utilization of resistive heating and electrochemical separation of protons by the MEA allowed the system to internally generate the heat required to balance the endothermic SMR reaction [4]. A similar system was used in direct synthesis of ammonia from methane [18, 168]. While the anode remained the same as the SMR reactor, the cathode utilized a vanadium nitrate catalyst, resulting in FE of up to 15% and ammonia synthesis rates of up to $1.89x10^{-9}$ mol cm^{-2} s^{-1} at ambient pressure, some of the best results to date [167]. The unique advantages of MEAs make them ideally suited for transformations of methane to higher-value chemicals and have previously been investigated primarily in the form of solid oxide type reactors utilizing anion exchange membranes. However, these systems struggle with durability and often require additional separation of products which needs to be addressed in the future [4, 181–185].

Although electrochemical reforming of methane to make hydrogen and ammonia has made significant progress, direct oxidation of methane to methanol and other oxygenates has remained challenging because of a trade-off between selectivity and conversion caused by unfavorable thermodynamics [13, 15, 171, 177]. Recently, vanadium (V)-oxo dimer clusters in H_2SO_4 have been shown to convert methane to CH_3OSO_3H at room temperature, achieving an FE of 84.5% (much higher than thermal catalysts) under 3 bar methane, showing stability for 240 h [199]. The reaction with H_2SO_4 protects the methanol group from over-oxidizing and doubles as the electrolyte. Additional steps would allow for hydrolysis of CH_3OSO_3H to methanol and reuse of the electrolyte but would reduce overall efficiency. Transition metal oxides including NiO/ZrO_2, $Ni(OH)_2/ZrO_2$, and Co_3O_4/ZrO_2 have also been explored as options for room temperature electrochemical oxidation

Table 5.1: Summary of current state-of-the-art systems for electrochemical methane transformation to chemicals.

Electrocatalysts	Temperature (°C)	Pressure (bar)	Oxidant source	Electrolyte	Technique/Method	Products	Methane conversion (%)	Selectivity (%)	Energy efficiency/ Faradaic efficiency (%)	Ref.
$Sr_2Fe_{1.5}Mo_{0.5}O_{6d-\delta}$-$Ce_{0.8}Sm_{0.2}O_{1.9}$ (SFM-SDC)	750-850	1	H2O	$La_{0.9}Sr_{0.1}Ga_{0.8}Mg_{0.2}O_{3-\delta}$ (LSGM)	Solid oxide electrolyzer	CO + H_2 (syngas)	32.2	H_2: 83.7	(F.E. > 100)	[183]
Ni-YSZ	800	1	O_2	YSZ layer	Solid oxide fuel cell	CO + H_2 (syngas)			E.E. > 75	[186]
$La_{0.75}Sr_{0.25}Cr_{0.5}Mn_{0.5}O_{3-\delta}$ (LSCM)	800	1	H_2O	$La_{0.9}Sr_{0.1}Ga_{0.8}Mg_{0.2}O_{3-\delta}$ (LSGM)	Solid oxide electrolyzer	CO + H_2 (syngas)	90	H_2 < 67	F.E. = 60-100	[187]
Ni-BZCY	800	50	H_2O	$BaZr_{0.8-x-y}Ce_xY_yO_{3-\delta}$ (BZCY)	Protonic membrane reformer	H_2	99.9	98	E.E. = 87 F.E. = 89.9	[4]
NiO-BZCY	500	1	H_2O	$BaZr_{0.1}Ce_{0.7}Y_{0.2O3-\delta}$ (BZCY)	Protonic ceramic electrochemical cell	H_2	80		F.E. = 97.5	[184]
$PdSO_4$	140	6.9-35	H_2SO_4	H_2SO_4	Three-electrode cell	CH_3OH	100		F.E. = 46	[185]
V_2O_5/SnO_2	100	0.1	O_2	$Sn_{0.9}In_{0.1}P_2O_7$	Solid oxide fuel cell	CH_3OH		88.4	F.E. = 61.4	[188]
Pd Au/C	50-250	0.5	O_2	$Sn_{0.9}In_{0.1O7}$	Solid oxide fuel cell	CH_3OH	0.012-0.38	6-60	F.E. = 0.0016-0.0048	[189]
VN-Fe/Ni-BZCY72	550-650	1	H_2O	$BaZr_{0.8}Ce_{0.1}Y_{0.1O3-\delta}$ (BZCY81)	Electrochemical Haber-Bosch	NH_3	64-86	>92	F.E. = 14	[168]
$Sr_2Fe_{1.5}Mo_{0.5O6-\delta}$ (SFMO)	850	1	H_2O	$La_{0.9}Sr_{0.1}Ga_{0.8}Mg_{0.2O3-\delta}$ (LSGM)	Solid oxide electrolyzer	C_2H_4, C_2H_6, H_2	41	82.2 (C_2H_4 and C_2H_6)	F.E. = 80-95	[16]
Mo/MCM-22 (zeolite)	710	1	O_2	$BaZr_{0.7}Ce_{0.2}Y_{0.1O3-\delta}$ (BZCY72)	Co-ionic membrane	C_2 products, C_6H_6, C_7H_8, $C_{10}H_8$	30	>85 (total)	E.E. = 60	[190]
$ZrO_2/NiCo_2O_4$	RT	1	CO_3^{2-}	Na_2CO_3	Three-electrode cell	$CH_3CH_2CH_2OH$, $CH_3CH(OH)CH_3$, CH_3CH_2COOH, CH_3COCH_3,	47.5	CH_3CH_2COOH: 65	F.E. = 100	[191]
ZrO_2/Co_3O_4	RT	1	CO_3^{2-}	Na_2CO_3	Three-electrode cell	$CH_3CH_2CH_2OH$, $(CH_3)_2CHOH$, CH_3CHO,	40	>60 (total)	(F.E. > 100)	[192]
$TiO_2/RuO_2/V_2O_5$	RT	1	H_2O	Na_2SO_4	Three-electrode cell	C_3OH, HCHO, HCOOH	100	CH_3OH: 97.7	F.E. = 57	[193]
Pt	130	46.5	($V^{IV}O$) (SO_4)	$K_2Pt^{II}Cl_4$ with NaCl	Three-electrode cell	CH_3OH, CH_3Cl, $CH_2(OH)_2$, HCOOH	13-16	CH_3OH: 70	F.E. = 90-103	[194]
NiO/ZrO_2	40	1	O_2	Na_2CO_3	Membrane electrode assembly	CH_3OH, HCHO, HCOOH, C_2H_5OH, CH_3COOH, C_3H_8O, C_3H_6O		HCHO: 44		[195]
NiO/Ni hollow fiber	RT	1	OH^-	NaOH	Three-electrode cell	CH_3OH, C_2H_5OH		CH_3OH: 78 C_2H_5OH: 95	CH_3OH F.E. = 54 C_2H_5OH F.E. = 85	[196]
NiO/Ni	RT	1	OH^-	NaOH	Two-electrode cell	CH_3OH, C_2H_5OH	100	87	F.E. = 89	[197]
Nanotube ZrO_2/Co_3O_4	RT	1	CO_3^{2-}	Na_2CO_3	Three-electrode cell	C_2H_5OH, $CH_3CH_2CH_2OH$, $CH_3CH(OH)CH_3$		91.98 ($CH_3CH_2CH_2OH$ and $CH_3CH(OH)CH_3$)		[198]
(V)-oxo dimer	RT	3	SO_42^-	H_2SO_4	Three-electrode cell	CH_3OSO_3H	100	100	F.E. = 85-90	[199]
NiO/ZrO_2	RT	1	O_2	Na_2CO_3	Membrane electrode assembly	CH_3OH			F.E. = 5	[200]

of methane in carbonate-based electrochemical systems [192, 195, 200]. Intriguingly, the FE in some of these systems is above 100%, suggesting that chemical reactions between methane and stoichiometric oxidants in the catalyst or the electrolyte could also be responsible for production of oxygenates. Future studies should seek to gain a fundamental understanding of kinetics associated with zirconium in electrochemical systems and the mechanisms underlying the formation of ethanol and propanol in these catalysts. The use of MEAs in the production of methanol has also shown promise, as it allows advanced control over the catalyst environment and selective transport of reactants. However, lack of coherent methods for reporting results leads to difficulty comparing results between investigations. Recent research in this area has been summarized by Fornaciari et al. [181] and thus will not be presented in detail here. Additional reports of electrochemical catalysts and electrolytes for the electrochemical transformation of methane to higher-value chemicals are compiled in Table 1 along with operating conditions, main products, and FEs.

5.4 Summary of targets for future development

Through economic studies and the analysis of energetics related to individual reactions, targets for development of electrochemical systems have been proposed in the last few years. It has been suggested that conditions of 70% selectivity, 1 V overpotential, and current densities of 0.5 A cm^{-2} could allow the electrochemical oxidation of methane to methanol to be viable [13, 182]. Current systems struggle to achieve these conditions primarily because low overpotentials are required to minimize over oxidation and maximize selectivity. MEAs may provide new insights into addressing the issues associated with the selectivity and conversion trade-off, although improved durability and ease of manufacturing will be required for commercialization [181].

The productivity target often suggested for ammonia is $1x10^{-7}$ mol cm^{-2} s^{-1} [173]. Specifically, in the case of ammonia, it should be noted that while high conversion is often expected to be a final result of electrochemical systems [168, 192], thermodynamics is often a limiting factor. As such,

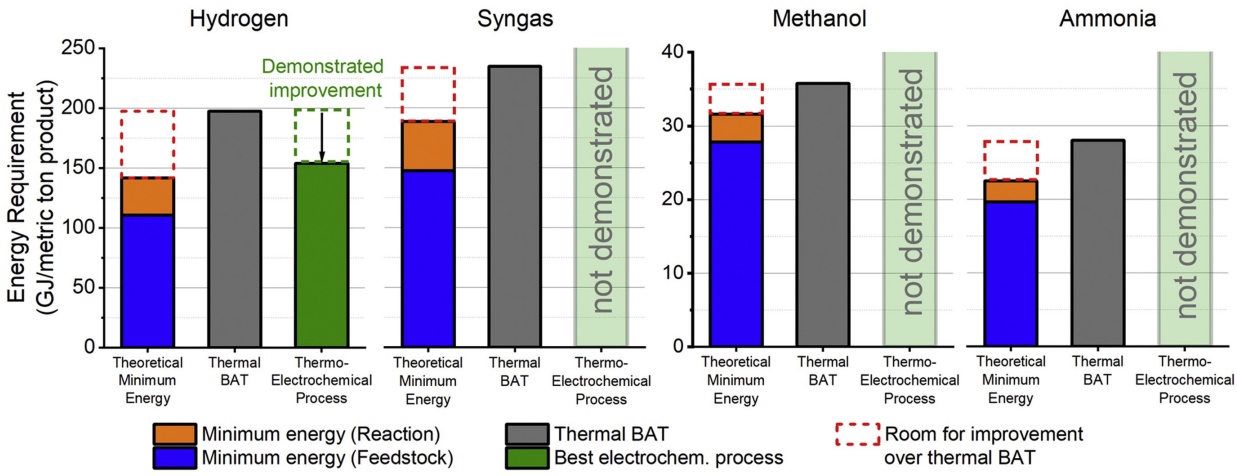

Figure 5.3: Comparison of minimum energy requirements for production of select products from methane by thermochemical and electrochemical techniques. Blue is energy contained in methane feedstock, orange is energy required by the heat of the reaction, green is energy required by the best available electrochemical technique, and gray is energy required by the best available thermochemical technique.

it would be unreasonable to expect significantly higher single pass conversion in electrochemical systems without product separation being integrated into the synthesis reactor. Fig. 5.3 compares the minimum energy requirements for production of select chemicals from methane against the best demonstrated technologies by thermochemical and electrochemical techniques. To date, systems that include product separation have only been reported for the production of hydrogen from methane.

5.5 Concluding remarks

Electrification of the chemical industry could create an intersectoral platform for decarbonized supply chains from natural resources to consumers through the efficient use of carbon and renewable electricity. Although recent developments have brought electrochemical SMR to the cusp of being economically competitive with traditional SMR, electrochemical direct oxidation to methanol and integrated ammonia production from methane still have many challenges to overcome. For ammonia synthesis, more active cathode catalysts and solid electrolytes that show

adequate conductivity at lower temperatures are needed to improve conversion and eliminate ammonia decomposition at high temperatures. Similar advances would benefit electrochemical SMR as well. Research in direct oxidation of methane to methanol needs to address the trade-off between selectivity and conversion or be coupled with efficient separation techniques developed to allow production at low conversion but high selectivity. Overall, a shift to systems-based analysis of experimental results is necessary to clearly see how individual parts of electrochemical systems can be integrated to allow developing technologies to penetrate the industrial sector.

Chapter 6

Development and testing of the Electrified Steam Methane Reforming Test Reactor (E-SMaRT-R)

6.1 Introduction

As discussed in the previous Chapter, electrochemical activation of methane has the potential to provide many advantages in the production of fuels and chemicals. While many technologies are being investigated, the recent development of highly stable and conductive proton conducting $BaZr_{0.8-x-y}Ce_xY_yO_{3-\delta}$ (BZCY) ceramics appear to be an especially promising technology. In SMR, these ceramic membranes have been shown to enhance the production of methane by shifting the thermodynamic equilibrium of the SMR reaction [4, 116]. By electrochemically pumping protons away from the anode where the SMR and water gas shift reactions are occurring, the thermodynamic equilibrium of the reactions is shifted toward full conversion, resulting in higher conversion of methane, and improved selectivity for CO_2 (vs. CO), thus maximizing hydrogen yield. Additionally, driving protons across the membrane results in heat generation within the

membrane that can be balanced with the endothermicity of the SMR reaction, eliminating the need for an external heat source and improving the thermal distribution in the catalyst.

The performance of the BZCY membrane is provided by the combination of rare earth metal doped perovskite oxides of barium cerates and zirconates. While barium cerates show high proton conductivity, they suffer from low tolerance for CO_2 and H_2O. On the other hand, Barium Zirconates exhibit poor proton conductivity but are highly stable. When combined together their characteristics can be combined to create both highly stable and conductive membranes. BZCY is a mixed conductor and depending on composition and atmosphere in which the membranes are operated, four different charge carriers may be present. Generally, the desired charge carrier is protonic-defects. These protonic-defects are created under humid atmospheres when oxygen vacancies, created by the substitution of Zr^{4+} with Y^{3+}, are hydrated through the Stotz–Wagner mechanism [201]. As such, the proton conductivity is dependent on the partial pressure of H_2O in the atmosphere it is exposed to [4, 202]. However, under oxidizing atmospheres, oxygen can be incorporated into the lattice to form holes or electronic defects that facilitate the conduction of electrons or oxygen ions, respectively. Electron conduction can also be facilitated by the reduction of Ce^{3+} in membranes with high Ce content [201, 203–206].

Grain size of the ceramic also plays a significant role in the conductivity. Protons are thought to conduct through the ceramic by a mechanism similar to the Grotthuss mechanism where protons hop between oxygen vacancy sites in the crystal lattice [204]. When conducting through a grain, the crystal structure is uniform and the proton can take a direct path. However, at the grain boundary, this mechanism is disrupted. A resistance contribution from the grain boundary can be extracted using electrochemical impedance spectroscopy and resistance has been shown to increase when grain size is decreased [207]. Generally grain size is established during the sintering process and many techniques have been investigated to maximize the grain size, or densify the ceramic while maintaining mechanical stability including the use of sintering aids[203, 208] high pressure sintering [209], and microwave sintering [207]. Other parameters that are commonly investigated

include the use of dopants besides Y [210, 211], controlling the morphology of the electrodes to improve mass transport and electrical conductivity [212], and bi-layer membranes [202].

Experimental systems typically utilize either planar or Tubular membrane geometries. Planar electrodes are typically tested in coin cell type configurations, although recent efforts have investigated larger format membranes to investigate scale-up feasibility [213, 214]. Tubular membranes are popular for experiments involving high pressure since the pressure gradient can be directed to exert a compressive force rather than tensile stress on the membrane to prevent fracture [215]. The ability to apply a pressure gradient also provides some unique opportunities for tubular membranes. Since the outside of the tube can be at a much higher pressure than the inside, the membrane can be used to electrochemically compress the hydrogen by pumping protons against the pressure gradient. Alternatively electricity could be generated by letting protons move along the pressure gradient. In the first case, a pressure dependent overpotential would be necessary to pump the protons against the gradient, while in the second case, the pressure difference would generate a potential difference across the membrane [116]. The ability to compress hydrogen as a part of the separation and reaction process is especially useful in the case of SMR since the energy required to compress the gas will generate heat in the membrane that can then be used to balance the energy consumed in the reaction [4].

The ability to combine heat generation, with hydrogen separation and compression provides an opportunity to intensify the SMR process. Further intensification can be achieved by coupling the SMR reaction with the production of other chemicals. For example, a vanadium oxide catalyst was applied to the cathode of a tubular BZCY membrane and nitrogen was fed to the cathode side while SMR was performed on the anode. This enabled the SMR reaction to provide protons to the nitrogen reduction reaction to produce ammonia on the cathode reaching up to 15% single pass conversion [168]. Other studies have looked at coupling CO_2 reduction [58] and conversion of methane to aromatics [190]. Overall, the unique properties of BZCY ceramic membranes provide numerous options for electrochemical synthesis pathways that remain to be fully explored.

With this in mind, a test system was designed to provide testing capabilities for tubular BZCY membranes capable of operating at high pressure and temperature. The following Chapters will provide a detailed account of the design, operation, and challenges associated with the development of the Electrochemical Steam Methane Reforming Test Reactor (E-SMaRT-R) system. Initial tests will be performed on a 15 cm^2 BZCY membrane supplied by Coorstek, and initial results will be presented in this chapter. The E-SMaRT-R system provides the capability to test high temperature and pressure electrochemistry and could be applied to other membrane chemistries as well. The capabilities and flexibility that this system provides will enable testing of numerous reaction conditions and chemistries, as well as future demonstration of Smart Manufacturing (SM) methods as discussed in Chapter 2 of this thesis.

6.2 Critical factors in the design and operation of the Electrified Steam Methane Reforming Test Reactor (E-SMaRT-R) system

Design of a system capable of performing high quality electrochemical measurements for gas phase reaction at high temperature and pressure, presents unique challenges. To accomplish this task, careful selection of equipment, control schemes, and appropriate sensors is need to ensure the system functions as expected. This Chapter begin by detailing the overall E-SMaRT-R system design, beginning with an overview of the system P&ID, followed by specification of the critical sensors and equipment used in construction. Next is a discussion of key challenges that were faced during development along with the resulting solutions. Finally, preliminary results are presented from tests performed with the E-SMaRT-R system after construction. Overall, this Chapter will provide the reader with knowledge of all the critical design and operation factors required for reliable system performance. Additionally, discussion of how a LabVIEW based user interface

(UI) is integrated with data collection and system control, serves as an example of how Phase 1 of the smart manufacturing inspired framework (discussed in Chapter 2) can be implemented in experimental systems.

6.2.1 Overview of system design

The P&ID of the E-SMaRT-R system is presented in Fig. 6.1 showing the various sensors, equipment, and control loops within the system. Here, gas lines are designated by solid lines, sensor signals are designated by single slashed lines, control signals have double slashes, and electric connections for process heat, potential and current control/sensing are specified with triple slashed lines. Additionally, pressure and temperature sensors are represented with boxes containing a P or T accordingly. Major pieces of equipment are labeled, and heated equipment is colored red. All control loops are interfaced with a LabVIEW based UI to allow for automation and remote control. This interface with the UI is represented by a box containing two adjacent triangles.

Starting from the right of Fig. 6.1 the gas flow rates into the system are controlled using thermal mass flow controllers (MFC). Currently MKS brand MFCs (model GE50A) are used, along with an MKS 946 vacuum system controller, but these MFCs are limited to operating pressures below 7 bar. Plans are in place to replace these MFCs with new SLA series MFCs from Brooks Instrument that are designed to operate at up to 50 bar. The current configuration has three MFC controlling feed gas to the anode and two controlling the feed to the cathode. This allows for controlled flow of CH_4 and H_2 as reactants and Ar at low concentration as an internal standard to measure volumetric changes on the anode. He is typically fed on the cathode during experiments, but the second mass flow controller allows for hydrogen flow when not performing experiments to keep the reactor in a reducing atmosphere. Following the gas lines from the MFCs, the feed gas passes through a set of valves that allow the gas to either be humidified in the steam system or bypass the steam system.

If the gas is to be humidified, the gas enters a 1 L stainless steel (ss) pressure vessel where the humidification occurs. Humidification is controlled utilize the temperature dependence of the

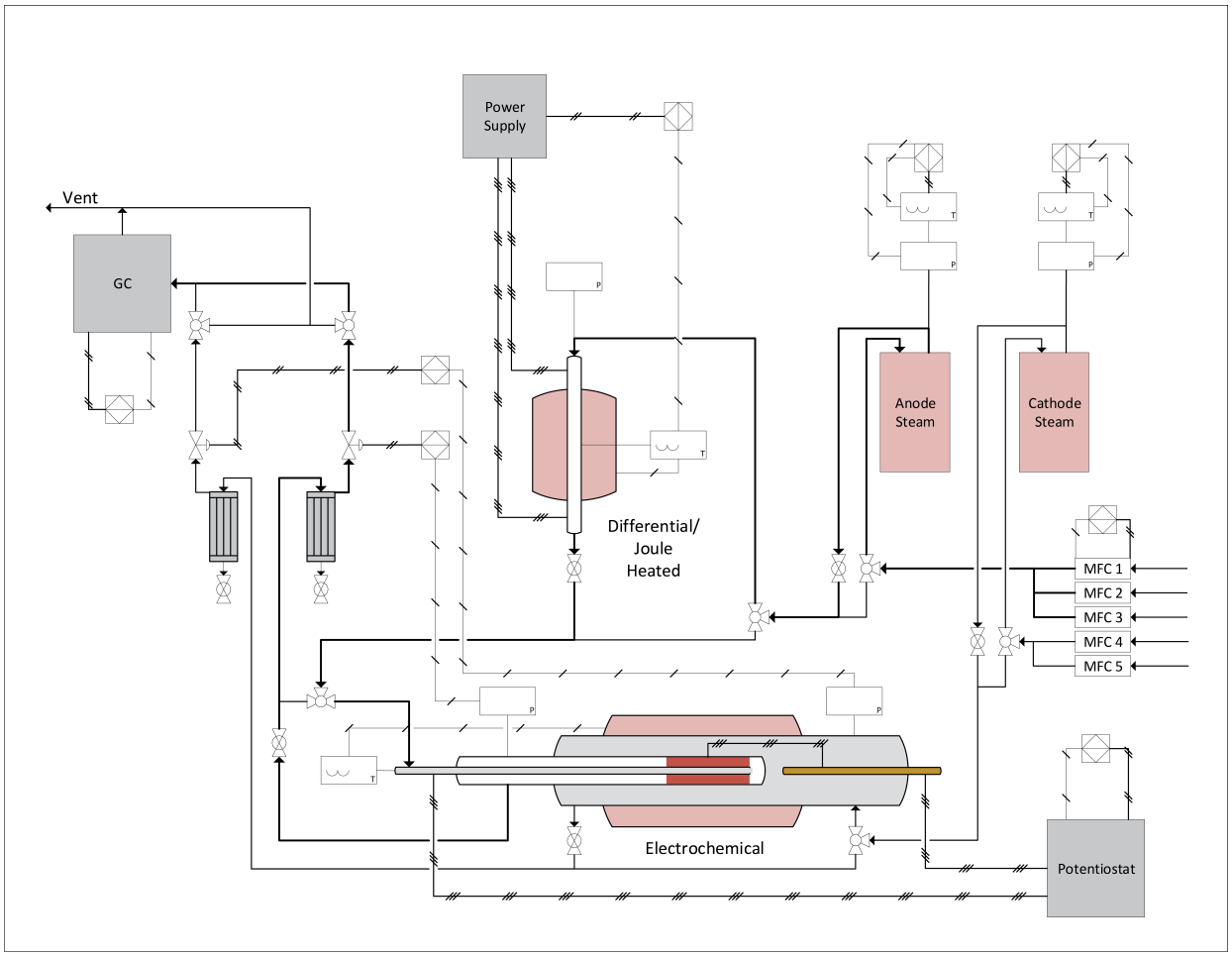

Figure 6.1: A P&ID of the E-SMaRT-R system. Gas flow paths for the cathode and anode are represented by solid lines. Electric connections that sense and control the current and potential are represented by lines with triple slash marks. Control loops involving automated sensors and controllers are represented by boxes containing adjacent triangles with sensor and control signals designated with single slashed and double slashed lines respectively. Temperature and pressure sensors are labeled with a T or P respectively. The system incorporates a total of 18 automated sensors/controllers and is designed to operate at system pressures up to 50 bar and reactor temperatures up to 900 ^{o}C under gas flow rates over 1000 SCCM.

vapor pressure of water. The ss pressure vessel is partially filled with liquid water and the gas is bubbled through a sparger submerged well below the level of the liquid. The temperature of the water is measured by a submerged thermocouple and the pressure in the steam box is measured by a sensor connected to the top of the steam system. A liquid level indicator is also attached in parallel to the pressure vessel to provide an estimate of the water level and to ensure that the water level does not drop below the level of the thermocouple or gas sparger. The gas sparger insure good mass transport between the liquid and the gas bubbles at high flow rates. The temperature of the pressure vessel is also controlled by a local control box that modulates the power output to a resistive heat tape wrapped around the bottom third of the pressure vessel. By controlling the temperature of the liquid, the vapor pressure can be set to provide the desired concentration of steam. Steam fraction can be calculated by simply dividing the vapor pressure of water by the system pressure measured in the steam system (Eq. 6.1).

$$Steam fraction = \frac{P^{vap}}{P_{total}} \tag{6.1}$$

In other words, the partial pressure of steam in the effluent of the steam system is equal to the vapor pressure created by the liquid. As the gas bubbles through the liquid and the head-space above the liquid, it equilibrates with the water vapor and the humidified gas exits the head-space of the steam system at the top of the pressure vessel at the desired concentration of steam. As long as $P_{total} > P^{vap}$, the steam fraction in the effluent of the steam system can be controlled reliably.

However, if $P_{total} < P^{vap}$ the liquid will begin to evaporate rapidly and risks flooding the system downstream. In practice, the water will not violently boil, but the flow of steam through the system will increase rapidly to a point where the pressure drop is high enough to make the pressure in the pressure vessel equal to the vapor pressure. This situation should be avoided at all times to prevent damage to soft components (such as PTFE ferrules and valve packing), sensors, and the electrochemical reactor. This is especially problematic if the vapor pressure is high due

to temperature of the liquid increasing, which will not only result in high velocity of steam in the downstream system, but also high temperature steam. Whether the high P^{vap} is due to temperature rise of the liquid or pressure loss in the system, high enough steam flow rates could be reached to overwhelm the condenser system resulting in liquid entering the gas chromatograph (GC) and damaging the sample columns.

It should be noted that while the steam fraction is controlled by the temperature of the liquid water, the flow rate is controlled by the dry gas from the MFCs. All gas lines downstream of the steam system are heat traced and maintained at a temperature above the dew point to prevent condensation until the gas passes through a condenser to remove the steam before entering the GC. After leaving the steam system, the humidified gas on the cathode can either be directed to the shell side of the electrochemical reactor body, or set to bypass the reactor all together.

The anode gas however can be directed to a differential reactor which is configured to allow for heating from an external furnace, or by joule heating of the reactor tube from an external power source. This configuration allows the anode side of the E-SMaRT-R system to be used in isolation to investigate thermal catalysis. Integration with LabVIEW to allow for online control and sensing of these experiments has also been established. For experiments conducted with proton conducting membranes, this section of the reactor can be bypassed completely. After bypassing the thermal catalysis reactor, the anode feed gas can either be fed through the tube side of the electrochemical membrane reactor, or set to bypass the reactor.

To better understand how the electrochemical membrane is constructed, an image is presented in Fig. 6.2 (a) showing the reactor components and the order of assembly. Starting from the top of the image, we see the shell of the reactor. The image shows a 3/4 inch tube, but this along with the fittings connecting either end of the tube, have been upgraded to a one inch diameter tube to avoid unintended membrane breaks during assembly due to imperfect membrane alignment causing contact with the wall. Note that all external components are based on Swagelok gas fittings. This was done to ensure gas tight operation at high pressure and temperature throughout the system. On one

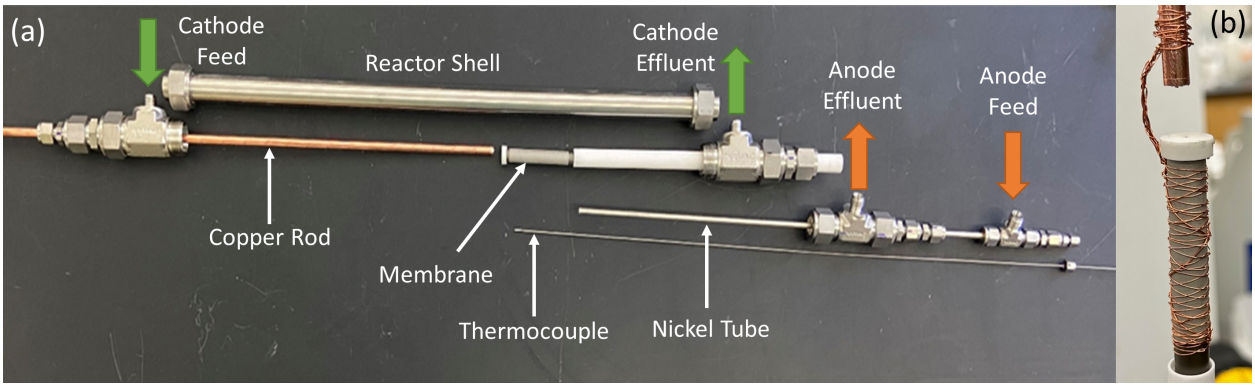

Figure 6.2: Details of the internal components of the electrochemical membrane reactor assembly. (a) From top to bottom (outside-in) the components are shown as follows: Reactor shell, copper current collector and membrane mounted on alumina riser, nickel current collector, reactor thermocouple. (b) An example of how the copper rod was attached to the membrane using oxygen free copper wire.

side of the tube an oxygen free copper rod is inserted until it comes close to the membrane. This copper rod is used to make electrical contact with the cathode (outside) of the cylindrical membrane using 2.5 and 0.25 mm oxygen free copper wire. These wires are tightly wrapped around the outside of the membrane when assembled using a wrap-and-twist method to ensure good contact with the cathode catalyst layer on the outside of the membrane as shown in Fig. 6.2 (b). The ceramic membrane is supported on an alumina tube which is mounted in Swagelok fittings on the opposite side of the reactor shell from the copper rod. A more detailed representation of the internals of the electrochemically active region of the reactor are presented in Fig. 6.3. Nickel wool is tightly packed into the end of the ceramic tube and a 3/16 inch nickel tube is fed through the alumina riser so that it is firmly pressed against the nickel wool. The nickel tube serves two purposes. First it acts as the anode feed inlet allowing gas to enter at the far end of the membrane and flow back through the annular space between the nickel tube and the membrane/alumina riser. It also acts as the current collector for the anode by contacting the nickel wool which provides electric conductivity between the tube and the catalysis layer on the inside of the tubular membrane. Last of all, a 1/16 inch diameter thermocouple with a ss casing is inserted through the nickel tube to measure the internal temperature of the reactor at the center of the membrane.

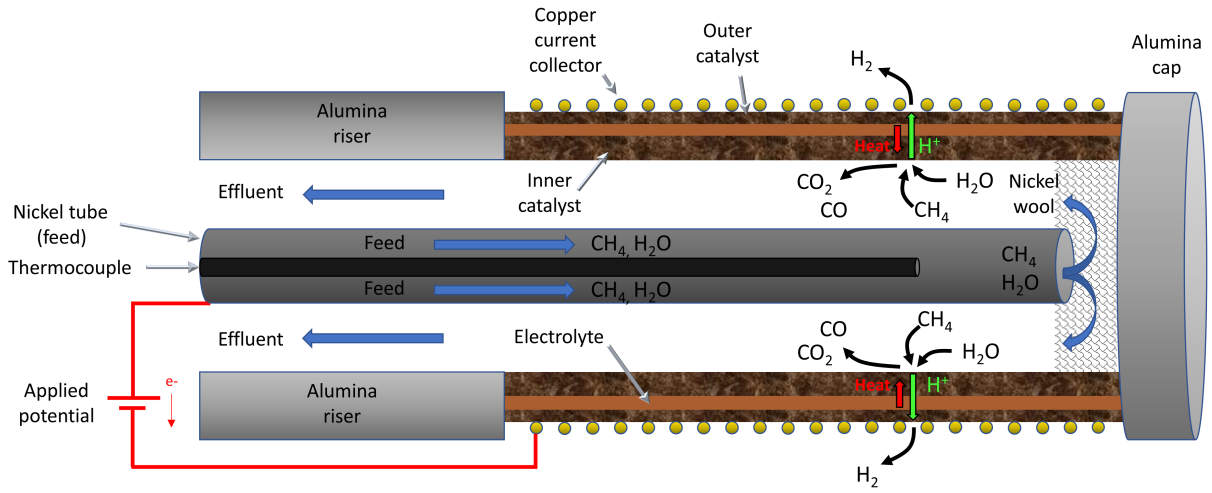

Figure 6.3: A detailed representation of inside the electrochemical membrane reactor. Gas enters through the nickel tube at the center of the membrane and flows out though the annular space between the membrane and the nickel tube. Methane reacts on the internal catalyst layer to produce CO and CO_2 while protons are driven across the membrane by the electric potential and separated from the other gases.

After passing through the reactor, both the cathode and anode effluent pass through condensers to remove remaining steam. Tap water is passed through the shell side of the condenser to provide cooling. The condensers are located before the back pressure regulators (BPR) to minimize moisture in the gas going to the GC and prevent condensation in the vent lines. 1:1 dome loaded BPRs are used to regulate the system pressure and pilot regulators modulate the control pressure for the cathode and anode independently. Dry gas can then be directed to either vent or pass through the GC for quantification of the effluent composition. The valves are configured so that the operator can choose only one effluent stream to pass through the GC or to allow both effluent streams to flow at the same time.

6.2.2 Critical components for sensing and control

System control and sensing is achieved through the use of a LabVIEW UI shown in Fig. 6.4 that interfaces with the critical sensors and equipment to allow automated data collection, storage, and processing. Here an automated python script has been implemented similar to that discussed

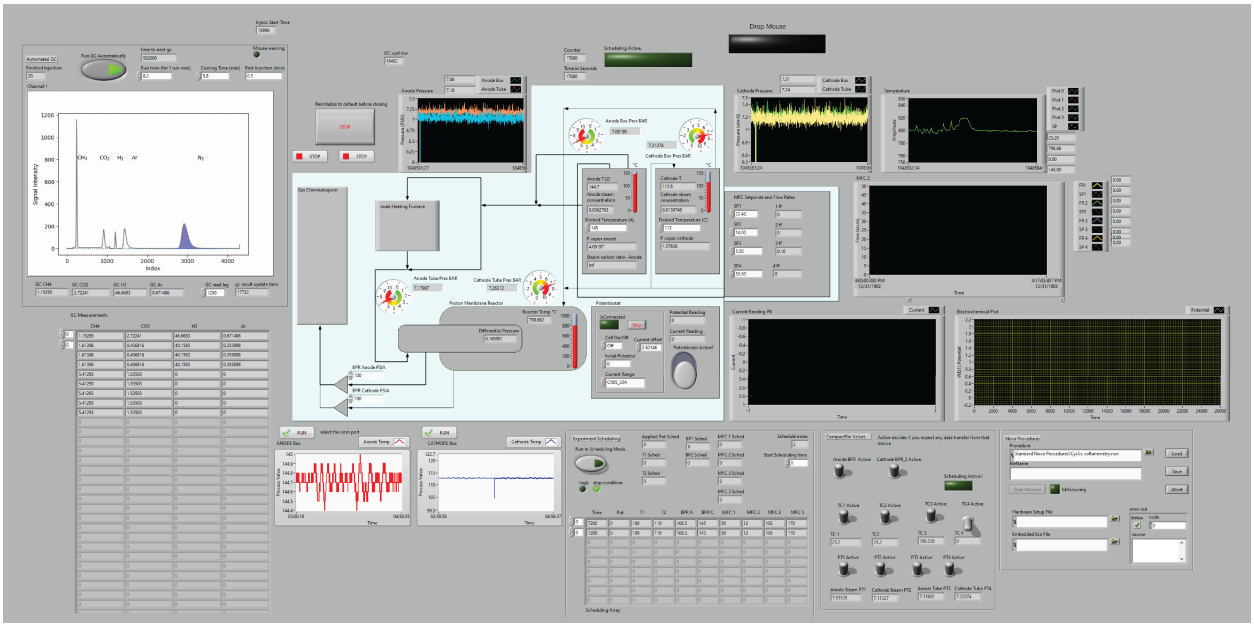

Figure 6.4: The LabVIEW user interface developed to allow automated methods of data collection and storage to be utilized. The layout of the UI is designed to have the same configuration as the real system, so that the connection between the information in the UI can be readily understood in relation to the real system.

in Chapter 1 to collect and process data from the GC. Additionally, a feature was added that allows various changes of the reactor conditions to be automated. This feature allows efficient collection of steady state data across a wide range of operating conditions with nearly unsupervised operation. Then not running using this automation script, the UI provides centralized manipulation of process variables and the ability to remotely control and monitor system performance. In the future this UI will also be used to demonstrate real-time process control at optimized operating conditions as well as for online fault detection and response.

As mentioned previously, control of the steam concentration is based on the temperature of the water and the pressure in the steam system. A K-type thermocouple is used to measure the temperature of the water and is read by an Omega platinum series control box. This control box has an internal proportional-integral controller that modulates the power output to the heat tape for the steam system. Temperature control is performed locally in the control box so that if LabVIEW crashes the system can maintain appropriate control of the temperature. Communication with the

control box is provided through a USB connection that allows LabVIEW to read the temperature of the thermocouple and send a set-point to the control box. Omega general purpose pressure transducers with a range between 0 and 70 bar are used to sense the system pressure. These transducers produce 4-20 mA signal that is proportional to the pressure in the system, and LabVIEW senses this signal through a CompactRIO module (model NI-9203). Pressure transducers are locate on each steam box and near the inlet of the cathode and anode gas streams to the reactor.

Control of the electrochemistry is provided by a Metrohm PGSTAT302N potentiostat paired with a 20 A booster that allows for current up to 20 A and potentials up to 10 V. This was connected with LabVIEW though a USB connection. Shielded cable, >10 gauge was used to extend the provided cables from Metrohm to connect the potentiostat to the E-SMaRT-R system. Clamps were fabricated from sheets of copper to attached the cables to the exposed section of the Nickel tube for the anode, and the copper rod for the cathode.

The pilot regulators (Equilibar, EPR 1000) used to provide the control pressure for the BPRs (Equilibar, LF series) respond to a current signal in the range of 4-20 mA. This signal is sent from LabVIEW using an NI-9265 CompactRIO module. It should be noted that the BPR system does not send a signal to LabVIEW. Since the pressure of interest is not the system outlet pressure, this information is not needed to control the system. Instead, system pressure is sensed by pressure transducers and the control signal to the BPR pilot regulator can be adjusted if needed to reach the desired system pressure.

In addition to the pilot regulators and pressure transducers, the thermocouple inside the reactor was also connected through the CompactRIO using a configurable NI-9219 module. Temperature measurements are double checked with a handheld thermocouple reader (Omega, model number HH806AU). A multichannel temperature reader also provides temperature readings for temperature-sensitive regions of the gas lines using K-type thermocouples. The gas lines are heated to prevent steam condensation using resistive heat tape powered by variable transformers. Since these temperatures do not change during operation, it was not deemed necessary to include these

temperatures in the LabVIEW UI. Instead these temperatures are only used to verify that the heat tape maintains the gas lines at a high enough temperature that steam will not condense, but not so high that the PTFE components used to make some gas connections would lose their structural integrity.

6.2.3 Challenges in system design

Five primary challenges were faced in the development of the E-SMaRT-R system. The first and most important was related to electrically isolating the electrochemical reactor from the rest of the system. Since the gas system is based on ss tubing to provide the high pressure rating, the system acts as one large conductor. The initial design relied on dielectric fittings manufactured by Swagelok to provide electric isolation between two sections of tubing. These fittings were designed to be compatible with the rest of the Swagelok based system and could easily be installed in a section of ss tubing. A dielectric fitting was installed on both the cathode and anode gas lines just after the MFCs, but before the valve controlling the flow of gas to the steam system. Additional fittings were installed after the condensers and before the BPRs. Due to material limitations for the polymer used in the dielectric fittings, these fittings required placement in regions of the system where the line was not heat traced. All contact points on the system were insulated between the dielectric fittings to prevent grounding and the formation of external circuits.

Initial measurements of the reactor showed much higher resistance of the membrane than expected based on previous reports. Additionally, polarization curves showed erratic behavior. For example, when applying linear sweep voltametry, the current could be seen to increase slowly and linearly with increasing potential, but at high enough potentials, the current would suddenly fall to zero. This behavior was determined to be representative of a scenario where the breakdown potential of an insulator was reached, resulting in the formation of an unintended external circuit. In this case, the potential difference between working and counter electrode would continue to increase, but the current would not return to the potentiostat. Instead current would flow through

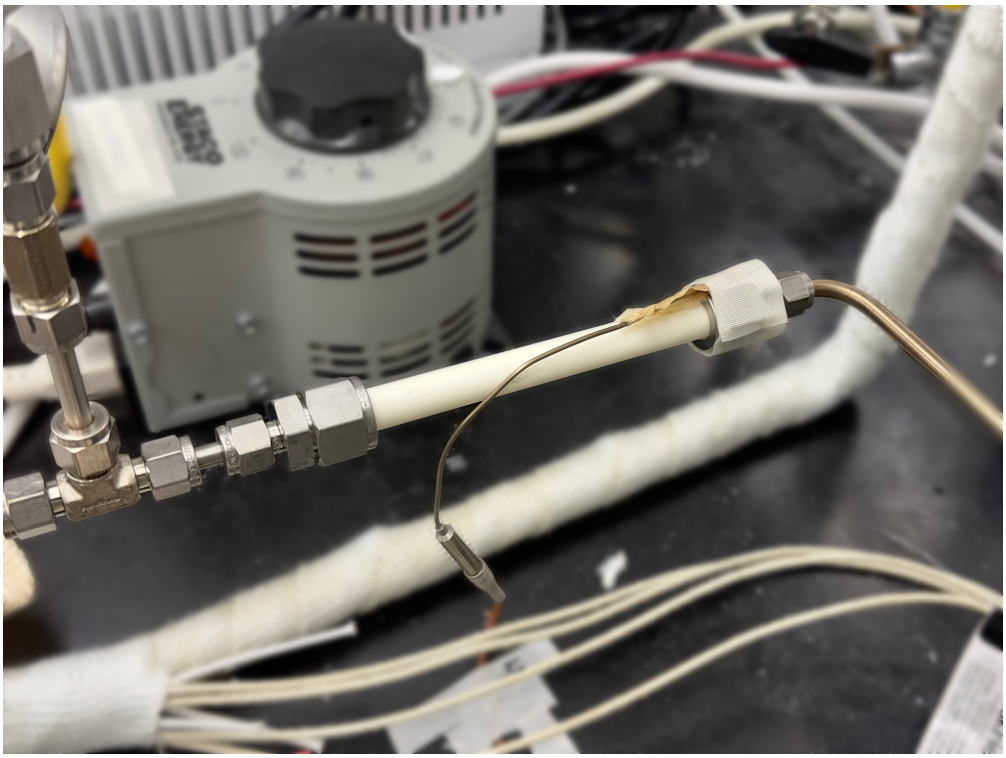

Figure 6.5: Custom made dielectric fittings using short section of alumina tube were used to provide electrical isolation for the reactor.

a low resistance path to an external sink that was created when the breakdown potential was exceeded. Thus, the potentiostat would not measure any current. To identifying the source of this external circuit, various potential grounding sources were systematically removed from the system until it was determined the thermocouples in contact with the metal tubing and connected to the multichannel thermocouple reader were the culprit. Initially it had been assumed that these sensors where electrically isolated since no change in temperature reading was observed when a potential was applied in the system. However, Once these thermocouples were electrically isolated from the ss tubing, the sudden loss of current with increasing potential was no longer observed.

When running later experiments, unexpected fluctuations in steam system temperature where observed showing that the potential applied at the electrode was shifting the voltage signal read by the temperature control box from the K-type thermocouple. To remedy this issue, more dielectric fittings where installed between the reactor and the steam systems. However, due to the inability

to properly heat trace these fittings, condensation would form inside the fitting and bridge the dielectric. The final solution to these electrical isolation issues was the use of short sections of Alumina tube to replace sections of ss tubing close to the reactor. Six inch lengths of 1/2 inch alumina tube with an inner diameter of approximately 1/4 inch (similar to the ss tubing) where fit with Swagelok adapters using PTFE ferrules. This technique of using PTFE ferrules was already used to seal the alumina riser in the reactor to the Swagelok body of the reactor. These *soft* ferrules are stable up to 200 ^{o}C allowing much higher temperatures to be used when heat tracing the tubing. For comparison, the dew point of water at 200 ^{o}C is slightly above 15 bar which is the highest partial pressure that would be expected in normal operation of the E-SMaRT-R system. As such the soft ferrules should be suitable for normal operation. However, this limitation should be kept in mind, since the maximum allowable steam fraction will be limited by these soft ferrules at high pressure. To provide full electrical isolation for the reactor, sections of alumina were installed close to the reactor on inlet and outlet gas lines and all thermocouples were placed outside of these fittings. The only exception is the reactor thermocouple which was determined to have excellent electrical isolation provided by the CompactRIO. An assembled section of alumina tube with the Swagelok adapters is shown for reference in Fig. 6.5.

Having developed a solution for the electrical isolation issue, the reactor performance was much more stable, but showed semi-regular spikes in potential that were unexpected. These spikes in potential where found to correlate with sudden drops in temperature measured in the reactor, suggesting that the problem was not electrical in nature (Fig. 6.6). Instead it was deduced that the fluctuations where caused by rapid increases in gas flow rate that disrupted the thermal equilibrium in the reactor. Investigation of potential sources led to the discovery of two separate contributions.

First, the back pressure regulators were observed to have a consistent pattern of slowly increasing control pressure and rapidly decreasing when attempting to maintain a steady pressure. This rapid decrease in control pressure resulted in a rapid venting of system pressure leading to short periods where the velocity of the gas through the tubing would be increased. As a result, the gas

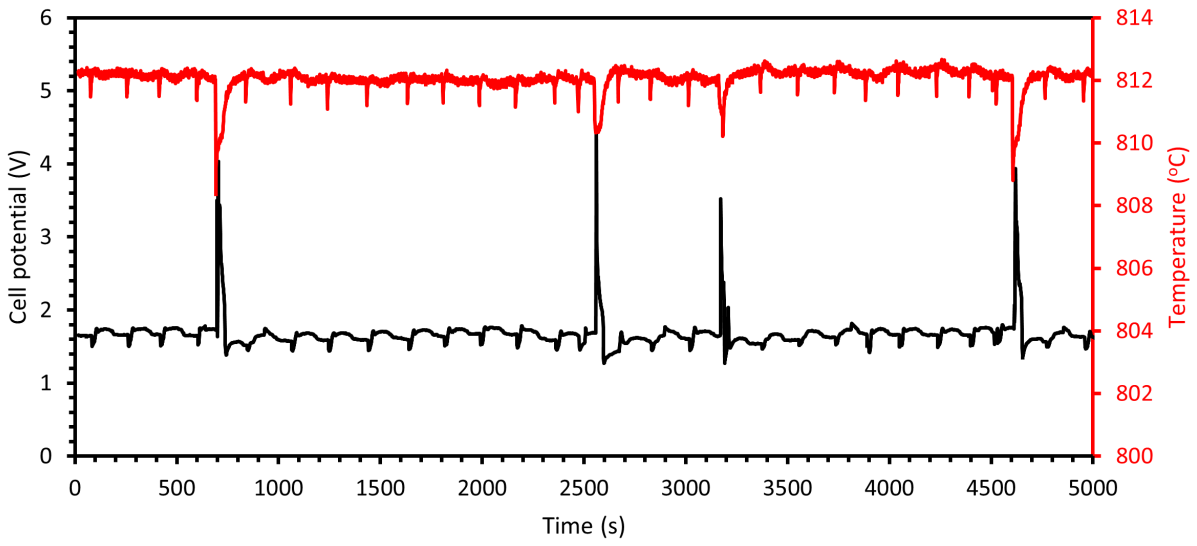

Figure 6.6: Fluctuations in potential correlate with temperature fluctuations in the reactor. These fluctuations were found to originate from changes in the BPR control pressure and condensation evaporating as discrete drops of water fell from cold sections of tubing into hot sections of gas tubing.

entering the reactor would have less time to thermally equilibrate in the furnace before entering the membrane region. This was addressed by increasing the gas volume on the control pressure side of the BPR. The increased volume acts as a buffer for pressure changes in the system helping to regulate the control pressure. Additionally the dead-band for the pilot regulator was adjust from zero to a value of 0.3 psi, meaning that no gas would flow in or out of the control side of the BPR while the control pressure remained within 0.3 psi of the set-point.

While adjusting the back pressure control system helped reduce the number of potential spikes, they were not eliminated. Further investigation identified steam condensation in the pressure sensor lines to be the source of the remaining potential spikes. These lines where vertically oriented as depicted in Fig. 6.7 and not heat traced to prevent heat damage to the electronic pressure transducers. At steam fractions above 10%, condensation would form in these tubes and drip into the hot gas line below, creating a burst of rapidly expanding water vapor. This would result in a higher velocity gas stream causing the reactor temperature to drop and sending a dose of high steam concentration gas through the reactor. This would temporarily flush the reactor of any easily oxi-

Figure 6.7: Pressure sensor lines are located vertically and not heated to prevent damage to the pressure transducers. Placing material in the tube to prevent condensed water from falling in to the hot tube below, eliminated potential spikes caused by condensation in these line.

dizable hydrogen gas, and force the potential to increase to maintain constant current by oxidizing the steam. To eliminate this effect, two successful methods where tested. In one pressure tube, a small section of 1/16 inch ss tubing was placed. This improved heat transfer along the section of tube and increased the surface area to volume ratio so that discrete droplets of water could no longer drop down the tube to the hot zone. In the other tube, inert silica wool was packed in the length of the tube to prevent droplets of water from forming and dropping into the hot zone. Both methods have worked well and the remaining potential spikes have been eliminated.

The last major challenge preventing reliable results from the E-SMaRT-R system was the presence of what appeared to be random shifts in potential, coinciding with rapidly changing membrane temperatures. These rapid shifts in heat generation that could be observed as a change in temper-

ature of the membrane suggested that there was a significant change in cell resistance within the reactor itself. All of the experiments showing shifts in potential, were taken using membranes that had detached from their alumina riser. To assemble the cell on the nickel tube, the tubular membranes where simply slipped over nickel wool that had been wrapped around the nickel tube until the membrane was pressed against the alumina riser again. After careful examination of the assembly it was deduced that the shifting was likely due to variations in contact resistance between the nickel wool and the membrane. This was confirmed when it was discovered that the shifts in potential could be induced by bumping the reactor during experiments. To address this issue we consulted with the membrane supplier and discovered that a more reliable way of ensuring good electrical contact on the anode is by tightly packing nickel wool in the end of the membrane and then installing the nickel rod so that it is firmly pressed against the nickel wool. When the next membrane was assembled, this new technique was used to ensure good electrical contact and the electrochemical performance of the membrane was stabilized.

6.3 Preliminary experiments and results

This section will discuss the experimental results that have thus far been collected from the E-SMaRT-R system to benchmark the performance. For these tests, a 15 cm^2 active area tubular $BaZr_{0.8-x-y}Ce_xY_yO_{3-\delta}$ membrane supported on a 1/2 inch outer diameter alumina tube supplied by CoorsTek Membrane Sciences was used as the benchmark membrane electrode assembly. This membrane electrode assembly consists of a BZCY membrane sandwiched between two layers of porous Ni-BZCY that facilitate electron, proton, and gas transport for the reactions using a nickel catalyst. During initial installation attempts, the outer shell of the reactor was found to be too narrow, causing contact between the end of the membrane and the outer wall of the reactor. When tightening gas fittings during installation, the torque applied would cause the membrane to press against the wall of the reactor causing the membrane to break close to where it was attached to

the alumina tube. The majority of the membrane remained intact, so these membranes were used while troubleshooting the fluctuations in the reactor. To prevent damage, the intact membrane was used only once appropriate control was established for all aspects of the system. Due to the membranes being loosely supported on the nickel rod, good electrical contact between the inside of the membrane and the nickel rod/wool was difficult to obtain. However, after elimination of the other sources of fluctuations in the reactor, the effects of this poor electrical contact were small enough to provide a reasonable degree of control for testing. SMR reactions were tested under galvanic control for current densities between 0 and 1 A cm^{-2}. It should be noted that the membrane was detached from the alumina support for these experiments which allows mixing of gases across the membrane. However, the break of the membrane was located at the outlet of the flow path. While mixing of the gases was unavoidable, the mixing should primarily occur at the outlet of the reactor and after the gas reacts, having little effect on the measured performance. However, independent quantification of anode and cathode gas effluent could not be accomplished in this configuration.

SMR experiments where carried out with the broken membrane at approximately 790 ^{o}C and 7 bar. A steam to carbon ratio (S/C) of 2.5 was targeted, but due to difficulties defining the flow rate with the existing MKS MFCs at this pressure, the actual S/C was calculated to be 2.95. This calculation was performed using a bubble meter to measure the effluent flow rate, coupled with the concentration of the feed gas measured by GC. Anode feed composition was measured by GC to be 20.6% CH_4, 20.4% H_2, and 59% H_2O. He was flown on the cathode with 20% H_2O along with a small concentration of Ar to quantify the volumetric change from the reaction. Gas concentration was measured at 0.033, 0.2, 0.5, 0.67, 0.8, and 1 A cm^{-2}. All gas concentrations were measured by an Agilent GC (model 7890B) using a thermal conductivity detector.

While optimization of the flow rates and conditions is still needed, the results show that changing increasing current density does influence the SMR reaction. Results for experiments conducted with the broken membrane are presented in Fig. 6.8. As the current density is increased, the con-

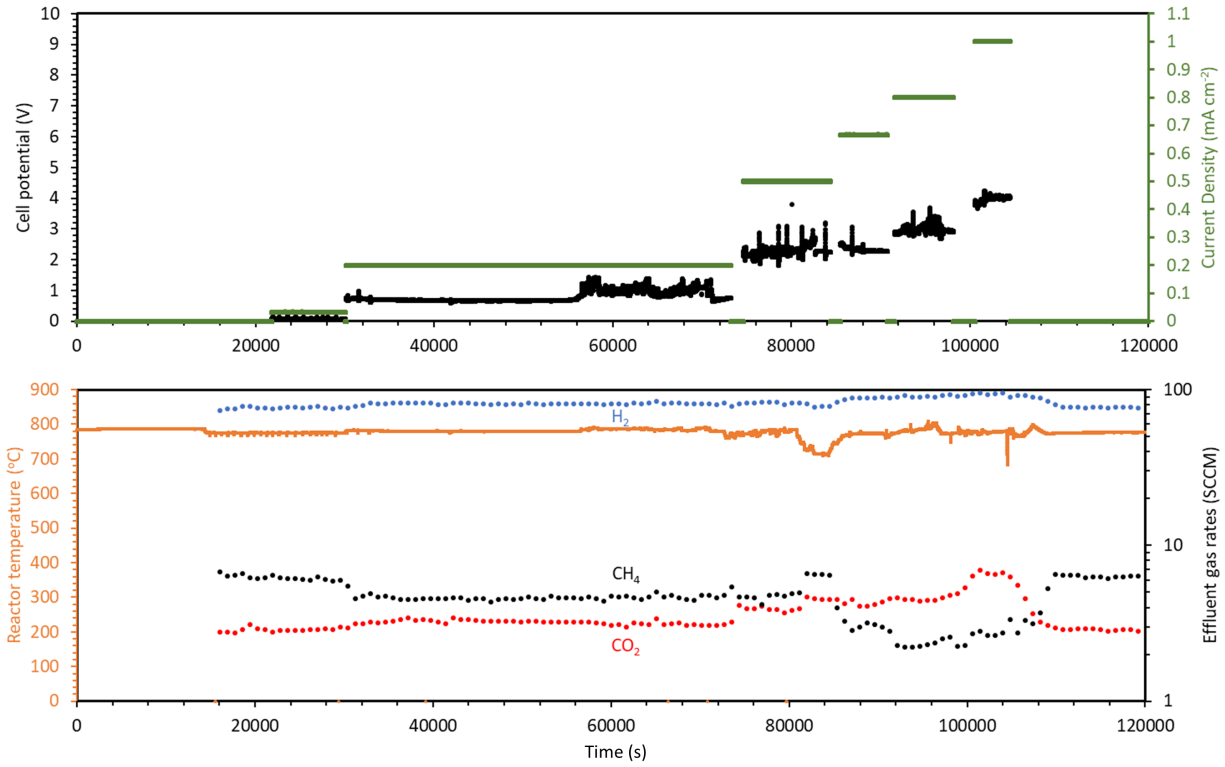

Figure 6.8: Transient experimental data from experiments with the broken membrane showing the transient response of the system to changes in current, potential, and temperature. Measured at 7 bar and S/C=2.95

version of methane increases resulting in lower effluent flow rates of methane. Additionally, a corresponding increase in flow rate for CO_2 and hydrogen in the effluent is observed. It should be noted that for the experiments discussed here, at 100% faradaic efficiency, 1 A cm^{-2} would result in a hydrogen recovery in excess of the theoretical maximum hydrogen yield based on the feed composition and flow rate. This suggests that the faradaic efficiency is less than unity for high current density conditions at least.

Broken membrane experiments were conducted in a single run, where the current was changed step-wise after measuring at each condition for at least 3 stable GC results. This provides useful insight about the transient response of the system. First, as seen in Fig. 6.8, the potential range in which this system operated was between 0 and 4 V. This is much higher than for the intact membrane due to the large contact resistance with the nickel current collector. The high contact

resistance also resulted in difficulty with controlling the reactor temperature, as much more heat was generated than was consumed. At high current densities the temperature of the furnace around the reactor was decreases as much as 150 ^{o}C to maintain the desired temperature around 790 ^{o}C inside the reactor. Fluctuations in potential made it difficult to maintain a stable temperature and resulted in temperature fluctuations at high current densities. These fluctuations in temperature can also be seen to cause proportional fluctuations in the effluent rates. At one point the temperature was allowed to decrease to 700 ^{o}C. The corresponding decrease in methane conversion and increase in CO_2 rates demonstrate the high sensitivity of the reaction to temperature changes. The intact membrane show much lower resistance and thus operates in a more isothermal manner, so these effects should be negligible for future experiments.

6.4 Conclusions

In this Chapter we discuss in detail, the design and deployment of the E-SMaRT-R system for investigating electrochemical reactions at high temperature and pressure with ion conductive ceramic membrane reactors. This system was designed from the ground up to allow for testing between 1 and 50 bar pressure, up to 900 ^{o}C temperature, and gas flow rates over 1000 SCCM. appropriate sensors and control equipment were selected to enable centralized control, along with data collection and handling through a LabVIEW based UI. The design of this system demonstrates the application of the first phase of the SM inspired framework for accelerating research in electrochemistry, and lays the foundation for efficient collection of large datasets to support the remaining phases of the framework.

Challenges faced during system startup included providing suitable electric isolation for the reactor, preventing steam condensation effects, and ensuring good contact between the membrane and the nickel current collector on the anode side of the membrane. electrical isolation was achieved by inserting sections of alumina tubing between the reactor and other components of

the system. Steam condensation in the pressure sensing lines was addressed by partially filling the lines to prevent the formation of discrete water droplets. Contact resistance between the membrane and the current collector was reduced by changing the assembly method during installation of the intact membrane.

After addressing these issues, the membrane performance was stabilized and current densities up to 1 A cm^{-2} were obtainable at cell potentials of less than 1 V. SMR was investigated with both a broken membrane assembly to provide benchmark measurements, and separation of hydrogen through the membrane was confirmed to result in shifting the equilibrium of the SMR reaction. Additional system characterization will help to further improve data collection and interpretation in this system, but these experiments show that the E-SMaRT-R system provides adequate control over the process conditions to begin gathering data for Phase 2 of the SM inspired framework.

Chapter 7

Conclusions

In this thesis, a framework for research, inspired by smart manufacturing (SM), is developed to accelerate discoveries in research directed toward technology scale-up. Specifically, the framework is developed in the context of scaling up electrochemical devices that have the potential to reshape the global energy landscape. These new technologies utilize highly complex interactions between mass, charge, and heat transport that affect the observed kinetics. Extracting the underlying relationships governing these interactions is difficult to accomplish using traditional research methods. Instead, a shift in experimental efforts towards collecting large datasets of high quality data can enable utilization of advanced computing techniques to help understand the complex interactions in electrochemical devices. This requires the design of appropriate experimental systems that facilitate automated data collection, management, and processing so that large reliable datasets can be collected from a variety of sensors. As such, this thesis not only provide the framework for implementing SM techniques to accelerate research, but also provides examples of how this framework can be applied in the lab.

Chapter 2 begins by presenting the framework and providing context for its application to electrochemistry, specifically electrochemical CO_2 reduction. This framework is composed of 4 distinct phases. In Phase 1, an appropriate reactor design is considered that allows SM principles

of automation and data connectivity to be implemented. This phase sets the foundation for the collection of large datasets that are then used in Phase 2 to extract underlying relationships using machine learning (ML) and artificial intelligence (AI) methods. Using intelligence provided by the ML and AI methods, control schemes are devised by which control of the reactor performance can be demonstrated to provide confidence in the models and identify gaps in knowledge. Finally in Phase 3, information gathered in the previous phases is incorporated in multi-scale modeling to develop a digital twin of the reactor system and to develop modeling techniques to describe the reactor performance on a more fundamental level. These models provide insight into the regions of the reactor that can not be probed experimentally, and the same methods developed for these models can be applied to the design of larger scale systems in Phase 4 to allow for *in silico* testing before construction.

In chapter 3, the first stage in the development of a CFD model for simulating electrochemical CO_2 reduction in the rotating cylinder electrode (RCE) reactor is discussed in detail. This stage of development focuses on establishing an accurate method of modeling hydrodynamics in the RCE and demonstrates how high quality experimental data can be used to validate simulation work. This simulation provides insights into the boundary layer conditions at the electrode surface and a better understanding of how the hydrodynamics can be used to control the mass transport of species reacting on the electrode surface. Key modeling techniques necessary to capture the hydrodynamics include using a $\kappa - \epsilon$ turbulence model with enhanced surface treatment. Also, not only must the mesh be refined enough at the surface to capture the hydrodynamics, but it must also capture the concentration gradient to accurately model mass transport at the electrode surface. Small stabilizing vortices that enhance mass transfer at the electrode surface are also identified providing a better understanding of how the system deviates from ideal conditions.

Chapter 4 continues the discussion for CFD modeling of the RCE in the second phase of the model development. Having established high quality modeling methods for the hydrodynamics, electrochemical reactions are introduced. Specifically, the hydrogen evolution reaction (HER)

which is ubiquitous to aqueous electrochemistry is used as a starting point for adding more complex chemical reactions. Motivation for the investigation of HER along with the addition of buffer reactions is provided by the fact that these reactions will be present in all aqueous electrochemical reactors. Challenges in modeling electrochemical reaction are primarily attributed to the non-linearity of the equations governing the current density in the reactor. While single reactions can be modeled successfully, Ansys Fluent software has difficulty converging on a solution when more than one multiple electrochemical reactions occur at appreciable rates. Regardless, successful simulation of kinetically limited water reduction and mass transfer limited reduction of protons are successfully modeled independently and the results provide insight about the electrochemical conditions at the electrode surface. A sinusoidal profile in the overpotential is observed in the azimuthal profile of the electrode while a hyperbolic function is observed in the axial profile. Current density distributions show that local current density can vary up to 25% from average for the mass transfer limited case, while the kinetically limited reaction is nearly uniform across the electrode surface. It is concluded that at low current density, the Ohmic loses are the primary cause of the potential profile, but have little effect on the current density profiles.

Chapter 5 changes pace by discussing recent efforts in the electrochemical activation of methane to produce fuels and chemicals. We propose that methane can act as an efficient carbon and hydrogen source during the transition away from fossil fuels as it provides a large energy benefit over water electrolysis for the production of hydrogen. Coupling methane with the production of ammonia requires the development of lower temperature conductive solid electrolytes to avoid ammonia decomposition and improve single pass conversion. Direct methane to methanol requires that the selectivity vs. conversion trade-off be addressed and that this technology could benefit from the development of highly efficient product separation process to allow system to operate at low conversion but high selectivity.

While most technologies discussed in chapter 5 are far from commercialization, the development of proton conducting $BaZr_{0.8-x-y}Ce_xY_yO_{3-\delta}$ (BZCY) ceramic membranes offers promising

new possibilities and proven performance. As such, this technology was identified as an excellent candidate for the application of the SM framework in Chapter 6. This chapter details the design and deployment of the Electrochemical Steam Methane Reforming Test Reactor (E-SMaRT-R) system. The E-SMaRT-R system was designed to allow testing of tubular ion conducting ceramics at pressures up to 50 bar and temperatures up to 900 ^{o}C while incorporating a high degree of automation for system operation, as well as data collection and management. Similar to the automation of the RCE reactor discussed in chapter 2, this system utilizes a LabVIEW based user interface that allows for centralized control over the system and data management. Automation methods such as a script to control changes of temperature or flow rates in the system at specific time intervals allow for semi-autonomous data collection of large datasets. This reactor is bench-marked against existing published performance metrics of a BZCY membrane provided by CoorsTek Membrane Sciences and experimental results show that electrochemical removal of hydrogen through the membrane during steam methane reforming does shift the chemical equilibrium of the reforming and water gas shift reaction toward complete conversion.

Overall this thesis provides a framework for applying SM methods to experimental electrochemical systems to accelerate the rate at which useful insights can be obtained. specifically, examples are provided for how multi-scale modeling is being used to expand our understanding of electrochemical reactions in the RCE and a smart reactor system is developed to utilize the SM inspired framework to investigate proton conducting membrane reactors at high temperature and pressure. In conclusion, the framework presented in this thesis, along with the discussion provided in the examples presented here, provide valuable insight about how SM techniques can be applied in the lab to accelerate research in the development of electrified chemical manufacturing processes.

Bibliography

[1] B. Walsh, P. Ciais, I. A. Janssens, J. Penuelas, K. Riahi, F. Rydzak, D. P. Van Vuuren, and M. Obersteiner. Pathways for balancing CO_2 emissions and sinks. *Nature communications*, 8(1):14856, 2017.

[2] A. A. Kebede, T. Kalogiannis, J. Van Mierlo, and M. Berecibar. A comprehensive review of stationary energy storage devices for large scale renewable energy sources grid integration. *Renewable and Sustainable Energy Reviews*, 159:112213, 2022.

[3] A. J. Bard, L. R. Faulkner, and H. S. White. *Electrochemical methods: Fundamentals and applications*. John Wiley & Sons, 2022.

[4] H. Malerød-Fjeld, D. Clark, I. Yuste-Tirados, R. Zanón, D. Catalán-Martinez, D. Beeaff, S. H. Morejudo, P. K. Vestre, T. Norby, R. Haugsrud, et al. Thermo-electrochemical production of compressed hydrogen from methane with near-zero energy loss. *Nature Energy*, 2(12):923–931, 2017.

[5] D. Richard, M. Tom, J. Jang, S. Yun, P. D. Christofides, and C. G. Morales-Guio. Quantifying transport and electrocatalytic reaction processes in a gastight rotating cylinder electrode reactor via integration of Computational Fluid Dynamics modeling and experiments. *Electrochimica Acta*, 440:141698, 2023.

[6] N. B. Watkins, Z. J. Schiffer, Y. Lai, C. B. I. Musgrave, H. A. Atwater, W. A. I. God-

dard, T. Agapie, J. C. Peters, and J. M. Gregoire. Hydrodynamics change tafel slopes in electrochemical CO_2 reduction on copper. *American Chemical Society Energy Letters*, 8: 2185–2192, 2023.

[7] J. Jang, M. Rüscher, M. Winzely, and C. G. Morales-Guio. Gastight rotating cylinder electrode: Toward decoupling mass transport and intrinsic kinetics in electrocatalysis. *American Institute of Chemical Engineering Journal*, 68(5):e17605, 2022.

[8] B. Rego de Vasconcelos and J.-M. Lavoie. Recent advances in power-to-x technology for the production of fuels and chemicals. *Frontiers in Chemistry*, 7:392, 2019.

[9] S. T. Wismann, J. S. Engbæk, S. B. Vendelbo, F. B. Bendixen, W. L. Eriksen, K. Aasberg-Petersen, C. Frandsen, I. Chorkendorff, and P. M. Mortensen. Electrified methane reforming: A compact approach to greener industrial hydrogen production. *Science*, 364(6442): 756–759, 2019.

[10] S. Madeddu, F. Ueckerdt, M. Pehl, J. Peterseim, M. Lord, K. A. Kumar, C. Krüger, and G. Luderer. The CO_2 reduction potential for the european industry via direct electrification of heat supply (power-to-heat). *Environmental Research Letters*, 15(12):124004, 2020.

[11] A. M. Brockway and P. Delforge. Emissions reduction potential from electric heat pumps in California homes. *The Electricity Journal*, 31(9):44–53, 2018.

[12] D. Gielen, D. Saygin, E. Taibi, and J.-P. Birat. Renewables-based decarbonization and relocation of iron and steel making: A case study. *Journal of Industrial Ecology*, 24(5): 1113–1125, 2020.

[13] S. Yuan, Y. Li, J. Peng, Y. M. Questell-Santiago, K. Akkiraju, L. Giordano, D. J. Zheng, S. Bagi, Y. Román-Leshkov, and Y. Shao-Horn. Conversion of methane into liquid fuels—Bridging thermal catalysis with electrocatalysis. *Advanced Energy Materials*, 10(40): 2002154, 2020.

[14] D. Richard, Y.-C. Huang, and C. G. Morales-Guio. Recent advances in the electrochemical production of chemicals from methane. *Current Opinion in Electrochemistry*, 30:100793, 2021.

[15] L. Arnarson, P. S. Schmidt, M. Pandey, A. Bagger, K. S. Thygesen, I. E. Stephens, and J. Rossmeisl. Fundamental limitation of electrocatalytic methane conversion to methanol. *Physical Chemistry Chemical Physics*, 20(16):11152–11159, 2018.

[16] C. Zhu, S. Hou, X. Hu, J. Lu, F. Chen, and K. Xie. Electrochemical conversion of methane to ethylene in a solid oxide electrolyzer. *Nature Communications*, 10(1):1173, 2019.

[17] A. A. Latimer, A. Kakekhani, A. R. Kulkarni, and J. K. Nørskov. Direct methane to methanol: The selectivity–conversion limit and design strategies. *American Chemical Society Catalysis*, 8(8):6894–6907, 2018.

[18] I. Garagounis, A. Vourros, D. Stoukides, D. Dasopoulos, and M. Stoukides. Electrochemical synthesis of ammonia: Recent efforts and future outlook. *Membranes*, 9(9):112, 2019.

[19] G. Wen, B. Ren, X. Wang, D. Luo, H. Dou, Y. Zheng, R. Gao, J. Gostick, A. Yu, and Z. Chen. Continuous CO_2 electrolysis using a CO_2 exsolution-induced flow cell. *Nature Energy*, 7:978–988, 2022.

[20] L. Chanussot, A. Das, S. Goyal, T. Lavril, M. Shuaibi, M. Riviere, K. Tran, J. Heras-Domingo, C. Ho, W. Hu, A. Palizhati, A. Sriram, B. Wood, J. Yoon, D. Parikh, C. L. Zitnick, and Z. Ulissi. Open Catalyst 2020 (OC20) dataset and community challenges. *American Chemical Society Catalysis*, 11(10):6059–6072, 2021.

[21] T. Mou, H. S. Pillai, S. Wang, M. Wan, X. Han, N. M. Schweitzer, F. Che, and H. Xin. Bridging the complexity gap in computational heterogeneous catalysis with machine learning. *Nature Catalysis*, 6(2):122–136, 2023.

[22] J. T. Margraf, H. Jung, C. Scheurer, and K. Reuter. Exploring catalytic reaction networks with machine learning. *Nature Catalysis*, 6:112–121, 2023.

[23] J. A. Esterhuizen, B. R. Goldsmith, and S. Linic. Interpretable machine learning for knowledge generation in heterogeneous catalysis. *Nature Catalysis*, 5(3):175–184, 2022.

[24] E. Taibi, H. Blanco, R. Miranda, and M. Carmo. Green hydrogen cost reduction-Scaling up electrolysers to meet the 1.5 ^{o}C climate goal. *International Renewable Energy Agency, Abu Dhabi*, 2020.

[25] R. Xia, S. Overa, and F. Jiao. Emerging electrochemical processes to decarbonize the chemical industry. *Journal of the American Chemical Society Au*, 2(5):1054–1070, 2022.

[26] G. H. Vogel. *Process Development, 1. Fundamentals and Standard Course*. John Wiley & Sons, Ltd, 2011.

[27] K. P. Kuhl, E. R. Cave, D. N. Abram, and T. F. Jaramillo. New insights into the electrochemical reduction of carbon dioxide on metallic copper surfaces. *Energy & Environmental Science*, 5(5):7050–7059, 2012.

[28] S. Nitopi, E. Bertheussen, S. B. Scott, X. Liu, A. K. Engstfeld, S. Horch, B. Seger, I. E. Stephens, K. Chan, C. Hahn, et al. Progress and perspectives of electrochemical CO_2 reduction on copper in aqueous electrolyte. *Chemical Reviews*, 119(12):7610–7672, 2019.

[29] J. Resasco, Y. Lum, E. Clark, J. Z. Zeledon, and A. T. Bell. Effects of Anion Identity and Concentration on Electrochemical Reduction of CO_2. *ChemElectroChem*, 5(7):1064–1072, 2018.

[30] Y. Hori, K. Kikuchi, and S. Suzuki. Production of CO and CH_4 in electrochemical reduction of CO_2 at metal electrodes in aqueous hydrogencarbonate solution. *Chemistry Letters*, 14 (11):1695–1698, 1985.

[31] J. Sobkowski, A. Wieckowski, P. Zelenay, and A. Czerwiński. Electrochemical reduction of CO_2 and oxidation of adsorbed species on the rhodium electrode. *Journal of Electroanalytical Chemistry and Interfacial Electrochemistry*, 100(1-2):781–790, 1979.

[32] Y. Hori and S. Suzuki. Electrolytic reduction of carbon dioxide at mercury electrode in aqueous solution. *Bulletin of the Chemical Society of Japan*, 55(3):660–665, 1982.

[33] Y. Hori, H. Wakebe, T. Tsukamoto, and O. Koga. Electrocatalytic process of CO selectivity in electrochemical reduction of CO_2 at metal electrodes in aqueous media. *Electrochimica Acta*, 39(11-12):1833–1839, 1994.

[34] Y. Hori, I. Takahashi, O. Koga, and N. Hoshi. Electrochemical reduction of carbon dioxide at various series of copper single crystal electrodes. *Journal of Molecular Catalysis A: Chemical*, 199(1-2):39–47, 2003.

[35] Q. Lu, J. Rosen, Y. Zhou, G. S. Hutchings, Y. C. Kimmel, J. G. Chen, and F. Jiao. A selective and efficient electrocatalyst for carbon dioxide reduction. *Nature communications*, 5(1):3242, 2014.

[36] R. Kas, R. Kortlever, A. Milbrat, M. T. Koper, G. Mul, and J. Baltrusaitis. Electrochemical CO_2 reduction on Cu_2O-derived copper nanoparticles: Controlling the catalytic selectivity of hydrocarbons. *Physical Chemistry Chemical Physics*, 16(24):12194–12201, 2014.

[37] R. Kortlever, I. Peters, S. Koper, and M. T. Koper. Electrochemical CO_2 reduction to formic acid at low overpotential and with high faradaic efficiency on carbon-supported bimetallic Pd–Pt nanoparticles. *American Chemical Society Catalysis*, 5(7):3916–3923, 2015.

[38] H. B. Yang, S.-F. Hung, S. Liu, K. Yuan, S. Miao, L. Zhang, X. Huang, H.-Y. Wang, W. Cai, R. Chen, et al. Atomically dispersed Ni (I) as the active site for electrochemical CO_2 reduction. *Nature Energy*, 3(2):140–147, 2018.

[39] K. Jiang, R. B. Sandberg, A. J. Akey, X. Liu, D. C. Bell, J. K. Nørskov, K. Chan, and H. Wang. Metal ion cycling of Cu foil for selective C–C coupling in electrochemical CO_2 reduction. *Nature Catalysis*, 1(2):111–119, 2018.

[40] F. Pan, B. Li, W. Deng, Z. Du, Y. Gang, G. Wang, and Y. Li. Promoting electrocatalytic CO_2 reduction on nitrogen-doped carbon with sulfur addition. *Applied Catalysis B: Environmental*, 252:240–249, 2019.

[41] K. Manthiram, B. J. Beberwyck, and A. P. Alivisatos. Enhanced electrochemical methanation of carbon dioxide with a dispersible nanoscale copper catalyst. *Journal of the American Chemical Society*, 136(38):13319–13325, 2014.

[42] T. Hatsukade, K. P. Kuhl, E. R. Cave, D. N. Abram, and T. F. Jaramillo. Insights into the electrocatalytic reduction of CO_2 on metallic silver surfaces. *Physical Chemistry Chemical Physics*, 16(27):13814–13819, 2014.

[43] S. Y. Lee, H. Jung, N.-K. Kim, H.-S. Oh, B. K. Min, and Y. J. Hwang. Mixed copper states in anodized Cu electrocatalyst for stable and selective ethylene production from CO_2 reduction. *Journal of the American Chemical Society*, 140(28):8681–8689, 2018.

[44] K. Hara, A. Tsuneto, A. Kudo, and T. Sakata. Electrochemical reduction of CO_2 on a Cu electrode under high pressure: Factors that determine the product selectivity. *Journal of the Electrochemical Society*, 141(8):2097, 1994.

[45] R. Kas, R. Kortlever, H. Yılmaz, M. T. Koper, and G. Mul. Manipulating the hydrocarbon selectivity of copper nanoparticles in CO_2 electroreduction by process conditions. *ChemElectroChem*, 2(3):354–358, 2015.

[46] K. Hara and T. Sakata. Large current density CO_2 reduction under high pressure using gas diffusion electrodes. *Bulletin of the Chemical Society of Japan*, 70(3):571–576, 1997.

[47] S. Narayanan, B. Haines, J. Soler, and T. Valdez. Electrochemical conversion of carbon dioxide to formate in alkaline polymer electrolyte membrane cells. *Journal of The Electrochemical Society*, 158(2):A167, 2010.

[48] J. Albo, G. Beobide, P. Castaño, and A. Irabien. Methanol electrosynthesis from CO_2 at Cu_2O/ZnO prompted by pyridine-based aqueous solutions. *Journal of CO_2 Utilization*, 18: 164–172, 2017.

[49] D. A. Salvatore, D. M. Weekes, J. He, K. E. Dettelbach, Y. C. Li, T. E. Mallouk, and C. P. Berlinguette. Electrolysis of gaseous CO_2 to CO in a flow cell with a bipolar membrane. *American Chemical Society Energy Letters*, 3(1):149–154, 2017.

[50] C.-T. Dinh, T. Burdyny, M. G. Kibria, A. Seifitokaldani, C. M. Gabardo, F. P. García de Arquer, A. Kiani, J. P. Edwards, P. De Luna, O. S. Bushuyev, et al. CO_2 electroreduction to ethylene via hydroxide-mediated copper catalysis at an abrupt interface. *Science*, 360 (6390):783–787, 2018.

[51] S. Ren, D. Joulié, D. Salvatore, K. Torbensen, M. Wang, M. Robert, and C. P. Berlinguette. Molecular electrocatalysts can mediate fast, selective CO_2 reduction in a flow cell. *Science*, 365(6451):367–369, 2019.

[52] J. Lee, J. Lim, C.-W. Roh, H. S. Whang, and H. Lee. Electrochemical CO_2 reduction using alkaline membrane electrode assembly on various metal electrodes. *Journal of CO_2 Utilization*, 31:244–250, 2019.

[53] F. P. García de Arquer, C.-T. Dinh, A. Ozden, J. Wicks, C. McCallum, A. R. Kirmani, D.-H. Nam, C. Gabardo, A. Seifitokaldani, X. Wang, et al. CO_2 electrolysis to multicarbon products at activities greater than 1 A cm^{-2}. *Science*, 367(6478):661–666, 2020.

[54] D. T. Whipple, E. C. Finke, and P. J. Kenis. Microfluidic reactor for the electrochemical

reduction of carbon dioxide: The effect of pH. *Electrochemical and Solid-State Letters*, 13 (9):B109, 2010.

[55] B. A. Rosen, A. Salehi-Khojin, M. R. Thorson, W. Zhu, D. T. Whipple, P. J. Kenis, and R. I. Masel. Ionic liquid-mediated selective conversion of CO_2 to CO at low overpotentials. *Science*, 334(6056):643–644, 2011.

[56] S. Ma, M. Sadakiyo, R. Luo, M. Heima, M. Yamauchi, and P. J. Kenis. One-step electrosynthesis of ethylene and ethanol from CO_2 in an alkaline electrolyzer. *Journal of Power Sources*, 301:219–228, 2016.

[57] Z. Zhan, W. Kobsiriphat, J. R. Wilson, M. Pillai, I. Kim, and S. A. Barnett. Syngas production by coelectrolysis of CO_2/H_2O: The basis for a renewable energy cycle. *Energy & Fuels*, 23(6):3089–3096, 2009.

[58] K. Xie, Y. Zhang, G. Meng, and J. T. Irvine. Electrochemical reduction of CO_2 in a proton conducting solid oxide electrolyser. *Journal of Materials Chemistry*, 21(1):195–198, 2011.

[59] L. Yu, J. Wang, X. Hu, Z. Ye, C. Buckley, and D. Dong. A nanocatalyst network for electrochemical reduction of CO_2 over microchanneled solid oxide electrolysis cells. *Electrochemistry Communications*, 86:72–75, 2018.

[60] E. L. Clark, M. R. Singh, Y. Kwon, and A. T. Bell. Differential electrochemical mass spectrometer cell design for online quantification of products produced during electrochemical reduction of CO_2. *Analytical chemistry*, 87(15):8013–8020, 2015.

[61] E. L. Clark and A. T. Bell. Direct observation of the local reaction environment during the electrochemical reduction of CO_2. *Journal of the American Chemical Society*, 140(22): 7012–7020, 2018.

[62] A. Murata and Y. Hori. Product selectivity affected by cationic species in electrochemical reduction of CO_2 and CO at a Cu electrode. *Bulletin of the Chemical Society of Japan*, 64 (1):123–127, 1991.

[63] J. Resasco, L. D. Chen, E. Clark, C. Tsai, C. Hahn, T. F. Jaramillo, K. Chan, and A. T. Bell. Promoter effects of alkali metal cations on the electrochemical reduction of carbon dioxide. *Journal of the American Chemical Society*, 139(32):11277–11287, 2017.

[64] C. Hahn, T. Hatsukade, Y.-G. Kim, A. Vailionis, J. H. Baricuatro, D. C. Higgins, S. A. Nitopi, M. P. Soriaga, and T. F. Jaramillo. Engineering Cu surfaces for the electrocatalytic conversion of CO_2: Controlling selectivity toward oxygenates and hydrocarbons. *Proceedings of the National Academy of Sciences*, 114(23):5918–5923, 2017.

[65] J. J. Kim, D. P. Summers, and K. W. Frese. Reduction of carbon dioxide and carbon monoxide to methane on copper foil electrodes. *Journal of Electroanalytical Chemistry and Interfacial Electrochemistry*, 245(1-2):223–244, 1988.

[66] C. Leiva. First principles of smart manufacturing. *Journal of Advanced Manufacturing and Processing*, 4:e10123, 2022.

[67] N. Tuptuk and S. Hailes. Security of smart manufacturing systems. *Journal of Manufacturing Systems*, 47:93–106, 2018.

[68] B. Burnak, N. A. Diangelakis, J. Katz, and E. N. Pistikopoulos. Integrated process design, scheduling, and control using multiparametric programming. *Computers & Chemical Engineering*, 125:164–184, 2019.

[69] J. Davis, H. Malkani, J. Dyck, P. Korambath, and J. Wise. Chapter 4 - Cyberinfrastructure for the democratization of smart manufacturing. In *Smart Manufacturing: Concepts and Methods*, pages 83–116. Elsevier, 2020.

[70] J. Davis. Smart manufacturing. In M. A. Abraham, editor, *Encyclopedia of Sustainable Technologies*, pages 417–427. Elsevier, Oxford, 2017.

[71] S. Phuyal, D. Bista, and R. Bista. Challenges, opportunities and future directions of smart manufacturing: A state of art review. *Sustainable Futures*, 2:100023, 2020.

[72] B. Burnak, N. A. Diangelakis, and E. N. Pistikopoulos. Towards the grand unification of process design, scheduling, and control - Utopia or reality? *Processes*, 7(7):461, 2019.

[73] Y.-J. Lin, S.-H. Wei, and C.-Y. Huang. Intelligent manufacturing control systems: The core of smart factory. *Procedia Manufacturing*, 39:389–397, 2019.

[74] J. Prior, M. Bartelt, J. Sinnemann, and B. Kuhlenkötter. Investigation of the automation capability of electrolyzers production. *Procedia CIRP*, 107:718–723, 2022.

[75] M. Bogojeski, S. Sauer, F. Horn, and K.-R. Müller. Forecasting industrial aging processes with machine learning methods. *Computers & Chemical Engineering*, 144:107123, 2021.

[76] B. Çıtmacı, J. Luo, J. B. Jang, V. Canuso, D. Richard, Y. M. Ren, C. G. Morales-Guio, and P. D. Christofides. Machine learning-based ethylene concentration estimation, real-time optimization and feedback control of an experimental electrochemical reactor. *Chemical Engineering Research and Design*, 185:87–107, 2022.

[77] A. S. Kumar and Z. Ahmad. Model predictive control (MPC) and its current issues in chemical engineering. *Chemical Engineering Communications*, 199(4):472–511, 2012.

[78] Y. Ding, L. Wang, Y. Li, and D. Li. Model predictive control and its application in agriculture: A review. *Computers and Electronics in Agriculture*, 151:104–117, 2018.

[79] A. Kumar, M. Baldea, T. F. Edgar, and O. A. Ezekoye. Smart manufacturing approach for efficient operation of industrial steam-methane reformers. *Industrial & Engineering Chemistry Research*, 54(16):4360–4370, 2015.

[80] H. Malkani and P. Korambath. Clean energy smart manufacturing institute (CESMII) special issue. *Journal of Advanced Manufacturing and Processing*, 4(4):e10146, 2022.

[81] Z. Brunner. Manufacturing USA highlights report 2022. Technical report, National Institute of Standards and Technology, 2022.

[82] N. S. Arden, A. C. Fisher, K. Tyner, L. X. Yu, S. L. Lee, and M. Kopcha. Industry 4.0 for pharmaceutical manufacturing: Preparing for the smart factories of the future. *International Journal of Pharmaceutics*, 602:120554, 2021.

[83] B. Vogel-Heuser, S. Rösch, A. Martini, and M. Tichy. Technical debt in automated production systems. In *2015 IEEE 7th International Workshop on Managing Technical Debt (MTD)*, pages 49–52. IEEE, 2015.

[84] A. Martini and J. Bosch. *Architectural technical debt in embedded systems*, chapter 4, pages 77–103. John Wiley & Sons, Ltd, 2019.

[85] A. Kravchenko. Workforce training and management challenges in the contemporary smart manufacturing (SM). *Intellectual Archive*, 8(2):59–65, 2019.

[86] B. Çıtmacı, J. Luo, J. B. Jang, P. Korambath, C. G. Morales-Guio, J. F. Davis, and P. D. Christofides. Digitalization of an experimental electrochemical reactor via the smart manufacturing innovation platform. *Digital Chemical Engineering*, 5:100050, 2022.

[87] V. G. Pangarkar. *Design of multiphase reactors*, chapter 5. John Wiley & Sons, 2014.

[88] M. Abolhasani and E. Kumacheva. The rise of self-driving labs in chemical and materials sciences. *Nature Synthesis*.

[89] A. Vriza, H. Chan, and J. Xu. Self-driving laboratory for polymer electronics. *Chemistry of Materials*, 35(8):3046–3056, 2023.

[90] S. M. Mennen, C. Alhambra, C. L. Allen, M. Barberis, S. Berritt, T. A. Brandt, A. D. Campbell, J. Castañón, A. H. Cherney, M. Christensen, et al. The evolution of high-throughput experimentation in pharmaceutical development and perspectives on the future. *Organic Process Research & Development*, 23(6):1213–1242, 2019.

[91] H. Tao, T. Wu, S. Kheiri, M. Aldeghi, A. Aspuru-Guzik, and E. Kumacheva. Self-driving platform for metal nanoparticle synthesis: Combining microfluidics and machine learning. *Advanced Functional Materials*, 31(51):2106725, 2021.

[92] B. Çıtmacı, J. Luo, J. B. Jang, C. G. Morales-Guio, and P. D. Christofides. Machine learning-based ethylene and carbon monoxide estimation, real-time optimization, and multivariable feedback control of an experimental electrochemical reactor. *Chemical Engineering Research and Design*, 191:658–681, 2023.

[93] B. R. Goldsmith, J. Esterhuizen, J.-X. Liu, C. J. Bartel, and C. Sutton. Machine learning for heterogeneous catalyst design and discovery. *American Institute of Chemical Engineering Journal*, 64(9):3553–3553, 2018.

[94] A. Angulo, L. Yang, E. S. Aydil, and M. A. Modestino. Machine learning enhanced spectroscopic analysis: Towards autonomous chemical mixture characterization for rapid process optimization. *Digital Discovery*, 1(1):35–44, 2022.

[95] B. P. MacLeod, F. G. Parlane, T. D. Morrissey, F. Häse, L. M. Roch, K. E. Dettelbach, R. Moreira, L. P. Yunker, M. B. Rooney, J. R. Deeth, et al. Self-driving laboratory for accelerated discovery of thin-film materials. *Science Advances*, 6(20):eaaz8867, 2020.

[96] B. J. Reizman and K. F. Jensen. An automated continuous-flow platform for the estimation of multistep reaction kinetics. *Organic Process Research & Development*, 16(11):1770–1782, 2012.

[97] J. Luo, V. Canuso, J. B. Jang, Z. Wu, C. G. Morales-Guio, and P. D. Christofides. Machine learning-based operational modeling of an electrochemical reactor: Handling data variability and improving empirical models. *Industrial & Engineering Chemistry Research*, 61: 8399–8410, 2022.

[98] Z. Wu, A. Tran, D. Rincon, and P. D. Christofides. Machine learning-based predictive control of nonlinear processes Part I: Theory. *American Institute of Chemical Engineering Journal*, 65(11):e16729, 2019.

[99] Z. Wu, J. Luo, D. Rincon, and P. D. Christofides. Machine learning-based predictive control using noisy data: Evaluating performance and robustness via a large-scale process simulator. *Chemical Engineering Research and Design*, 168:275–287, 2021.

[100] M. A. Xavier and M. S. Trimboli. Lithium-ion battery cell-level control using constrained model predictive control and equivalent circuit models. *Journal of Power Sources*, 285: 374–384, 2015.

[101] M. Denn. *Process Fluid Mechanics*. Prentice-Hall international series in the physical and chemical engineering sciences. Prentice-Hall, 1980.

[102] S. Santhanagopalan. *Encyclopedia of Applied Electrochemistry*, chapter Electrochemical Systems - Scaling, Dimensionless Groups, pages 634–640. Springer New York, 2014.

[103] M. W. Oppenheimer, D. B. Doman, and J. D. Merrick. Multi-scale physics-informed machine learning using the Buckingham Pi theorem. *Journal of Computational Physics*, 474: 111810, 2023.

[104] X. Xie, A. Samaei, J. Guo, W. K. Liu, and Z. Gan. Data-driven discovery of dimensionless numbers and governing laws from scarce measurements. *Nature Communications*, 13(1): 7562, 2022.

[105] H. Chen, C. Batchelor-McAuley, E. Kätelhön, J. Elliott, and R. G. Compton. A critical evaluation of using physics-informed neural networks for simulating voltammetry: Strengths, weaknesses and best practices. *Journal of Electroanalytical Chemistry*, 925(June):116918, 2022.

[106] Y.-J. Tu, S. Delmerico, and J. G. McDaniel. Inner layer capacitance of organic electrolytes from constant voltage molecular dynamics. *The Journal of Physical Chemistry C*, 124(5): 2907–2922, 2020.

[107] S. Kong, X. Lv, X. Wang, Z. Liu, Z. Li, B. Jia, D. Sun, C. Yang, L. Liu, A. Guan, et al. Delocalization state-induced selective bond breaking for efficient methanol electrosynthesis from CO_2. *Nature Catalysis*, 6:6–15, 2022.

[108] D. Micale, C. Ferroni, R. Uglietti, M. Bracconi, and M. Maestri. Computational fluid dynamics of reacting flows at surfaces: Methodologies and applications. *Chemie Ingenieur Technik*, 94(5):634–651, 2022.

[109] L.-T. Zhu, X.-Z. Chen, B. Ouyang, W.-C. Yan, H. Lei, Z. Chen, and Z.-H. Luo. Review of machine learning for hydrodynamics, transport, and reactions in multiphase flows and reactors. *Industrial & Engineering Chemistry Research*, 61:9901–9949, 2022.

[110] The World Bank. Fossil fuel energy consumption (% of total). `https://data.worldbank.org/indicator/EG.USE.COMM.FO.ZS`, 2014.

[111] P. D. Luna, C. Hahn, D. Higgins, S. A. Jaffer, T. F. Jaramillo, and E. H. Sargent. What would it take for renewably powered electrosynthesis to displace petrochemical processes? *Science*, 364(6438):eaav3506, 2019.

[112] J. Newman and N. P. Balsara. *Electrochemical systems*. John Wiley & Sons, 2021.

[113] F. Walsh, G. Kear, A. Nahlé, J. Wharton, and L. Arenas. The rotating cylinder electrode for studies of corrosion engineering and protection of metals—An illustrated review. *Corrosion Science*, 123:1–20, 2017.

[114] C. J. Low, C. P. de Leon, and F. C. Walsh. The rotating cylinder electrode (RCE) and its application to the electrodeposition of metals. *Australian Journal of Chemistry*, 58(4):246–262, 2005.

[115] J. Newman. Current distribution on a rotating disk below the limiting current. *Journal of The Electrochemical Society*, 113(12):1235, dec 1966.

[116] D. Clark, H. Malerød-Fjeld, M. Budd, I. Yuste-Tirados, D. Beeaff, S. Aamodt, K. Nguyen, L. Ansaloni, T. Peters, P. K. Vestre, D. K. Pappas, M. I. Valls, S. Remiro-Buenamañana, T. Norby, T. S. Bjørheim, J. M. Serra, and C. Kjølseth. Single-step hydrogen production from NH_3, CH_4, and biogas in stacked proton ceramic reactors. *Science*, 376(6591):390–393, 2022.

[117] T. Mizushina. The electrochemical method in transport phenomena. *Advances in Heat Transfer*, 7:87–161, 1971.

[118] J. R. Selman and C. W. Tobias. Mass-transfer measurements by the limiting-current technique. *Advances in Chemical Engineering*, 10:211–318, 1978.

[119] M. Eisenberg, C. W. Tobias, and C. R. Wilke. Ionic mass transfer and concentration polarization at rotating electrodes. *Journal of the Electrochemical Society*, 101(6):306–320, 1954.

[120] D. C. Silverman. The rotating cylinder electrode for examining velocity-sensitive corrosion-A review. *Corrosion*, 60(11):1003–1023, 2004.

[121] J. Selman and J. McClure. Limiting current to a vertical rotating rod electrode. *Journal of Electroanalytical Chemistry and Interfacial Electrochemistry*, 110(1):79–92, 1980.

[122] V. G. Levich. *Physicochemical hydrodynamics*. Prentice-Hall Inc., 1962.

[123] K. P. Griffin, L. Fu, and P. Moin. Velocity transformation for compressible wall-bounded turbulent flows with and without heat transfer. *Proceedings of the National Academy of Sciences*, 118(34):e2111144118, 2021.

[124] S. Vijay, W. Ju, S. Brückner, S.-C. Tsang, P. Strasser, and K. Chan. Unified mechanistic understanding of CO_2 reduction to CO on transition metal and single atom catalysts. *Nature Catalysis*, 4(12):1024–1031, 2021.

[125] G. Bauer, P. Gamnitzer, V. Gravemeier, and W. A. Wall. An isogeometric variational multiscale method for large-eddy simulation of coupled multi-ion transport in turbulent flow. *Journal of Computational Physics*, 251:194–208, 2013.

[126] P. Van Shaw and T. J. Hanratty. Fluctuations in the local rate of turbulent mass transfer to a pipe wall. *American Institute of Chemical Engineering Journal*, 10(4):475–482, 1964.

[127] D. Matić, B. Lovreček, and D. Skansi. The rotating cylinder electrode. *Journal of Applied Electrochemistry*, 8(5):391–398, 1978.

[128] ANSYS. *Ansys Fluent Theory Guide*. ANSYS Inc., Canonsburg, PA, 2022.

[129] B. E. Launder and N. D. Sandham. *Closure Strategies for Turbulent and Transitional Flows*. Cambridge University Press, 2002.

[130] T.-H. Shih, W. W. Liou, A. Shabbir, Z. Yang, and J. Zhu. A new $k-\epsilon$ eddy viscosity model for high reynolds number turbulent flows. *Computers & Fluids*, 24(3):227–238, 1995.

[131] M. Wolfshtein. The velocity and temperature distribution in one-dimensional flow with turbulence augmentation and pressure gradient. *International Journal of Heat and Mass Transfer*, 12(3):301–318, 1969.

[132] H. C. Chen and V. C. Patel. Near-wall turbulence models for complex flows including separation. *American Institute of Aeronautics and Astronautics Journal*, 26(6):641–648, 1988.

[133] T. Jongen and Y. Marx. Design of an unconditionally stable, positive scheme for the $k - \epsilon$ and two-layer turbulence models. *Computers & Fluids*, 26(5):469–487, 1997.

[134] F. White and G. Christoph. A simple new analysis of compressible turbulent two-dimensional skin friction under arbitrary conditions. Technical report, University of Rhode Island, Kingston, Department of Mechanical Engineering and Applied Mechanics, 1971.

[135] P. G. Huang, P. Bradshaw, and T. J. Coakley. Skin friction and velocity profile family for compressible turbulent boundary layers. *American Institute of Aeronautics and Astronautics Journal*, 31(9):1600–1604, 1993.

[136] B. Kader. Temperature and concentration profiles in fully turbulent boundary layers. *International Journal of Heat and Mass Transfer*, 24(9):1541–1544, 1981.

[137] W. Haynes. *CRC Handbook of Chemistry and Physics*. CRC Press, 2016.

[138] M. Eisenberg, C. Tobias, and C. Wilke. Mass transfer in electrode processes. 2. Mass transfer at rotating cylinders. Technical report, University of California, Berkeley, Department of Chemistry and Chemical Engineering, 1953.

[139] D. R. Gabe, G. Wilcox, J. Gonzalez-Garcia, and F. Walsh. The rotating cylinder electrode: Its continued development and application. *Journal of Applied Electrochemistry*, 28(8): 759–780, 1998.

[140] C. D. Andereck, S. S. Liu, and H. L. Swinney. Flow regimes in a circular couette system with independently rotating cylinders. *Journal of Fluid Mechanics*, 164:155–183, 1986.

[141] M. Sprague, P. Weidman, S. Macumber, and P. Fischer. Tailored taylor vortices. *Physics of Fluids*, 20(1):014102, 2008.

[142] E. Rivero, P. Granados, F. Rivera, M. Cruz, and I. González. Mass transfer modeling and simulation at a rotating cylinder electrode (RCE) reactor under turbulent flow for copper recovery. *Chemical Engineering Science*, 65(10):3042–3049, 2010.

[143] R. Srinivasan, S. Jayanti, and A. Kannan. Effect of taylor vortices on mass transfer from a rotating cylinder. *American Institute of Chemical Engineering Journal*, 51(11):2885–2898, 2005.

[144] F. J. Almazán-Ruiz, F. V. Caballero, M. R. Cruz-Díaz, E. P. Rivero, and I. González. Scale-up of rotating cylinder electrode electrochemical reactor for Cu(II) recovery: Experimental and simulation study in turbulence regimen. *Electrochimica Acta*, 77:262–271, 2012.

[145] T. Perez and J. Nava. Simulation of turbulent flow of a rotating cylinder electrode. Influence of using plates and concentric cylinder as counter electrodes. *International Journal of Electrochemical Science*, 8:4690–4699, 04 2013.

[146] W. S. Saric. Görtler vortices. *Annual Review of Fluid Mechanics*, 26(1):379–409, 1994.

[147] T. Wei, E. M. Kline, S. H.-K. Lee, and S. Woodruff. Görtler vortex formation at the inner cylinder in taylor–couette flow. *Journal of Fluid Mechanics*, 245:47–68, 1992.

[148] F. Bao, E. Kemppainen, I. Dorbandt, R. Bors, F. Xi, R. Schlatmann, R. van de Krol, and S. Calnan. Understanding the hydrogen evolution reaction kinetics of electrodeposited nickel-molybdenum in acidic, near-neutral, and alkaline conditions. *ChemElectroChem*, 8(1):195–208, 2021.

[149] I. Katsounaros, J. C. Meier, S. O. Klemm, A. A. Topalov, P. U. Biedermann, M. Auinger, and K. J. Mayrhofer. The effective surface pH during reactions at the solid-liquid interface. *Electrochemistry Communications*, 13(6):634–637, 2011.

[150] M. N. Jackson, O. Jung, H. C. Lamotte, and Y. Surendranath. Donor-dependent promotion of interfacial proton-coupled electron transfer in aqueous electrocatalysis. *American Chemical Society Catalysis*, 9(4):3737–3743, 2019.

[151] C.-O. Danielsson, A. Dahlkild, A. Velin, and M. Behm. A model for the enhanced water dissociation on monopolar membranes. *Electrochimica Acta*, 54(11):2983–2991, 2009.

[152] A. N. Colli and J. M. Bisang. Tertiary current and potential distribution including laminar/turbulent convection, diffusion, and migration by the finite volume method using openfoam. *Industrial & Engineering Chemistry Research*, 60(32):11927–11941, 2021.

[153] Y. D. Gamburg and G. Zangari. *Theory and practice of metal electrodeposition*. Springer Science & Business Media, 2011.

[154] Energy Information Administration. US Energy Information Administration annual energy outlook 2020. *US Department of Energy: Washington, DC, USA*, 2020.

[155] M. R. Edwards and J. E. Trancik. Climate impacts of energy technologies depend on emissions timing. *Nature Climate Change*, 4(5):347–352, 2014.

[156] Energy Transitions Commission et al. Mission possible: Reaching net-zero carbon emissions from harder-to-abate sectors by mid-century. *Energy Transitions Commission*, 2018.

[157] E. Elhacham, L. Ben-Uri, J. Grozovski, Y. M. Bar-On, and R. Milo. Global human-made mass exceeds all living biomass. *Nature*, 588(7838):442–444, 2020.

[158] M. Brudermüller. How to build a more climate-friendly chemical industry. In *World Economic Forum, Annual Meeting*, 2020.

[159] D. W. Keith, G. Holmes, D. S. Angelo, and K. Heidel. A process for capturing CO_2 from the atmosphere. *Joule*, 2(8):1573–1594, 2018.

[160] W. Falter, A. Langer, F. Wesche, and S. Wezel. Decarbonization strategies in converging chemical and energy markets. *Journal of Business Chemistry*, 17:20–40, 2020.

[161] J.-Y. Joo, S. Raghavan, and Z. Sun. Integration of sustainable manufacturing systems into smart grids with high penetration of renewable energy resources. In *2016 IEEE Green Technologies Conference (GreenTech)*, pages 12–17. IEEE, 2016.

[162] Innovation, mission: Accelerating breakthrough innovation in carbon capture, utilization, and storage. In *Report of the Mission Innovation Carbon Capture, Utilization, and Storage Experts' Workshop*, 2017.

[163] Y. T. Shah. *Hybrid energy systems: Strategy for industrial decarbonization*. CRC Press, 2021.

[164] R. M. Perkin. Electrically generated heat. *Ullmann's Encyclopedia of Industrial Chemistry*, 2000.

[165] T. Mai, D. Steinberg, J. Logan, D. Bielen, K. Eurek, and C. McMillan. An electrified future: Initial scenarios and future research for US energy and electricity systems. *IEEE Power and Energy Magazine*, 16(4):34–47, 2018.

[166] V. V. Welborn, L. Ruiz Pestana, and T. Head-Gordon. Computational optimization of electric fields for better catalysis design. *Nature Catalysis*, 1(9):649–655, 2018.

[167] S. Ringe, C. G. Morales-Guio, L. D. Chen, M. Fields, T. F. Jaramillo, C. Hahn, and K. Chan. Double layer charging driven carbon dioxide adsorption limits the rate of electrochemical carbon dioxide reduction on gold. *Nature communications*, 11(1):33, 2020.

[168] V. Kyriakou, I. Garagounis, A. Vourros, E. Vasileiou, and M. Stoukides. An electrochemical haber-bosch process. *Joule*, 4(1):142–158, 2020.

[169] C. Smith, A. K. Hill, and L. Torrente-Murciano. Current and future role of haber–bosch ammonia in a carbon-free energy landscape. *Energy & Environmental Science*, 13(2):331–344, 2020.

[170] S. T. Wismann, J. S. Engbæk, S. B. Vendelbo, W. L. Eriksen, C. Frandsen, P. M. Mortensen, and I. Chorkendorff. Electrified methane reforming: Understanding the dynamic interplay. *Industrial & Engineering Chemistry Research*, 58(51):23380–23388, 2019.

[171] J. Jang, K. Shen, and C. G. Morales-Guio. Electrochemical direct partial oxidation of methane to methanol. *Joule*, 3(11):2589–2593, 2019.

[172] A. H. B. Mostaghimi, T. A. Al-Attas, M. G. Kibria, and S. Siahrostami. A review on electrocatalytic oxidation of methane to oxygenates. *Journal of Materials Chemistry A*, 8 (31):15575–15590, 2020.

[173] M. Appl. Ammonia, 2. production processes. *Ullmann's Encyclopedia of Industrial Chemistry*, 2011.

[174] A. P. Simpson and A. E. Lutz. Exergy analysis of hydrogen production via steam methane reforming. *International Journal of Hydrogen Energy*, 32(18):4811–4820, 2007.

[175] B. Chen, Z. Liao, J. Wang, H. Yu, and Y. Yang. Exergy analysis and CO_2 emission evaluation for steam methane reforming. *International Journal of Hydrogen energy*, 37(4):3191–3200, 2012.

[176] X. Peng. Analysis of the thermal efficiency limit of the steam methane reforming process. *Industrial & Engineering Chemistry Research*, 51(50):16385–16392, 2012.

[177] A. A. Latimer, H. Aljama, A. Kakekhani, J. S. Yoo, A. Kulkarni, C. Tsai, M. Garcia-Melchor, F. Abild-Pedersen, and J. K. Nørskov. Mechanistic insights into heterogeneous methane activation. *Physical Chemistry Chemical Physics*, 19(5):3575–3581, 2017.

[178] J. N. Jocz, A. J. Medford, and C. Sievers. Thermodynamic limitations of the catalyst design space for methanol production from methane. *ChemCatChem*, 11(1):593–600, 2019.

[179] W. Deibert, M. E. Ivanova, S. Baumann, O. Guillon, and W. A. Meulenberg. Ion-conducting ceramic membrane reactors for high-temperature applications. *Journal of membrane science*, 543:79–97, 2017.

[180] C. Duan, R. Kee, H. Zhu, N. Sullivan, L. Zhu, L. Bian, D. Jennings, and R. O'Hayre. Highly efficient reversible protonic ceramic electrochemical cells for power generation and fuel production. *Nature Energy*, 4(3):230–240, 2019.

[181] J. C. Fornaciari, D. Primc, K. Kawashima, B. R. Wygant, S. Verma, L. Spanu, C. B. Mullins, A. T. Bell, and A. Z. Weber. A perspective on the electrochemical oxidation of methane to methanol in membrane electrode assemblies. *American Chemical Society Energy Letters*, 5 (9):2954–2963, 2020.

[182] P. Promoppatum and V. Viswanathan. Identifying material and device targets for a flare gas recovery system utilizing electrochemical conversion of methane to methanol. *American Chemical Society Sustainable Chemistry & Engineering*, 4(3):1736–1745, 2016.

[183] T. Liu, H. Liu, X. Zhang, L. Lei, Y. Zhang, Z. Yuan, F. Chen, and Y. Wang. A robust solid oxide electrolyzer for highly efficient electrochemical reforming of methane and steam. *Journal of Materials Chemistry A*, 7(22):13550–13558, 2019.

[184] Y. Tong, X. Meng, T. Luo, C. Cui, Y. Wang, S. Wang, R. Peng, B. Xie, C. Chen, and Z. Zhan. Protonic ceramic electrochemical cell for efficient separation of hydrogen. *American Chemical Society applied materials & interfaces*, 12(23):25809–25817, 2020.

[185] M. E. O'Reilly, R. S. Kim, S. Oh, and Y. Surendranath. Catalytic methane monofunctionalization by an electrogenerated high-valent Pd intermediate. *American Chemical Society Central Science*, 3(11):1174–1179, 2017.

[186] M. Farnak, J. Esfahani, and S. Bozorgmehri. An experimental design of the solid oxide fuel cell performance by using partially oxidation reforming of natural gas. *Renewable Energy*, 147:155–163, 2020.

[187] J. Lu, C. Zhu, C. Pan, W. Lin, J. P. Lemmon, F. Chen, C. Li, and K. Xie. Highly efficient electrochemical reforming of CH4/CO_2 in a solid oxide electrolyser. *Science advances*, 4 (3):eaar5100, 2018.

[188] B. Lee and T. Hibino. Efficient and selective formation of methanol from methane in a fuel cell-type reactor. *Journal of catalysis*, 279(2):233–240, 2011.

[189] A. Tomita, J. Nakajima, and T. Hibino. Direct oxidation of methane to methanol at low temperature and pressure in an electrochemical fuel cell. *Angewandte Chemie International Edition*, 47(8):1462–1464, 2008.

[190] S. H. Morejudo, R. Zanón, S. Escolástico, I. Yuste-Tirados, H. Malerød-Fjeld, P. K. Vestre, W. G. Coors, A. Martínez, T. Norby, J. M. Serra, et al. Direct conversion of methane to aromatics in a catalytic co-ionic membrane reactor. *Science*, 353(6299):563–566, 2016.

[191] M. Ma, C. Oh, J. Kim, J. H. Moon, and J. H. Park. Electrochemical CH_4 oxidation into acids and ketones on ZrO_2: $NiCo_2O_4$ quasi-solid solution nanowire catalyst. *Applied Catalysis B: Environmental*, 259:118095, 2019.

[192] M. Ma, B. J. Jin, P. Li, M. S. Jung, J. I. Kim, Y. Cho, S. Kim, J. H. Moon, and J. H. Park. Ultrahigh electrocatalytic conversion of methane at room temperature. *Advanced Science*, 4(12):1700379, 2017.

[193] R. S. Rocha, R. M. Reis, M. R. Lanza, and R. Bertazzoli. Electrosynthesis of methanol from methane: The role of V_2O_5 in the reaction selectivity for methanol of a $TiO_2/RuO_2/V_2O_5$ gas diffusion electrode. *Electrochimica acta*, 87:606–610, 2013.

[194] R. S. Kim and Y. Surendranath. Electrochemical reoxidation enables continuous methane-to-methanol catalysis with aqueous Pt salts. *American Chemical Society Central Science*, 5 (7):1179–1186, 2019.

[195] N. Spinner and W. E. Mustain. Electrochemical methane activation and conversion to oxygenates at room temperature. *Electrochemical Society Transactions*, 53(23):1, 2013.

[196] Z. Guo, W. Chen, Y. Song, X. Dong, G. Li, W. Wei, and Y. Sun. Efficient methane electrocatalytic conversion over a Ni-based hollow fiber electrode. *Chinese Journal of Catalysis*, 41(7):1067–1072, 2020.

[197] Y. Song, Y. Zhao, G. Nan, W. Chen, Z. Guo, S. Li, Z. Tang, W. Wei, and Y. Sun. Electrocatalytic oxidation of methane to ethanol via NiO/Ni interface. *Applied Catalysis B: Environmental*, 270:118888, 2020.

[198] C. Oh, J. Kim, Y. J. Hwang, M. Ma, and J. H. Park. Electrocatalytic methane oxidation on Co_3O_4–incorporated ZrO_2 nanotube powder. *Applied Catalysis B: Environmental*, 283: 119653, 2021.

[199] J. Deng, S.-C. Lin, J. Fuller III, J. A. Iñiguez, D. Xiang, D. Yang, G. Chan, H. M. Chen, A. N. Alexandrova, and C. Liu. Ambient methane functionalization initiated by electrochemical oxidation of a vanadium (V)-oxo dimer. *Nature communications*, 11(1):3686, 2020.

[200] T. J. Omasta, W. A. Rigdon, C. A. Lewis, R. J. Stanis, R. Liu, C. Q. Fan, and W. E. Mustain. Two pathways for near room temperature electrochemical conversion of methane to methanol. *Electrochemical Society Transactions*, 66(8):129, 2015.

[201] M. Dippon, S. M. Babiniec, H. Ding, S. Ricote, and N. P. Sullivan. Exploring electronic conduction through $BaCe_xZr_{0.9-x}Y_{0.1}O_{3-\delta}$ proton-conducting ceramics. *Solid State Ionics*, 286:117–121, 2016.

[202] N. Bausá, C. Solís, R. Strandbakke, and J. M. Serra. Development of composite steam electrodes for electrolyzers based on barium zirconate. *Solid State Ionics*, 306:62–68, 2017.

[203] M. Chen, M. Zhou, Z. Liu, and J. Liu. A comparative investigation on protonic ceramic fuel cell electrolytes $BaZr_{0.8}Y_{0.2O-\delta}$ and $BaZr_{0.1}Ce_{0.7}Y_{0.2}O_{3-\delta}$ with NiO as sintering aid. *Ceramics International*, 48(12):17208–17216, 2022.

[204] T. Norby and Y. Larring. Concentration and transport of protons in oxides. *Current Opinion in Solid State and Materials Science*, 2(5):593–599, 1997.

[205] N. Bonanos. Transport properties and conduction mechanism in high-temperature protonic conductors. *Solid State Ionics*, 53-56:967–974, 1992.

[206] N. S. Patki, A. Manerbino, J. D. Way, and S. Ricote. Galvanic hydrogen pumping performance of copper electrodes fabricated by electroless plating on a $BaZr_{0.9-x}Ce_xY_{0.1}O_{3-\delta}$ proton-conducting ceramic membrane. *Solid State Ionics*, 317:256–262, 2018.

[207] M. Wang, T. Ma, H. Wang, S. Yu, and L. Bi. Microwave sintering coupled with sintering aids for proton-conducting oxide membranes. *Ceramics International*, 49(11, Part B):19561–19568, 2023.

[208] J. Tong, D. Clark, L. Bernau, M. Sanders, and R. O'Hayre. Solid-state reactive sintering mechanism for large-grained yttrium-doped barium zirconate proton conducting ceramics. *Journal of Materials Chemistry*, 20(30):6333–6341, 2010.

[209] J. Peng, H. Li, and S. Lin. Study on properties of $BaZr_{0.7}Ce_{0.2}Y_{0.1}O_{3-\delta}$ ceramics prepared by high-pressure sintering. *Journal of the Ceramic Society of Japan*, 128(2):62–65, 2020.

[210] Y. Meng, J. Gao, H. Huang, M. Zou, J. Duffy, J. Tong, and K. S. Brinkman. A high-performance reversible protonic ceramic electrochemical cell based on a novel Sm-doped $BaCe_{0.7}Zr_{0.1}Y_{0.2}O_{3-\delta}$ electrolyte. *Journal of Power Sources*, 439:227093, 2019.

[211] C. Duan, J. Tong, M. Shang, S. Nikodemski, M. Sanders, S. Ricote, A. Almansoori, and R. O'Hayre. Readily processed protonic ceramic fuel cells with high performance at low temperatures. *Science*, 349(6254):1321–1326, 2015.

[212] A. Gondolini, A. Bartoletti, E. Mercadelli, P. Gramazio, A. Fasolini, F. Basile, and A. Sanson. Development and hydrogen permeation of freeze-cast ceramic membrane. *Journal of Membrane Science*, 684:121865, 2023.

[213] Q. Wang, T. Luo, Y. Tong, M. Dai, X.-Y. Miao, S. Ricote, Z. Zhan, and M. Chen. Large-area protonic ceramic cells for hydrogen purification. *Separation and Purification Technology*, 295:121301, 2022.

[214] S. Pirou, Q. Wang, P. Khajavi, X. Georgolamprou, S. Ricote, M. Chen, and R. Kiebach. Planar proton-conducting ceramic cells for hydrogen extraction: Mechanical properties, electrochemical performance and up-scaling. *International Journal of Hydrogen Energy*, 47(10):6745–6754, 2022.

[215] I. Yuste-Tirados, X. Liu, C. Kjølseth, and T. Norby. Impedance of a tubular electrochemical cell with BZCY electrolyte and Ni-BZCY cermet electrodes for proton ceramic membrane reactors. *International Journal of Hydrogen Energy*, 2023.